Electromagnetic induction studies with long-periodic geomagnetic variations in Europe - I. Theory and methods of data analysis

Ulrich Schmucker

Contents

Electromagnetic induction studies with long-periodic geomagnetic variations in Europe - I. Theory and methods of data analysis

Ulrich Schmucker
Geophysikalisches Institut Universität Göttingen, Postfach 2341, D-37013 Göttingen, Germany

SUMMARY

The theoretical foundations of the various methods of magneto-variational sounding (*MVS*) are developed from first principles. Because only time variations of the Earth's magnetic field are involved, these methods respond exclusively to the tangential-electric (*TE*) mode of the electromagnetic field on and above ground, presuming that the inducing source field is also in this mode. With increasing period MVS results become less and less sensitive to lateral resistivity contrasts at shallow depth, which is demonstrated. It sets these methods apart from magneto-telluric soundings (*MTS*) subject to persistent surface effects due to anomalous electric field variations in the tangential-magnetic (*TM*) mode. This work concentrates on the analysis of daily variations and associated activity-related variations, yielding response estimates for periods between three hours and two days. The relevant depth range of penetration extends from $250\,km$ to $750\,km$ and includes the transition from a resistive upper mantle ($\geq 100\,\Omega m$) to a conducting deeper mantle ($\leq 1\,\Omega m$). The ultimate purpose of this study is to obtain information about the degree of lateral uniformity in resistivity beneath Europe.

Among MVS methods the gradient method is the most versatile one, relating the vertical component of geomagnetic variations to the spatial derivatives of their horizontal components. The connecting transfer function is the C-response. Within certain limits, which are specified, the method can be applied without concern about the spatial structure of the inducing source field, which is tested with response estimates for variations from two different sources: Quasi-periodic daily variations and transient storm-time variations. All calculations are carried out in spherical coordinates, Alternative MVS methods based on global presentations of the horizontal components by one or more spherical harmonics are of restricted applicability. Tests show that the gradient method gives the best results.

A new generalised version of this method removes the constraint about one-dimensionality. It combines gradient sounding with geomagnetic depth sounding (*GDS*), provided the source field is of sufficient spatial complexity to rule out representation by a single spherical harmonic. The resulting multivariate relation involves up to five transfer functions, including a tensor C-response in close relation to the tensor impedance for the TE mode in the electric field. Input variables are three of the four spatial derivatives of the horizontal components and these components themselves. They are derived from polynomials fitted to the horizontal components in a network of observing sites. An eigen-value analysis ascertains that the performed fit of 2-dimensional second degree polynomials is a numerically stable process. A second eigen-value analysis concerns the inversion of the spectral matrix in multivariate regressions, indicating that regularisation is required, when all five transfer functions are to be found. Eigen-solutions identify the two GDS transfer functions together with the Berdichevsky-average of the tensor C-response as the best resolvable combination. Two kinds of errors are derived for (robust) estimates of transfer functions, distribution-dependent errors and jack-knife errors. For univariate regressions both errors are of comparable size, but for trivariate regressions the former turn out to be twice as large. The data base for exemplary soundings are two years of hourly mean values (1964-65) at 35 European observatories.

1 INTRODUCTION

Observations of geomagnetic variations provide information about electrical properties of matter within the Earth. The experimental data for the following studies are tabulated hourly mean values, prepared by a network of more than 30 observatories in Europe. Time-series of up to two years length have been analysed. At some sites simultaneous records of geo-electric fields would have been available, but their concurrent evaluation for magneto-telluric soundings (*MTS*) will be the subject of a later publication. Data processing for inferences about internal conductivities can be performed either in the time-domain or in the frequency-domain, yielding for further interpretations electromagnetic responses as functions of time or frequency. Because of the oscillatory nature of the variations to be studied, our choice is the frequency-domain, leading to magneto-variational sounding (*MVS*) results in the form of complex transfer functions estimated from univariate and multivariate linear regressions.

Time-series with a sampling rate of one value per hour cannot provide reliable estimates of transfer functions for periods which are too close to the Nyquist period, here two hours. Towards longer periods the chosen length of analysed time-series sections sets an upper limit of, say, one fifth of this length. With the choice of ten-day sections the period range of response estimates extends from three or four hours to 48 hours. Within this range two major types of geomagnetic variations occur: Regular quasi-periodic daily variations (S_r) and an assortment of irregular transient variations (S_{cont}) in connection with magnetic storm-time activity, forming a spectral background continuum. At its longest periods we can expect contributions from the recovery phase of magnetic storms (D_{st}), and within daily variations a small part will be due to lunar geomagnetic tides (L). The analysis of longer time-sections toward D_{st} responses for periods of many days is deferred until a later time.

The depth to which both types of variations penetrate downward into the Earth extends from $250\,km$ to $750\,km$ according to previous studies with daily variations during quiet times, using the Z:Y and the potential methods (Olsen, 1998, Fig. 5; Schmucker, 1999b, Table 8), but these results may be biased toward conditions beneath continents. The aim of the following work is to obtain detailed knowledge about electric conductivities in the quoted depth range beneath Europe. Emphasis will be on horizontal spatial gradient sounding (*HSG*) and its combination with geomagnetic depth sounding (*GDS*), the latter extended for the first time to periods beyond a few hours.

Henceforth we shall refer to the HSG method simply as *gradient method* to investigate layered 1D structures. It relates the vertical component of geomagnetic variations to the spatial derivatives of their horizontal components, while in GDS it is related to the horizontal components themselves to study deviations from 1D structures. The transfer function in gradient sounding is the scalar C-response, which in its real part is a direct measure for the downward penetration depth of the electromagnetic field into the Earth, reflecting the skin-effect at the respective site. We shall consider also an extension to tensor C-responses, in analogy to the tensor impedance in MTS to overcome the restriction to 1-dimensionality. We shall see that GDS transfer functions represent spatial derivatives of C-responses, where lateral changes of resistivity cause a variable penetration depth and thereby *induction anomalies* of the internal part of geomagnetic variations. This connection provides a mutual test of gradient sounding and GDS for compatibility.

The divergence-free magnetic vector $\underline{B}$ can be split into a tangential-electric (*TE*) or induction mode, associated with likewise divergence-free currents tangential to plane or spherical surfaces, and a tangential-magnetic (*TM*) or galvanic mode with magnetic field lines confined to them. Throughout this presentation we assume that the inducing source field meets the following three

conditions: that it is a field exclusively in the TE mode, laterally quasi-uniform in the sense that its lateral dimension, for example its half-width, is much larger than the penetration depth at the respective period, and thirdly that its time-space structure is complicated enough to rule out representations by a single spherical or plane harmonic.

Violation of the first condition could lead to unwanted vertical magnetic components in connections with TM source constituents, where deviations from a stratified Earth occur and thereby anomalous fields in the TE mode. This is a very unlikely possibility, however, in the case of long-periodic variations. There may exist TM modes in their ionospheric and magnetospheric source regions, but their low frequency and the nearly non-conducting air space prevents them from reaching down to the surface of the Earth.

Violation of the second condition does not rule out MVS, but the resulting transfer functions would depend then on the source field structure, for example on the degrees of spherical harmonics involved, which is not the case otherwise. Long-periodic variations meet in mid-latitudes also the second condition. Here source dimensions are in the order of thousand kilometres and thereby well in excess of the penetration depth for the longest periods. Still the second condition of quasi-uniformity remains critical and will receive further attention.

Violation of the third condition renders it impossible to distinguish between the part of the vertical component connected as *normal part* to spatial derivatives of the horizontal components and as *anomalous part* to these components themselves. For example, the potential U of the D_{st} recovery phase of magnetic storms is well accounted for by a single spherical harmonic $P_1(\cos\theta) = \cos\theta$, yielding $B_\theta = -dU/d\theta \propto \sin\theta$ for co-latitude θ. With $dB_\theta/d\theta = B_\theta \cdot \mathrm{ctg}\theta$ a linear relationship evolves between B_θ and its derivative with respect to co-latitude, which prohibits a combined application of the gradient method and GDS. It may be just stated that in this context the coherence between horizontal field components and their derivatives has been found to be small enough to permit combined gradient sounding and GDS, even though for S_{cont} more so than for S_r.

With regard to surface effects, which are caused by lateral resistivity changes at shallow depth, it may be sufficient to point out that they diminish with increasing period T at the same rate as the electric surface field in the TE mode, the driving force for deflected subsurface currents in that mode. In relation to the horizontal magnetic field its strength is given by the TE mode impedance $2\pi C/T$ which decreases as $1/\sqrt{T}$ for uniform conductors, when C increases according to $\sqrt{T}$. For the real Earth the decline becomes more rapid, when at sufficiently long periods highly conducting matter is reached in the deeper mantle, slowing down the further increase of penetration depth. This quasi-static approach is valid, however, only for small-scale features in relation to $|C|$. Otherwise self-induction and inductive coupling to the underlying structure has to be taken into account. Neither does this reasoning apply to deflected subsurface currents connected to anomalous electric fields in the TM mode, the cause of persistent modifications of MTS results almost anywhere towards longer periods.

A final note concerns $curl\,\underline{B}$ in the air space above ground and below the ionosphere. In this nearly non-conducting space and considering the extremely low frequencies to be studied neither conduction nor displacement currents should render $curl\,\underline{B}$ significantly different from zero. Setting then $curl\,\underline{B}$ exactly to zero in an approximate manner, this has two consequences: Firstly, toroidal magnetic fields with $curl\,\underline{B} \neq 0$ are ignored as they would exist in conjunction with anomalous electric fields in the TM mode. Secondly, poloidal magnetic fields for electric fields in the TE mode become potential fields. For further insight we turn to the Helmholtz equation which governs the propagation of electromagnetic fields in matter of resistivity ρ and velocity of light c. Their general solution for spherical conductors, composed of a sequence of uniform shells, involves modified

spherical Bessel functions of the first and second kind of orders $\pm n$ to express the dependence on radius r, with spherical harmonics of degree n to describe angular dependencies. Their argument is $u = ikr$ with $k = [i\omega\mu_0/\rho - (\omega/c)^2]^{1/2}$ as propagation constant. Inserting $\mu_0 = 4\pi \cdot 10^{-7} Vs/Am$ as free-space permeability, $\rho = 10^{14}\,\Omega m$ for air near to the ground, and $c = 10^5\,km/s$ yields $|k| = 3.8 \cdot 10^{-9}\,km^{-1}$ for $\omega = 10^{-3}\,s^{-1}$ or $T = 1.7\,hrs$.

$|u| \approx 10^{-5}$, and with the asymptotic values u^n and $1/u^{n+1}$, respectively, for modified spherical Bessel functions for $u \to 0$, solutions for the Helmholtz equation merge asymptotically into the solutions of the Laplace equation for potential fields (cf. eq. 24 and also Eckhardt et al., 1963, p. 6281).

2 BASIC EQUATIONS

2.1 Gradient sounding on a flat Earth

Field components are subscripted according to right-handed Cartesian co-ordinates with z down and the plane $z = 0$ representing the Earth's surface; orientations of horizontal axes are x toward geographic north and y toward geographic east. Notations B_x, B_y, B_z for the components of the magnetic vector $\underline{B}$ and corresponding notations for the electric vector $\underline{E}$ refer to complex Fourier transforms at angular frequency ω. Time factor is $exp(i\omega t)$ with t as time. The upper half-space is assumed to be non-conducting up to a certain height $z = -H\,(H > 0)$, where the source region begins, while the lower half-space is a stratified conductor with isotropic conductivity $\sigma = \sigma(z)$ and $\sigma(z) > 0$ for $z \to \infty$ The time-varying inducing source field shall be in the tangential TE mode and thus with $E_z = 0$ for $z > -H$.

The derivation of the basic equations proceeds conveniently from Weidelt's definition of the C-response (Weidelt, 1972, eq. 4):

$$C(\omega) =: \frac{E_x(\omega,0)}{-\partial E_x/\partial z\,|_{z=0}} = \frac{E_y(\omega,0)}{-\partial E_y/\partial z\,|_{\,z=0}} \tag{1}$$

For a given 1D model it can be found readily by solving the 1-dimensional diffusion equation $d^2E/dz^2 = i\omega\mu_0\sigma(z)E(z)$ for uniform electric fields $E = E_x$ or E_y in horizontal planes, even though at the same time a small degree of non-uniformity shall exist providing finite derivatives $\partial E/\partial x$ and $\partial E/\partial y$. The apparent contradiction will be resolved with the forthcoming concept of "quasi-uniformity".

Faraday's law $curl\,E = -i\omega B$ connects below the source region the spatial derivatives of the two horizontal components of electric field to the three components of the magnetic field:

$$\frac{\partial E_x}{\partial z} = -i\omega B_y,\ \frac{\partial E_y}{\partial z} = +i\omega B_x,\ \frac{\partial E_x}{\partial y} - \frac{\partial E_y}{\partial x} = i\omega B_z\,. \tag{2}$$

Inserting eq. (1) into the first two equations for $z = 0$ yields the impedance relations

$$E_x = +i\omega C(\omega) \cdot B_y\, and\, E_y = -i\omega C(\omega) \cdot B_x \tag{3}$$

which connect in

$$Z(\omega) = i\omega C(\omega) \tag{4}$$

the scalar impedance $Z(\omega)$ of a layered half-space to its C-response. Differentiating in eqs (3) E_x with respect to y, E_y with respect to x and evaluating with the resulting derivatives the third equation of Faraday' s law gives

$$B_z = C(\omega) \cdot \left(\frac{\partial B_x}{\partial x} - \frac{\partial B_y}{\partial y} \right) \tag{5}$$

as basic equation of gradient sounding ((Schmucker, 1970a, eq. 5.54) and Kuckes, 1973, eq. 10). The combination of spatial derivatives in parenthesis is called the horizontal spatial gradient (HSG) of the surface field.

An alternative derivation utilizes the non-divergence of magnetic fields. From Faraday' s law it can be inferred that B_z has the same dependence on depth z as E_x and E_y. Hence,

$$C(\omega) =: \frac{\partial B_z(\omega,0)}{-\partial B_z/\partial z \mid_{z=0}} \tag{6}$$

is an alternative definition of the C-response which when inserted into

$$div\underline{B} = \frac{\partial B_x}{\partial x} + \frac{\partial B_y}{\partial y} + \frac{\partial B_z}{\partial z} = 0$$

leads back to eq. (5).

We turn now to the case of unrestricted spatial source geometry and begin with a Fourier transformation from the space into the wave-number domain. Henceforth $\hat{F}$ denotes the Fourier transform of field component F in horizontal planes, i.e.

$$\hat{F}(\omega,\underline{k},z) = \int\int F(\omega,\underline{r},z) exp[-i\underline{kr}] d\underline{r},\; F(\omega,\underline{r},z) = \frac{1}{4\pi^2} \int\int \hat{F}(\omega,\underline{k},z) exp[i\underline{kr}] d\underline{k}, \tag{7}$$

with $\underline{r} = (x,y)$ as horizontal location vector, $\underline{k} = (k_x, k_y)$ as horizontal wave-number vector and with $k = +\sqrt{k_x^2 + k_y^2}$ as scalar wave-number. Then Faraday's law for the vertical component of $curl\underline{E}$ reads in terms of these transforms $ik_y\hat{E}_x - ik_x\hat{E}_y = i\omega\hat{B}_z$. Insertion of the correspondingly transformed impedance relations $\hat{E}_x = i\omega\hat{C}\hat{B}_y$ and $\hat{E}_y = -i\omega\hat{C}\hat{B}_x$ with

$$\hat{C}(\omega,k) =: \frac{\hat{E}_x(\omega,\underline{k},0)}{-\partial\hat{E}_x/\partial z \mid_{z=0}} = \frac{\hat{E}_y(\omega,\underline{k},0)}{-\partial\hat{E}_y/\partial z \mid_{z=0}} \tag{8}$$

in analogy to eq. (1) leads to

$$\hat{B}_z = \hat{C}(\omega,k) \cdot \left(ik_x\hat{B}_x + ik_y\hat{B}_y \right) \tag{9}$$

the $(\omega, \underline{k})$-domain C-response follows now from $d^2\hat{E}/dz^2 = [i\omega\mu_0\sigma(z) + k^2] \cdot \hat{E}(\omega,k,z)$. Its sole dependence on the scalar wave-number is an obvious consequence of the necessity that the response above stratified conductors cannot depend on the orientation of $\underline{k}$.

As shown in Appendix A, the partial derivative $\partial\hat{C}/\partial k$ approaches zero for $k \to 0$, which implies that $\hat{C}(\omega,k)$ merges asymptotically into the response $\hat{C}(\omega,0)$ for a uniform field in horizontal planes. Physically it means, as seen in the forthcoming eq. (11) for $\hat{C}k \to 0$, that external and internal parts of the magnetic potential become equal which in turn implies that the horizontal components of the magnetic source field are doubled by induction and its vertical component annihilated. Hence, for sufficiently small *but still finite wave-numbers* we may substitute $\hat{C}(\omega,k)$ by $\hat{C}(\omega,0)$, henceforth denoted as $C(\omega)$ for shortness. In other words, we assume that a small

degree of spatial non-uniformity causes the compensation of the vertical source field component to be incomplete, which leaves an observable B_z for gradient sounding. But the non-uniformity is at the same time thought to be small enough to keep $\hat{C}(\omega,k)$ very close to the asymptotic zero wave-number response $C(\omega)$.

Provided that B_x and B_y are sufficiently smooth functions of location in horizontal planes, their Fourier transforms may be set to zero beyond a certain maximum wave-number k_{max}. If then, as seen from eq. (11), the inequality $k\cdot \mid \hat{C}(\omega,k) \mid \ll 1$ holds up to $k = k_{max}$, this field will be considered as *quasi-uniform* for frequency ω in the sense that the above substitution is justified. Since $ik_x\hat{B}_x$ and $ik_y\hat{B}_y$ are the Fourier transforms of $\partial B_x/\partial x$ and $\partial B_y/\partial y$, respectively, an inverse Fourier transformation of eq. (9) back into the space domain, with $C(\omega)$ replacing $\hat{C}(\omega,k)$ as a constant, re-establishes eq. (5). Appendix A contains for completeness the unrestricted inverse transformation and shows that the right-hand-side of eq. (5) has to be understood as a series expression truncated after the first term.

In conclusion we consider the original definition of the C-response in terms of external and internal parts of the potential (Schmucker, 1970a, Section 5.3). Its Fourier transform as function of z is conveniently written as

$$\hat{U}(\omega,\underline{k},z) = \frac{1}{k}\left(E(\omega,\underline{k})\cdot e^{-kz} + I(\omega,\underline{k})\cdot e^{+kz}\right) \tag{10}$$

for $0 \geq z > -H$, which satisfies Laplace's equation $k^2\hat{U} + \partial^2\hat{U}/\partial^2 z = 0$ in the (ω,k)-domain as well as conditions at infinity, namely that the external part with coefficient $E(\omega,\underline{k})$ arising from the overhead source disappears at infinite depth and that the internal part with coefficient $I(\omega,\underline{k})$ from induced currents tends to zero with increasing height. Note that in this context the symbol E refers to the external part of the magnetic potential rather than to electric fields. Inserting $\hat{B}_z = -\partial\hat{U}/\partial z = E - I$ and $\partial\hat{B}/\partial z = -k\cdot(E+I)$ for $z = 0$ into the (ω,k)-domain version of eq. (6) yields

$$\hat{C}(\omega,k) = \frac{1}{k}\cdot\frac{E(\omega,\underline{k}) - I(\omega,\underline{k})}{E(\omega,\underline{k}) + I(\omega,\underline{k})}\,. \tag{11}$$

We conclude that internal and external parts become asymptotically equal, when the *product* $k\hat{C}$ approaches zero, allowing $\hat{C}$ as one of the two factors to remain finite for $k \to 0$. The limiting case illuminates once more the concept of induction by quasi-uniform source fields.

2.2 Gradient sounding on a spherical Earth

We use geocentric spherical coordinates (r,θ,λ), with r = R as Earth's surface, θ and λ as geographic co-latitude and longitude, respectively, and we assume again induction by a quasi-uniform TE source field, with $E_r = 0$ below the source region. Inside the Earth conductivity is assumed to be a sole function of radius r with poorly conducting air between $r = R$ and $r = R+H$, where the external source region begins. The C-response for a spherical Earth will be defined in a way that its relation to the surface impedance is retained in the form of eq. (4). Faraday's law, now

$$\frac{1}{r}\frac{\partial}{\partial r}(rE_\lambda) = +i\omega B_\theta,\ \frac{1}{r}\frac{\partial}{\partial r}(rE_\theta) = -i\omega B_\lambda,\ \frac{1}{r\sin\theta}\left\{\frac{\partial}{\partial\theta}(\sin\theta\cdot E_\lambda) - \frac{\partial E_\theta}{\partial\lambda}\right\} = -i\omega B_r\,, \tag{12}$$

suggests that

$$C_0(\omega) =: \frac{RE_\theta(\omega,R)}{-\partial(rE_\theta)/\partial r\mid_{r=R}} = \frac{RE_\lambda(\omega,R)}{-\partial(RE_\lambda)/\partial r\mid_{r=R}} \tag{13}$$

is an appropriate definition because it leads by the same reasoning as for a flat Earth to the impedance relations

$$E_\theta = -i\omega C_0(\omega)\cdot B_\lambda, E_\lambda = +i\omega C_0(\omega)\cdot B_\theta\,. \tag{14}$$

The insertion of the resulting derivatives $\partial(\sin\theta\cdot E_\lambda)/\partial\lambda$ and $\partial E_\theta/\partial\lambda$ for $r=R$ into the third equation of Faraday's law establishes in

$$B_r = \frac{C_0(\omega)}{R\sin\theta}\cdot\left\{\frac{\partial}{\partial\theta}(\sin\theta\, B_\theta)+\frac{\partial B_\lambda}{\partial\lambda}\right\} \tag{15}$$

the basic relation for gradient sounding in spherical co-ordinates.

The appropriate definition of the C-response for spherical conductors in terms of the radial component of the magnetic field is

$$C_0(\omega) =: \frac{R^2 B_r(\omega,R)}{-\partial(r^2B_r)/\partial r\,|_{r=R}} \tag{16}$$

Together with

$$div\underline{B} = \frac{1}{r\sin\theta}\left\{\frac{\partial}{\partial\theta}(\sin\theta\, B_\theta)+\frac{\partial B_\lambda}{\partial\lambda}\right\}+\frac{1}{r^2}\frac{\partial}{\partial r}(r^2B_r)=0\,,$$

it provides for $r=R$ an alternative derivation of eq. (15). This path has been taken by Berdichevsky et al. (1969). Here equation (8) corresponds to our eq. (16) and their equation (9) is our eq. (15).

The concept of quasi-uniformity in spherical geometry has to be re-formulated now in terms of spherical harmonics. Their notation is as follows: The series representation for a field component F on a sphere of radius r will be $F(r,\vartheta,\lambda)=\sum\limits_{n,m}\hat{F}_n^m(r)\cdot Y_n^m(\theta,\lambda)$, in which $\hat{F}_n^m$ is the coefficient for the (elementary) surface harmonic

$$Y_n^m(\theta,\lambda) = P_n^m(\cos\theta)\cdot exp(im\lambda) \tag{17}$$

of degree n and order m. The symbol $\sum\limits_{n,m}$ implies a summation over orders from $m=-n$ to $m=+n$, followed by a summation over degrees from $n=1$ to $n=\infty$, $P_n^m(\cos\theta)$ denotes an associated spherical function of degree n to $exp(im\lambda)$, and Y_n^m is solution of the partial differential equation

$$\frac{\partial(\sin\theta\,\partial Y_n^m/\partial\theta)}{\sin\theta\,\partial\theta} = \left[m^2/\sin^2\theta - n(n+1)\right]\cdot Y_n^m\,. \tag{18}$$

Next we connect the coefficients of the tangential components to those of the potential U. For convenience the latter are multiplied with the radius of the Earth, yielding $U = R\sum\limits_{n,m}\hat{U}_n^m\cdot Y_n^m$.

From $\underline{B} = -gradU$ or $B_\theta = -1/R\cdot\partial U/\partial\theta$, $B_\lambda = -1/(R\sin\theta)\cdot\partial U/\partial\lambda$ the coefficients are

$$\hat{B}_{\theta,n}^m = -\hat{U}_n^m\cdot Q_n^m/P_n^m \tag{19}$$

with $Q_n^m = dP_n^m/d\theta$ and

$$\hat{B}_{\lambda,n}^m = -\hat{U}_n^m\cdot im/\sin\theta\,. \tag{20}$$

Since the corresponding coefficients for the electric field are sole functions of r, the first two eqs (12) of Faraday's law are readily rewritten in terms of them. They lead together with the spherical C-response definition

$$\hat{C}_n(\omega) =: \frac{R\hat{E}_{\vartheta,n}^m(R,\omega)}{\partial(r\hat{E}_{\vartheta,n}^m)/\partial r\,|_{r=R}} = \frac{R\hat{E}_{\lambda,n}^m(R,\omega)}{\partial(R\hat{E}_{\lambda,n}^m)/\partial r\,|_{\,r=R}} \tag{21}$$

to impedance relations $\hat{E}^m_{\theta,n} = -i\omega\hat{C}_n \cdot \hat{B}^m_{\lambda,n}$ and $\hat{E}^m_{\lambda,n} = i\omega\hat{C}_n \cdot \hat{B}^m_{\theta,n}$ in analogy to eqs (14). Combined with Faraday's law

$$\frac{1}{r\sin\theta}\left\{\frac{d(\sin\theta \cdot P^m_n)}{P^m_n d\theta}\hat{E}^m_{\lambda,n} + im\hat{E}^m_{\vartheta,n}\right\} = -i\omega\hat{B}^m_{r,n} \tag{22}$$

for $r = R$, we obtain

$$\hat{B}^m_{r,n} = -\hat{C}_n/R\sin\theta \cdot \left(\frac{d(\sin\theta \cdot P^m_n)}{P^m_n d\theta}\hat{B}^m_{\vartheta,n} + im\hat{B}^m_{\lambda,n}\right) \tag{23}$$

as basic equation to derive C-responses in spherical coordinates for any surface field expanded into spherical harmonics. The exclusive dependence of $\hat{C}_n(\omega)$ on degree n corresponds to the sole dependence of the flat-Earth response $\hat{C}_n(\omega,k)$ on the scalar wave-number. Any dependence on order m would imply a dependence on the chosen position of the pole $\theta = 0$, which contradicts the invariance of the response against the orientation of coordinates, when the resistivity is a sole function of r.

As shown below $\hat{C}_n(\omega)$ merges asymptotically into the above introduced degree-independent response $C_0(\omega)$ for $(n+1)\hat{C}_n/R \to 0$. If then $(n+1) \mid \hat{C}_n(\omega) \mid /R$ is small against unity up to a maximum degree $n = n_{max}$, which provides an adequate representation of B_θ and B_λ, we can replace $\hat{C}_n(\omega)$ in eq. (23) by $C_0(\omega)$ and return to eq. (15) by summation, i.e. with $B_r = \sum_{n,m} Y^m_n \hat{B}^m_{r,n}$ and with $\partial(\sin\vartheta B_\theta)/\partial\vartheta = \sum_{n,m} \partial(\sin\vartheta Y^m_n)/\partial\vartheta \cdot \hat{B}^m_{\vartheta,n}$, $\partial B_\lambda/\partial\lambda = \sum_{n,m} imY^m_n/\hat{B}^m_{\lambda,n}$ as series for the derivatives.

It remains the task to express the C-response $\hat{C}_n(\omega)$ in terms of external part E^m_n and internal part I^m_n of the potential coefficient $\hat{U}^m_n$, now to be considered as function of r. Laplace's equation in spherical co-ordinates as well as the relevant conditions at $r = 0$ and $r \to \infty$ are satisfied by

$$\hat{U}^m_n(r) = R \cdot \left\{E^m_n(r/R)^n + I^m_n(r/R)^{n+1}\right\} \text{ for} R \le r < R + H\,. \tag{24}$$

Inserting $\hat{B}^m_{r,n} = -nE^m_n + (n+1)I^m_n$ and $\partial(r^2\hat{B}^m_{r,n})/\partial r = -n(n+1)\cdot(E^m_n + I^m_n)\cdot R$ for $r = R$ into eq. (16), rewritten in terms of the coefficients $\hat{B}^m_{r,n}$ and with $\hat{C}_n(\omega)$ taking the place of $C_0(\omega)$, leads to the desired relation

$$\hat{C}_n(\omega) = \frac{R}{n+1} \cdot \frac{E^m_n - (n+1)/n \cdot I^m_n}{E^m_n + I^m_n} \tag{25}$$

(Schmucker, 1970a, Section 5.2). Hence, in spherical geometry the concept of quasi-uniformity implies that the internal part approaches its upper limiting value $n/(n+1)\cdot E^m_n$, when the product $(n+1)\hat{C}_n/R$ tends to zero, i.e. when for a fixed degree n the radius R becomes infinitely large, while $\hat{C}_n(\omega)$ assumes its finite asymptotic value $C_0(\omega)$ which is identical with the zero wave-number response $C(\omega)$ for a flat Earth.

2.3 Gradient sounding in combination with geomagnetic depth sounding

We return temporarily to Cartesian co-ordinates and consider the induction in 3D structures with isotropic or anisotropic resistivities. As before we assume induction by a quasi-uniform TE source field, and now also the third condition from Section 1 becomes crucial, namely that no perfect or nearly perfect linear relations may exist between the horizontal magnetic components and their spatial derivatives. We postpone how to extend the definition of a scalar C-response in Section 2.1

to the now required tensor C-response and proceed instead directly from the conventional bivariate MTS impedance relations with two modifications:

Firstly we recall that induction by TE source fields generates anomalous TM modes, where deviations occur from a layered structure. But in air only the electric field contains both modes, while the observable magnetic field on and above ground remains in the TE mode (cf. Section 1). This allows us to split the electric components and the respective elements of the impedance tensor according to modes. Secondly E_x and E_y will not be related to B_x and B_y at the same location, as it is usually done in MTS, but to their normal parts B_{nx} and B_{ny}, which we would have observed in the absence of lateral non-uniformities, and which we assume to be smooth functions of location. While this has been presumed for their external parts, its extension to internal parts needs further attention.

Induction by quasi-uniform source fields implies that the (ω,k)-domain ratio of internal to external parts is close to unity, as already stated in conjunction with eq. (11). Therefore external and internal parts of the horizontal components are of comparable size for all relevant wave-numbers and the same applies to them after their transformation back into the space domain. Hence, the normal horizontal field as the sum of both parts will have about the same spatial quasi-uniformity as the source field. Using for example polynomials fitted by least squares to the observed horizontal components within a network of sites, the choice of low-degree polynomials achieves the desired spatial smoothness.

With the just outlined modifications the MTS relations to be evaluated are

$$\begin{aligned} E_x &= E_x^{TE} + E_x^{TM} = \left(Z_{xx}^{TE} + Z_{xx}^{TM}\right) \cdot B_{nx} + \left(Z_{xy}^{TE} + Z_{xy}^{TM}\right) \cdot B_{ny}\,, \\ E_y &= E_y^{TE} + E_y^{TM} = \left(Z_{yx}^{TE} + Z_{yx}^{TM}\right) \cdot B_{nx} + \left(Z_{yy}^{TE} + Z_{yy}^{TM}\right) \cdot B_{ny}\,. \end{aligned} \tag{26}$$

From Faraday's law $curl_z \underline{E} = -i\omega B_z$, applied separately to the two modes, follows

$$\frac{\partial E_x^{TE}}{\partial y} - \frac{\partial E_y^{TE}}{\partial x} = i\omega B_z\,,\ \frac{\partial E_x^{TM}}{\partial y} - \frac{\partial E_y^{TM}}{\partial x} = 0, \tag{27}$$

noting that TM modes have no vertical magnetic component by definition. Differentiating E_x in eqs (26) term by term towards y and correspondingly E_y towards x, while observing that the impedance tensor elements as well as B_{nx} and B_{ny} are now functions of locations, we obtain by insertion of the resulting derivatives into eq. (27)

$$\frac{\partial E_x}{\partial y} - \frac{\partial E_y}{\partial x} = \frac{\partial E_x^{TE}}{\partial y} - \frac{\partial E_y^{TE}}{\partial x} = Z_{xx}^{TE} \cdot \frac{\partial B_{nx}}{\partial y} + \frac{\partial Z_{xx}^{TE}}{\partial y} B_{nx} + \ldots = i\omega B_z. \tag{28}$$

In order to simplify notations, the elements of the TE mode impedance tensor are replaced by those of a herewith introduced C-response tensor $\underline{\underline{C}} = (C_{kl})$ according to

$$Z_{kl}^{TE} = i\omega C_{kl} \quad (k,l = 1,2) \tag{29}$$

with subscripts k and l for x and y. This converts eq. (28) into

$$B_z = C_{xx} \cdot \frac{\partial B_{nx}}{\partial y} + \frac{\partial C_{xx}}{\partial y} B_{nx} + \ldots$$

with altogether eight terms on the right-hand-side. The potential condition

$$\frac{\partial B_x}{\partial y} - \frac{\partial B_y}{\partial x} = 0 \tag{30}$$

for an irrotational magnetic field in air reduces their number to seven, and respectively two terms with the same horizontal components B_{nx} or B_{ny} can be combined into one. This leaves five terms on the right-hand-side, three terms involving spatial derivatives for the tensor C-response and two terms for GDS. The resulting multivariate expression with five transfer functions is

$$B_z = C_{xy} \cdot \frac{\partial B_{ny}}{\partial y} - C_{yx} \cdot \frac{\partial B_{nx}}{\partial x} + (C_{xx} - C_{yy}) \cdot \frac{\partial B_{nx}}{\partial y} + z_H \cdot B_{nx} + z_D \cdot B_{ny}, \tag{31}$$

where

$$z_H = \frac{\partial C_{xx}}{\partial y} - \frac{\partial C_{yx}}{\partial x},\ z_D = \frac{\partial C_{xy}}{\partial y} - \frac{\partial C_{yy}}{\partial x}. \tag{32}$$

For reasons which will become clear in Section 5.1, the first two terms are re-arranged according to their sums and differences. This gives

$$B_z = C_1 \cdot \left(\frac{\partial B_{nx}}{\partial x} + \frac{\partial B_{ny}}{\partial y} \right) + C_2 \cdot \left(\frac{\partial B_{ny}}{\partial y} - \frac{\partial B_{nx}}{\partial x} \right) + C_3 \cdot \frac{\partial B_{nx}}{\partial y} + z_H \cdot B_{nx} + z_D \cdot B_{ny} \tag{33}$$

with

$$C_1 = (C_{xx} - C_{yx})/2\ , C_2 = (C_{xy} + C_{yx})/2\ \ C_3 = (C_{xx} - C_{yy})\ , \tag{34}$$

from now on to be used as basic equation for gradient sounding in combination with GDS.

Transfer function C_1 represents the rotation-invariant *Berdichevsky average* of the off-diagonal elements, transfer functions C_2 and C_3 account for anisotropy and 3D effects. The rotation-invariant sum $(C_{xx} + C_{yy})$ of diagonal elements cannot be determined, a consequence of the potential condition, which reduces the number of independent derivatives from four to three. It is not possible therefore to determine the skew of $\underline{\underline{C}}$, but the derivable transfer functions are sufficient to allow transformations to rotated co-ordinates. The fourth and fifth transfer functions z_H and z_D are GDS transfer functions in their original definition (Schmucker, 1970a, Section 3.8) and eqs (32) clarify their implication for the spatial variability of the tensor C-response above 3D structures. Subscripts are relics of former times, when B_x was called "H", for "horizontal component", and B_y was called "D", for "declination".

With the aid of eq. (12) the spherical version of eq. (33) follows as

$$\begin{aligned} B_r = & \frac{1}{R \sin\theta} \cdot \left\{ C_1 \cdot \left(\frac{\partial}{\partial \theta}(\sin\theta \cdot B_{n\theta}) + \frac{\partial B_{n\lambda}}{\partial \lambda} \right) + C_2 \cdot \left(\frac{\partial B_{n\lambda}}{\partial \lambda} - \frac{\partial}{\partial \theta}(\sin\theta \cdot B_{n\theta}) \right) - C_3 \cdot \frac{\partial B_{n\theta}}{\partial \lambda} \right\} \\ & + z_H \cdot B_{n\theta} - z_D \cdot B_{n\lambda} \end{aligned} \tag{35}$$

with C_1, C_2 and C_3 as before and

$$z_H = \left(\frac{\partial C_{xx}}{\sin\theta \partial \lambda} + \frac{\partial C_{yx}}{\partial \theta} \right)/R\ \ z_D = \left(\frac{\partial C_{xy}}{\sin\theta \partial \lambda} + \frac{\partial C_{yy}}{\partial \theta} \right)/R. \tag{36}$$

In the derivation the potential condition in spherical coordinates

$$\frac{\partial B_\theta}{\partial \lambda} - \frac{\partial}{\partial \theta}(\sin\theta \cdot B_\lambda) = 0 \tag{37}$$

has been used.

Kuckes et al. (1985) have proposed a similar generalization of gradient sounding in combination with GDS, and their equations (15) and (16) correspond to our eq. (35). Their derivations are based

on expanding the potential of the normal field, which they call the "excitation part" of the surface field, into spherical harmonics with origin $r = 0$ at ground level and here at the point, where the sounding is to be performed. The dependence on distance is r^n with $n = 1, 2, \ldots$. The expansion coefficients are determined by fitting polynomials to B_x and B_y within a network of observing sites. Because Kuckes et al. assume the potential to have equal internal and external parts, the excitation field has no vertical component. The remaining anomalous B_{az}, called the "scattered part" of the surface field, represent as "scattered amplitudes" the coefficients in the series of the spherical harmonics. By limiting polynomials to second degree, Kuckes et al. obtain their final relations. Some of these scattered amplitudes can be identified as C-response and GDS transfer functions, but otherwise their implications are complicated by the use of polar coordinates for the surroundings of the sounding site, not counting that connections to MTS impedances are not considered.

The case of 2D structures deserves special attention. If C_3 and z_H vanish for certain rotated coordinates (x', y'), x' and not y' is the strike direction because no anomalous magnetic field exists for B-polarisation. Furthermore, the anomalous electric field for this polarisation is in the TM mode, which implies that the impedance element $-Z^{TE}_{y'x'}$ is identical with the scalar impedance for the normal structure. It is preferable in this special case to proceed from eq. (31) rather than from eq. (33). Its 2D version is

$$B_z = C_{x'y'} \cdot \frac{\partial B_{ny'}}{\partial y'} - C_{y'x'} \cdot \frac{\partial B_{nx'}}{\partial x'} + z_D \cdot B_{ny'}. \tag{38}$$

with $C_{x'y'}$ as C-response for E-polarisation, with $-C_{y'x'} = C(\omega)$ as scalar C-response for the surrounding normal structure and with $z_D = \partial C_{x'y'}/\partial y'$. The formulas to transfer spatial derivatives to rotated coordinates, with α as strike angle against x counted clockwise, are

$$\begin{aligned} \frac{\partial B_{nx'}}{\partial x'} &= \frac{\partial B_{nx}}{\partial x}\cos^2\alpha + 2\frac{\partial B_{nx}}{\partial y}\cos\alpha\sin\alpha + \frac{\partial B_{ny}}{\partial y}\sin^2\alpha\,, \\ \frac{\partial B_{ny'}}{\partial y'} &= \frac{\partial B_{nx}}{\partial x}\sin^2\alpha - 2\frac{\partial B_{nx}}{\partial y}\cos\alpha\sin\alpha + \frac{\partial B_{ny}}{\partial y}\cos^2\alpha\,. \end{aligned} \tag{39}$$

Other possibilities for a reduction to three transfer functions are the assumption of a lower halfspace which is laterally uniform but anisotropic, which requires a tensor C-response but no GDS transfer functions, or the case of a moderate 3D-structure, when the terms for transfer functions C_2 and C_3 may be dropped.

We return in conclusion to the postponed task to define the elements of $\underline{\underline{C}}$ in terms of the electric field and its derivative with respect to depth. For this purpose we define horizontal vectors $\underline{E}_h = (E_x, E_y)^T$, $\underline{B}_h = (B_x, B_y)^T$, $\dot{\underline{E}}_h = (\partial E_y/\partial z, -\partial E_x/\partial z)^T$ and introduce the matrix $\underline{\underline{A}}$ to connect the horizontal magnetic vector with its normal part, i.e. $\underline{B}_h = \underline{\underline{A}}\underline{B}_{nh}$. In these notations Faraday's law of eqs (2) now reads $\dot{\underline{E}}_h = i\omega\underline{\underline{A}}\underline{B}_{nh}$ and the impedance relations of eqs (26) $\underline{E}_h = (i\omega\underline{\underline{C}} + \underline{\underline{Z}}^{TM})\underline{B}_{nh}$, which when combined yield in

$$\dot{\underline{E}}_h = \underline{\underline{A}}(\underline{\underline{C}} + \underline{\underline{Z}}^{TM}/i\omega)^{-1}\underline{E}_h \tag{40}$$

the desired expression. In the special case of 2D structures, striking in x or y direction, the impedance tensor has zero diagonal elements and matrix $\underline{\underline{A}}$ zero off-diagonal elements. For a strike

in x-direction the field for E-polarisation is a TE field, while E, for B-polarisation contains both modes, the TE mode for its normal part and the TM mode for its anomalous part, and no anomalous magnetic field exists. Thus $a_{xx} = 1$ and in the inverse matrix $\underline{\underline{A}}^{-1}$ element a_{yy} has to be replaced by its reciprocal. This gives in close resemblance to eq. (1) $C_{xy} = \frac{a_{yy}E_x}{-\partial E_x/\partial z|_{z=0}}$ and $-C_{yx} = \frac{E_x}{-\partial E_y/\partial z|_{z=0}} + Z_{yx}^{TM}$; $-C_{yx}$ is again the scalar C-response of the surrounding normal structure.

a) Other related methods

So far their application has been mostly in spherical coordinates and with spherical harmonics. For completeness also their flat-Earth equivalents will be added, which eventually may find more widespread attention in MVS studies in polar and equatorial jet-regions. When in global studies series of spherical harmonics are derived not only for the potential but also for the vertical component, external and internal parts of the potential coefficients $\hat{U}_n^m = E_n^m + I_n^m$, as they appear in eq. (24), can be separated with Gauss' method. Set in relation to each other in

$$I_n^m = Q_n \cdot E_n^m, \tag{41}$$

this represents an univariate regression problem to be solved towards transfer function Q_n of the *potential method*. Eq. (25) shows how to convert it into $\hat{C}_n$. Ideally resulting estimates should agree within error limits for spherical harmonics of the same degree, but different order. Extensions to 3D global structures are possible, at least in principle. In Cartesian coordinates spatial Fourier transforms replace spherical harmonics, and eqs (10) and (11) have to be used to obtain C-responses for the (ω, k)-domain.

The potential method leads to response estimates for the Earth as a whole, and it is therefore not of immediate relevance, when we wish to investigate the substructure on a more regional scale. Results from a previous study (Schmucker, 1999b) will serve, however, as a global reference for the forthcoming locally focussed soundings. The methods to be considered now have in common with the gradient method that they involve the vertical magnetic component as observed at single sites which avoids the problematic need to develop this component into spherical harmonics. Furthermore, the condition of lateral uniformity can be relaxed to apply only to distances from the sounding site, which are comparable to the penetration depth. All further derivations proceed from eq. (23) for gradient sounding in terms of spherical harmonics.

After replacing in this equation the coefficients for the horizontal field components by those of the potential, with the aid of eqs (19) and (20), we obtain by a spherical harmonic synthesis

$$B_r(\theta,\lambda) = -\sum_{n,m} \hat{C}_n / R \sin\theta \cdot \left[-d\left(\sin\theta Q_n^m\right)/d\theta + m^2/\sin\theta P_n^m \right] e^{im\lambda} \hat{U}_n^m$$

with $Q_n^m = dP_n^m/d\theta$. When replacing $\hat{B}_{\vartheta,n}^m$ by $\hat{U}_n^m$ it has been observed that their relation depends on co-latitude. Eq. (18), the differential equation for elementary surface harmonics, reduces this expression to

$$B_r(\theta,\lambda) = -\sum_{n,m} n(n+1)\hat{C}_n/R \cdot \hat{U}_n^m Y_n^m(\theta,\lambda). \tag{42}$$

This is the basic equation of the *Z:Y method* in its original multivariate form with the intention to estimate a sequence of C-responses for fields of unrestricted geometry (Schmucker, 1979). If these responses are nearly the same, either because the range of degrees is quite limited or because

responses for a wider range are all close to their asymptotic value, eq. (42) reduces to the basic equation of the *univariate Z:Y method*:

$$B_r(\theta,\lambda) = -C_0/R \cdot \sum_{n,m} n(n+1) \cdot \hat{U}_n^m Y_n^m(\theta,\lambda). \tag{43}$$

From $B_\theta = -\sum_{n,m} \partial Y_n^m/\partial\theta \cdot \hat{U}_n^m$ and $B_\lambda = -\sum_{n,m} imY_n^m \cdot \hat{U}_n^m/\sin\theta$ it follows again with the aid of eq. (18) that $[\partial(\sin\vartheta B_\vartheta)/\partial\vartheta + \partial B_\lambda/\partial\lambda]/\sin\theta = \sum_{n,m} n(n+1)Y_n^m\hat{U}_n^m$, which shows that eq. (43) resembles eq. (15) for the gradient method in spherical coordinates. Both methods differ only in the way in which the horizontal spatial gradients are derived, either from global fields expanded into spherical harmonics or from regional fields approximated for example by polynomials (cf. Fig. 15). The respective C-response C_0 can be interpreted either as the spherical $\hat{C}_n$-response for the degree of the spherical harmonic which has the largest contribution, or as the zero wave-number response of a flat Earth. As in the case of the gradient method also the univariate Z:Y method can be combined with geomagnetic depth sounding by adding two terms for GDS transfer functions for a trivariate expression.

In Cartesian coordinates the relations, which connect the spatial Fourier transforms $\hat{B}_x$ and $\hat{B}_y$ to the spatial Fourier transform of the potential, are $\hat{B}_x = -ik_x\hat{U}$ and $\hat{B}_y = -ik_y\hat{U}$ as it follows readily from $B_x = -\partial U/\partial x$ and $B_y = -\partial U/\partial y$. Insertion of these relations into eq. (9) gives $\hat{B}_z = \hat{C}(\omega,k)\cdot k^2\hat{U}$ and thereby leads to the flat-Earth version of eq. (42) in

$$B_z(\underline{r}) = \frac{1}{4\pi^2}\int \hat{C}(\omega,k)k^2\hat{U}(\omega,\underline{k})exp(i\underline{k}\cdot\underline{r})d\underline{k}. \tag{44}$$

If for $k \le k_{max}$ the wave-number response can be replaced by the asymptotic response $\hat{C}(\omega,0) = C(\omega)$ and if in addition $\hat{U}$ vanishes for $k > k_{max}$, eq. (44) turns into

$$B_z(\underline{r}) = C(\omega)\frac{1}{4\pi^2}\int k^2\hat{U}(\omega,\underline{k})exp(i\underline{k}\cdot\underline{r})d\underline{k} \tag{45}$$

as basic equation for the univariate Z:Y method on a flat Earth, assuming now induction by a quasi-uniform source field.

Expansions of globally observed data into spherical harmonics can be avoided altogether, when the inducing source field is well represented by a single spherical harmonic, a possibility which lead Eckhardt et al. (1963) to the first local estimates of D_{st} responses. Writing then for any field component F on $r = R$ simply $F(\theta,\lambda) = \hat{F}_n^m Y_n^m(\theta,\lambda)$, eq. (42) reduces $B_r = -n(n+1)\hat{C}_n/R \cdot \hat{U}_n^m Y_n^m$. Insertion of eq. (19) or eq. (20) to replace $\hat{U}_n^m$ leads in

$$B_r(\theta,\lambda) = n(n+1)\cdot\hat{C}_n/R \cdot P_n^m/Q_n^m \cdot B_\vartheta(\theta,\lambda) \tag{46}$$

and

$$B_r(\theta,\lambda) = n(n+1)\cdot\hat{C}_n/R \cdot \sin\theta/im \cdot B_\lambda(\theta,\lambda) \tag{47}$$

to the basic equations for the *Z:H* and *Z:D method*, which allow local response estimates with data from a single site (Schmucker, 1970b, eq. 20). Their drawback is that the two methods yield conflicting results unless the ratio of the horizontal components is compatible with the assumed spherical function, i.e. for source fields involving non-zonal spherical harmonics the relation

$$B_\theta/B_\lambda = \frac{\sin\theta Q_n^m}{imP_n^m} \tag{48}$$

should be satisfied , as it is readily inferred from a comparison of eqs (46) and (47).

Various procedures have been devised to overcome this problem by involving both horizontal components in a single response estimate which is not in conflict with the stated condition. In the original conception of the method a transfer to rotated co-ordinates was suggested, ensuring a phase difference of 90 degrees between B_θ and B_λ, and to adopt a co-latitude which yields their amplitude ratio in agreement with eq. (48). In later attempts a second spherical harmonic was added with the same order but a different degree n'. Appendix B shows how to connect the ratio $\hat{U}^m_{n'}/\hat{U}^m_n$ of the two potential coefficients to the ratio B_θ/B_λ, leading to a correction factor $f_{nn'}$. for B_λ in the Z:D method (Schmucker, 1986). Alternatively. the coefficient ratio can be inferred from the results of a global analysis of the same type of variations with a presumably similar spatial structure (Bahr, 1985, 1989). In a third approach we return to eq. (23) for the gradient method in terms of spherical harmonics and obtain for the Z:D method the alternative formula

$$B_r(\vartheta,\lambda) = -im\hat{C}_n/R\sin\vartheta \cdot B_\lambda(\vartheta,\lambda)\cdot\left[1+f_\beta\right] \tag{49}$$

with

$$f_\beta = \frac{d\left(\sin\theta P^m_n\right)/d\theta}{imP^m_n}\cdot B_\theta/B_\lambda$$

as correct ion factor.

Turning in conclusion to the corresponding expressions in Cartesian co-ordinates, the inducing source field is assumed to be given by a single spatial harmonic with $exp(i\underline{kr})$ as location factor. The implication is that Fourier amplitudes $\hat{F}(\underline{k})$ are zero except for a narrow range $(\underline{k}\pm\underline{\Delta k}/2)$, yielding $F(\underline{r}) = 1/4\pi^2\cdot\hat{F}(\underline{k})exp(i\underline{kr})\Delta k_x\Delta k_y$, which converts eq. (44) into $B_z(\underline{r}) = \hat{C}(\omega,k)\mathrm{k}^2U(\omega,\underline{r})$. After replacing the potential either with iB_x/k_x or with iB_y/k_y, the formulas for local response estimates on a flat Earth, with observations at a single site, are

$$B_z(x,y) = ik^2/k_x\cdot\hat{C}(\omega,k)B_x(x,y) \text{ or } B_z(x,y) = ik^2/k_y\cdot\hat{C}(\omega,k)B_y(x,y) \tag{50}$$

with condition $B_x/B_y = k_x/k_y$ for consistent results.

3 TIME SERIES ANALYSIS

The processing of data begins with the harmonic analysis of selected time-sections, henceforth called *events*. They have all the same length T, in full days, and contain $(N+1)$ discrete hourly values, i.e. $T = N\Delta t$ with Δt equal to one hour. A multitude of short gaps is closed beforehand by linear interpolation, extending over up to four hours during the night and over up to two hours during daytime. In the preparation of irregular variations also longer gaps are bridged by inserting quiet times daily variations as outlined below. Any event with still incomplete data is excluded. But if only the last value is missing, which is the midnight value of the first day after the event, it will be replaced by the value before midnight on the preceding day. If the first and last values are different, the first value is replaced by their mean and the sine-harmonics are corrected afterwards accordingly (cf. Chapman & Bartels, 1940, section 16.15). Omitting then the last value, the harmonic analysis of the remaining N values yields cosine and sine coefficients a_m and b_m for M harmonics, with $m = 1,2,\ldots,M \le N/2$. They are combined to complex *Fourier amplitudes* $c_m = a_m - ib_m$ for angular frequency $\omega_m = 2\pi m/T$.

Regular daily variations S_r are processed separately from irregular transient variations S_{cont}. In the first case with $T = 1\,day$ single days are analysed from midnight to midnight in Universal time, and $M = 6$ harmonics are derived. In the analysis of S_{cont} the harmonic analysis is performed in time-sections of many days, and smoothed spectral values are obtained for frequency bands of constant width Δf. The choice of the length of the time sections is not critical as long as the number of harmonics $T\Delta f$ within frequency bands is sufficiently large to allow adequate smoothing with spectral filters. In view of the numerous data gaps, which may extend over days or even weeks, time-sections should be as short as possible, and for the adopted bandwidth of $\Delta f = 1\,cpd$ the decision for $T = 10\,days$ appears to be a reasonable compromise. An alternative would have been to use longer, but overlapping sections. Tests have shown that overlapping sections of 20 or 40 days do not improve results. So this alternative is not used. The time series are high-pass filtered with a cut-off at $0.5\,cpd$ prior to the analysis in order to suppress contributions from the D_{st} recovery phase of storms (cf. Section 1).

The sample record in Fig. 1 show S_r and S_{cont} as clearly distinguishable types of variations. The chosen ten-day section begins with three days of exceptional magnetic quietness, during which the planetary three-hour-indices Kp are either zero or one. Then follow days of steadily increasing magnetic activity during which Kp rises to 5 and even to 6 on the seventh day. On the quiet days we note very regular daily variations, representing *Sq-variations* in the monthly average, extending as $S_d = S_q + S_D$ with enlarged amplitudes well into the disturbed time (cf. Chapman & Bartels, 1940, chapter 6.8). But superimposed are increasingly dominating irregular polar substorm variations (*DP*). The five chosen observatories lie along the 15°E meridian crossing Europe, starting with L'Aquila (AQU) near Rome, followed by Fürstenfeldbruck (FUR) and Wingst (WNG) in Southern and Northern Germany, Rude Skov (RSV) near Copenhagen and Lovö (LOV) near Stockholm. It is noteworthy that during the first three days *Sq*-variations remain clearly visible up to LOV, which is quite close to the auroral zone.

The gradual changes with latitude during the first three days correspond to the configuration of the overhead *Sq*-current system, whose centre lies in late spring over the Mediterranean Sea. Accordingly daily variations of the vertical component have their greatest amplitude at the southern sites and at AQU also their smallest amplitude in the north component. But during the following disturbed days this component shows at AQU stronger and stronger variations and those of the vertical component increase dramatically northward, indicating intensifying contributions from S_D and *DP* with origins in the auroral zone. For our purposes it is essential that variations of both horizontal components appear to be well correlated along the $2000\,km$ long profile and thereby well suited for the intended fit by low-degree polynomials. In particular variations of the east component look so much alike that derivatives with respect to latitude should hardly exceed a few Nanotesla per 1000 kilometres. We shall see that these small derivatives, however, account for the observed variations of the vertical component, indicating that they reflect mainly induction in a stratified Earth by non-uniform source fields rather than local induction anomalies.

The following illustrations augment these findings in the frequency domain by spectra. Figure 2 shows the harmonic amplitude spectra $\mid c_m \mid$ for the ten-day time-sections of Fig. 1. Bars above the last spectral line indicate the amplitude spectrum $\sqrt{4\sigma^2/N}$ of harmonically analysed random variables of variance σ^2, estimated from $\sigma^2 = 1/2 \cdot \sum_{1}^{N/2} \mid c_m \mid^2$ according to Parseval's theorem. From the total of $N/2 = 120$ harmonics only the first eighty are displayed. The bars agree reasonably well with the level of the continuum spectra up to $5\,cpd$, indicating that the irregular variations are indeed basically of random nature. Note that the lengths of the bars increase systematically

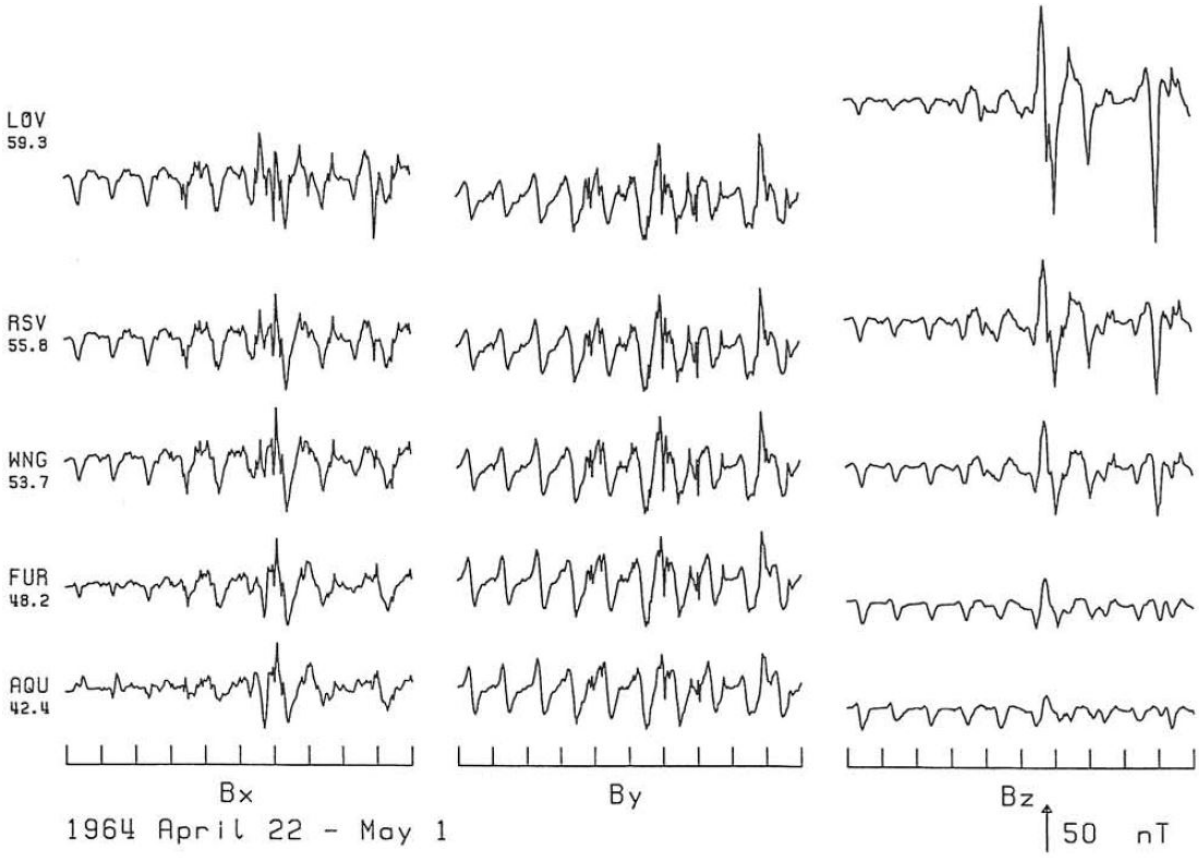

Figure 1: Ten-day record samples of geomagnetic variations in April 1964, shown for five observatories on a north-south profile from Sweden to Italy: Lovoe (LOV), Rude Skov (RSV), Wingst (WNG), Fürstenfeldbruck (FUR), L'Aquila (AQU). Numbers below observatory acronyms are geographic latitudes. Plotted are hourly mean values for the north-component B_x, the east-component B_y, and the vertical component B_z. - After three days of magnetic quietness with undisturbed quasi-periodic daily variations follow days of increasing magnetic activity, with a maximum on the sixth day. During the disturbed days intensified daily variations and later on superimposed transient storm-time variations, with peak excursions notably in B_z. At all times well correlated variations along the profile. Nearly latitude-independent daily variations in B_y are in contrast to visible changes in B_z and B_x, as to be expected for an overhead *Sq*-current loop centred at local noon above Southern Europe.

towards north, especially for B_z, indicating the expected rise of the continuum level towards the auroral zone. We observe further that the spectral peaks of S_r at the diurnal frequencies stand out clearly above the continuum level except for B_x at the southern site, as to be expected, and that further north spectral peaks of higher harmonics gradually disappear into the continuum.

Figure 3 repeats the display of spectra on a logarithmic scale, now for unsmoothed power spectra $\mid c_m \mid^2 \cdot T/4$ in the average over all 72 ten-day time-sections, which fit into the two years 1964-65. *Sq*-variations of the respective month have been removed before the harmonic analysis to obtain a better view of the spectrum of irregular variations. The bars at the end of the spectra, representing the power spectral densities $(T/N \cdot \sigma^2)$ of random variables, are again representative for the power spectra up to, say, $3\,cpd$. We see now clearer than in Fig. 2 the gradual decline of spectral densities towards $8\,cpd$, but the slopes appear as sufficiently gentle for the intended spectral analysis with bandwidths of $1\,cpd$. Evidently the removal of *Sq*-variations has been quite effective in the necessary pre-whitening of the spectra prior to the analysis. The remaining slopes appear to be slightly greater for the vertical than for the horizontal components, possibly because of a decreasing penetration depth with increasing frequency.

Figure 3 demonstrates also that the removal of S_q has not brought down their spectral peaks exactly to the level of the continuum at the diurnal frequencies, and interestingly the remaining small peaks can be recognised occasionally up to the eights harmonic. Recalling from Fig. 2 that daily variations increase in amplitude during disturbed days, the not removed part of S_r could represent the *disturbance daily variations* S_D. Noteworthy are certain persistent characteristics of the power spectra, for example the slight dents halfway between the diurnal frequencies, while spectra of random variables should scatter at random around their means, possibly indicating that the harmonics of individual time-sections are not totally independent. This observation will receive further attention in Section 5.2, when considering the degrees of freedom for an adequate estimate of errors.

Returning to the processing of S_{cont}, a sequence of preparatory steps has been applied to the time series in their full length. Each step was tested for its effectiveness to improve the final outcome, and even though some of the improvements are small, their combined effect is significant. The first step concerns the removal of the geomagnetic main field and its secular variations. For this purpose the time series are searched for quiet days in the greatest possible distance after storms to minimize contribution from the D_{st} recovery phase. In the average two suitable days per months could be found. Then a second degree polynomial is fitted by least squares to the unequally spaced local midnight means of the selected days, from midnight to three o'clock local time, and subtracted from the time series hour by hour.

Because too many time-sections would be lost with gaps longer than four and two hours, respectively, and noting that many of these gaps are one day long, with one or two additional hours, all gaps with up to two days are bridged with the *Sq*-variations of the respective month, assigning to each hourly interval in Universal time the interval in local time with the greatest overlap. Care has been taken that this replacement does not produce offsets at neither end of the gap by adding a suitable slope. Afterwards the time series are high-pass filtered to suppress any remaining low frequency constituents from D_{st}. The chosen trapezoidal filter has a cut-off frequency of $0.5\,cpd$ and a one-sided length of two days. The filter response was found to be steep enough to allow reliable estimates of transfer functions for the first frequency band centred at the cut-off frequency. Tests with longer filters and thus increased steepness as well as tests with lower cut-off frequencies have not lead to significantly improved results. In the final step the *Sq*-variations of the month are subtracted hour by hour, and the resulting time series is broken up into non-overlapping ten-day

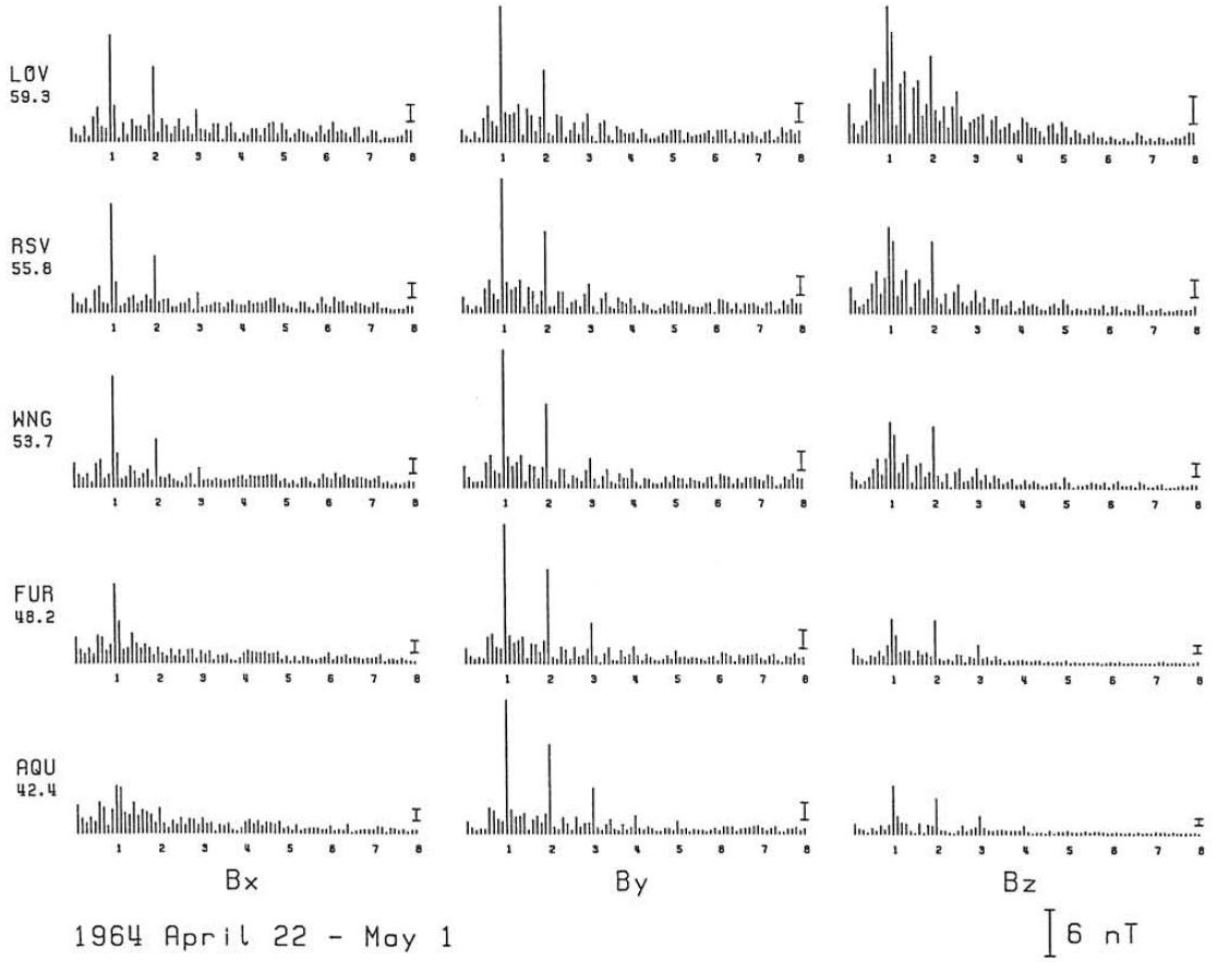

Figure 2: Amplitude spectra for the ten-day record samples of Fig. 1 on a linear scale. Frequency spacing of lines is 0.10 cycles per day (*cpd*) and numbers below horizontal axes are frequencies in *cpd*. Vertical bars above the end of each spectrum indicate amplitudes of white noise with the same variance. Arrangements according to sites and components as in Fig. 1. - The line spectrum of daily variations is mostly well above the level of the background continuum, at least up to the fourth harmonic, and this level is well represented by the amplitude of white noise. For B_z spectral lines and background continuum increase continuously towards north, reflecting increasing contributions from activity-related quasi-period S_D and transient *DP*-variations.

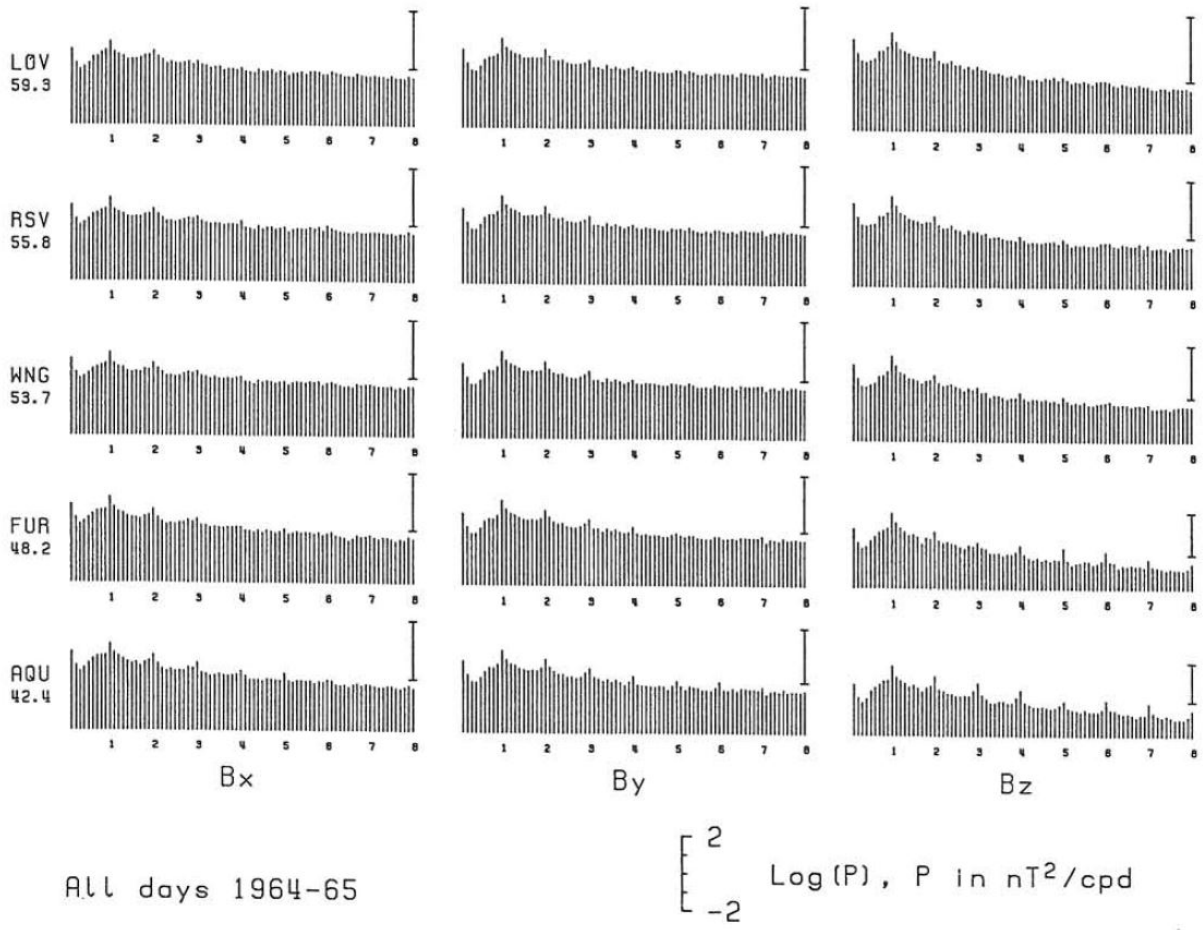

Figure 3: Power spectra (P) in the same arrangement as in Fig. 2, but on a logarithmic scale. These are average spectra of all 72 ten-day time-sections fitted into the years 1964-65. Prior to the analysis monthly *Sq*-variations have been removed hour-by-hour. Vertical bars above the end of the spectra show the spectral density of white noise with the variance of the full two years. - The removal of *Sq*-variations leaves small spectral peaks at the diurnal frequencies, which may be associated with S_D. They remain visible at the southern sites up to almost $8\,cpd$, notably in B_z. There exists an overall increase of spectral densities towards the auroral zone and a gentle decline from $4\,cpd$ onwards below the level of white noise everywhere.

sections in a way that the last hourly value is also the first hourly value of the next section.

The concluding step of data processing starts with the conversion of Fourier amplitudes into *event spectra* $\hat{S}_{kl}$. In the S_r-analysis they are simply *Fourier products*, for example

$$\hat{S}_{xy}(m,n) = B_x(m,n) \cdot B_y^*(m,n) \tag{51}$$

defines the cross-spectrum between B_x, and B_y for the m-th harmonic on the n-th day; with the star denoting the complex conjugate. The corresponding event spectrum in the S_{cont}-analysis is the weighted band-average of Fourier products according to

$$\hat{S}_{xy}(m,n) = \sum_{m'=-L}^{+L} w_{m'} B_x(m-m',n) \cdot B_y^*(m-m',n) \tag{52}$$

for the m-th frequency band of the n-th time-section; $w_{m'} = w_{-m}$ are the weights of the chosen spectral filter. Should $(m-m')$ become negative, the complex conjugate of the Fourier amplitude for $(m'-m)$ is substituted.

We shall use Parzen filters with $L = 10$ and $\tau_{max} = 2$ *days* in the lag-domain and thereby obtain $b = 1.86/\tau_{max} = 0.93\,cpd$ as equivalent bandwidth (cf. Jenkins & Watts, 1968, Table 6.6). Because the filter extends halfway into the adjacent frequency bands, the resulting smoothed spectral values are not completely independent. But with $w_5/w_0 = (2/\pi)^4 = 0.165$ for the weights at the band boundaries in relation to the weights at mid-frequency, the overlap appears as tolerable in view of the achieved bandwidth of nearly $1\,cpd$. As a rule, mid-frequencies are placed halfway between the diurnal frequencies, from $0.5\,cpd$ to $7.5\,cpd$. A shift to diurnal frequencies would have given contributions from S_D maximum weights, but test have not shown any marked improvement of the final transfer function estimates.

The weighted summation of event spectra $\hat{S}_{kl}$ leads in the concluding step of data processing to *(global) spectra* S_{kl}. For example

$$S_{xy}(m) = \sum_{n=1}^{N} Q_{mn} \hat{S}_{xy}(m,n) \tag{53}$$

is the (global) cross-spectrum between B_x and B_y for the m-th frequency band. The estimation of transfer functions will proceed from these discrete spectral values. The method to derive spectral weights Q_{mn} will be the subject of Section 5.3.

4 POLYNOMIALS

4.1 Consideration of alternatives and formulation of basic equations

As already stated, the polynomials to be derived have no other purpose than to provide a spatially smoothed field distribution, which is firstly easy to differentiate and secondly suitable for presenting the horizontal components B_{nx} and B_{ny} of the *normal* field which we would expect in the absence of any induction anomalies. They approximate the observed horizontal components within a network of sites, either their Fourier amplitudes frequency-by-frequency or their time series hour-by-hour. Ideally, the residuals of the polynomial fit should be the horizontal components of a magnetic potential field arising from internal induction anomalies, i.e. they should have a relationship to

its vertical component, as expressed by the GDS transfer functions , which is compatible with an internal origin of the field. But the implementation of this condition is beyond the scope of this contribution. The fact that ordinary polynomials do not involve orthogonal functions is of little bearing because we shall use low-degree polynomials only, and since the fields to be fitted at a given instant of time hardly change signs within Europe, as seen in Fig. 1, expansions into series of oscillatory orthogonal base functions such as spherical harmonics would not be suitable. Alternatives would have been a least squares fit with cubic splines or spherical cap harmonics, but neither possibility has been tested (cf. Wang & Dahlen, 1995; Torta & DeSantis, 1996).

Attention has received, however, the multivariate linear statistical method (*MLS*) as introduced by Egbert (1997, Section 2) into induction work. The assumed linearity means in this context that B_x (or B_y) is related linearly to B_y (or B_x) at the same site and to B_x and B_y at all other sites. The least squares formulation for an assemblage of events leads to a system of homogeneous normal equations and thus to an eigen-value problem. Spatial smoothing is achieved by reconstructing the field components from a limited number of eigen-solutions, associated with the largest eigen-values, retaining in this way those parts of the horizontal components, which have the greatest spatial coherence. The principal drawback of the method is the necessity to have complete data for all events and sites, while polynomials can be derived event by event with varying sets of sites, just as data are available. In view of the many unfilled data gaps, our preference for polynomials is more circumstantial, not counting the problem to differentiate MLS-smoothed fields. Tests have been performed with a limited number of European sites, which have complete data for the chosen events. The resulting smoothed fields obtained with the two methods are quite similar, indicating that with low-degree polynomials we have filtered out also successfully the spatially most coherent part.

All further calculations are in spherical coordinates, as introduced in Section 2.2, assigning geographic co-ordinates (φ, λ) to points of observation P, with $\varphi = \pi/2 - \theta$ as latitude. Expansions into polynomials are not, however, in terms of these angular spherical coordinates, but in terms of *dimensioned* spherical (u, v) coordinates, resembling (x, y) coordinates on a flat Earth. For their definition the distance between P and some centrally located reference point P_0 at (φ_0, λ_0) is decomposed into spherical arcs $u_0 = R(\phi - \phi_0)$ and $v_0 = R\sin\theta(\lambda - \lambda_0)$, first along meridians and then along circles of latitude. Corresponding arcs $u_r = R(\phi_r - \phi_0)$ and $v_r = R\sin\theta_r(\lambda_r - \lambda_0)$ connect P and a second reference point P_r at (ϕ_r, λ_r), which will be the zero reference point for the polynomials to be developed in terms of

$$u = u_0 - u_r = R(\phi - \phi_r),\ v = v_0 - v_r = R\sin\theta(\lambda - \lambda_0) - R\sin\theta_r(\lambda_r - \lambda_0)\,. \tag{54}$$

This leads to polynomials which in their approximation are invariant against the position of P_r when P_0 remains fixed, and a natural choice is to let both points coincide. Later on, however, a deviating positions of P_r will be used under certain circumstances. A minor dependence remains anyhow on the chosen position of P_0 because the definition of the longitudinal coordinate v involves the sine of co-latitude. But even placing P_0 far away from Europe has been found to have only marginal effects. This is also a valuable demonstration that rounding-off errors do not influence the polynomials to any significant extent, noting that the least squares solution for the fit of second degree polynomials involves coordinates already up to their sixth powers. For all further calculations $\phi_0 = 50°N$ and $\lambda_0 = 10°E$, which places P_0 into Southern Germany, not far from the observatory Fürstenfeldbruck.

Turning to the basic equation for gradient sounding in spherical coordinates, we replace in eq. (15) the derivatives $\partial/\partial\theta$ and $\partial/\partial\lambda$ by $-R\partial/\partial u$ and $R\sin\theta\,\partial/\partial v$, respectively, multiply all compon-

ents with the sine of co-latitude, and obtain

$$B_z^* = C_0(\omega) \cdot \left(\frac{\partial B_{nu}^*}{\partial u} + \frac{\partial B_{nv}^*}{\partial v} \right), \tag{55}$$

where $B_{nu}^* = -\sin\theta B_{n\theta}$, $B_{nv}^* = +\sin\theta B_{n\lambda}$ and $B_z^* = -\sin\theta B_r$. The thus re-formulated basic equation for gradient sounding on a spherical Earth conveniently resembles eq . (5) for gradient sounding on a flat Earth. The likewise converted potential condition of eq. (37) becomes

$$\frac{\partial B_u^*}{\partial v} + \frac{\partial B_v^*}{\partial u} = 0, \tag{56}$$

in analogy to eq. (30).

We are ready now to formulate 2-dimensional second degree polynomials to approximate B_u^* and B_v^* at a given site. With self-explanatory notations of the expansion coefficients, they are

$$\begin{aligned} B_u^*(u,v) &= a_{00} + a_{10}u + a_{01}v + a_{20}u^2 + 2a_{11}uv + a_{02}v^2 + \delta B_u^*(u,v)\,, \\ B_v^*(u,v) &= b_{00} + b_{10}u + b_{01}v + b_{20}u^2 + 2b_{11}uv + b_{02}v^2 + \delta B_v^*(u,v)\,. \end{aligned} \tag{57}$$

Noting that the just stated potential condition leads to the identities

$$a_{01} = b_{10},\ a_{02} = b_{11},\ a_{11} = b_{20}\,, \tag{58}$$

the number of independent coefficients is reduced from twelve to nine.

4.2 Least squares fit of polynomials to observations

Using vector notations, the system of linear equations to be solved is $\underline{\underline{G}} \cdot \underline{m} = \underline{d} + \underline{\delta d}$, where $\underline{m}$ denotes the model vector for the unknown polynomial coefficients, $\underline{d}$ the data vector containing B_u^* and B_v^*, and $\underline{\delta d}$ the misfit vector for the residuals δB_u^* and δB_v^* in eqs (57). The $2N \times M$ matrix $\underline{\underline{G}}$ connects observations at N sites to M coefficients. Its elements are real and determined solely by the coordinates of the sites. The normal equations for a least squares solution minimizing $\| \underline{\delta d} \|^2$ have the symmetric matrix $\underline{\underline{G}}^T \underline{\underline{G}}$ as coefficient matrix which has to be inverted to find $\underline{m} = \left(\underline{\underline{G}}^T \underline{\underline{G}} \right)^{-1} \underline{\underline{G}}^T \underline{d}$. If $\lambda_1, \lambda_2, \ldots, \lambda_M$ are the (positive) eigen-values of matrix $\underline{\underline{G}}^T \underline{\underline{G}}$, ordered according to their size, a large *condition number* λ_1/λ_M indicates that the system of normal equations is ill-conditioned and that the solution will be unduly sensitive to data errors. These ratios are listed in the last column of Table 1 for variable numbers of observing sites and coefficients. The other entries are the *rms* misfit residuals ε in the average $(<>)$ over all events, i.e. $\varepsilon^2 = <\| \underline{\delta d} \|^2 / N' >$ with N' as the number of sites which have data for a specific event, secondly the *rms* data amplitudes β, with $\beta^2 = <\| \underline{d} \|^2 / 2N'$, thirdly the model vector norms $\gamma = \| \underline{m} \|$. Numbers in parentheses in the second column indicate how many sites with data have been available in the average.

The Winch-Fainberg collection of geomagnetic hourly values for the IQSY 1964-65 includes 35 observatories in Europe, omitting observatories in the polar region and east of Moscow (cf. Schmucker, 1999a, Section 2 and Table 1). The retained observatories are more or less evenly distributed over Europe between the Atlantic coast in the west, the western part of Russia in the east, Southern Scandinavia in the north, and the Mediterranean countries in the south. Their geographic coordinates and observatory acronyms can be found in the just quoted reference and in Part II of this

contribution. The events which are used for the entries into Table 1 are either the 124 quiet Q^*-days of the IQSY (cf. Schmucker, 1999a, Table 2) or the 72 ten-day sections which fit into these two years. Rows in Table 1 with $N = 35$ refer to results obtained by fitting polynomials to the Fourier amplitudes of the horizontal components within the entire European network, either for the second harmonic of daily variations or for the harmonics within the second frequency band of the spectral continuum, here in the average over all harmonics between $1\,cpd$ and $2\,cpd$.

For completeness entries in Table 1 start with third degree polynomials and $M = 14$ independent coefficients, out of 20. Their mean relative misfit residual ε/β amounts to 0.146 for S_r and to 0.221 for S_{cont}, which means that about 85% of the observed S_r-harmonics can be accounted for by third degree polynomials versus less than 80% for S_{cont}. Obviously the more smoothly varying S_r-variations can be better approximated by polynomials than activity-related irregular variations with their complicated spatial structure in high latitudes. It is noteworthy that the model vector norms are not yet excessive in comparison to those for lower degree polynomials, an indicator that the polynomials have not started yet to oscillate between data points. But condition numbers in excess of one thousand show clearly that data from 35 sites are insufficient for a reliable determination of fourteen coefficients. Lowering their number to $M = 9$ for second degree polynomials leads to much more stable solutions, with condition numbers well below 100, and by a further reduction to $M = 5$ for first degree polynomials it is reduced to less than ten, but at the expense of a substantially increased misfit by about one third.

Because we wish to obtain a spatially smoothed surface field suitable for the intended identification with the normal parts of of the horizontal components, no further consideration is given to third degree polynomials, which would require anyhow extensive regularisation. But in view of the considerable dependence of B_z on latitude, as it is evident in Fig. 1 and which in all likelihood is not of anomalous internal origin, we wish to retain non-linear polynomials with derivatives depending at least linearly on coordinates. Therefore our choice will be 2-dimensional second degree polynomials according to eqs (57), with the option to lower the number of coefficients to seven in the following way:

We return temporarily to Cartesian co-ordinates and observe that if a potential U of a magnetic field $\underline{B} = -gradU$ satisfies Laplace's equation, the field components will do the same, e.g. $\nabla^2 B_x = 0$. Rewriting second derivatives of B_x and B_y with respect to z as

$$\frac{\partial^2 B_x}{\partial z^2} = -\frac{\partial^3 U}{\partial x \partial z^2} = \frac{\partial}{\partial x}\left(\frac{\partial B_z}{\partial z}\right) \text{ and } \frac{\partial^2 B_y}{\partial z^2} = -\frac{\partial^3 U}{\partial y \partial z^2} = \frac{\partial}{\partial y}\left(\frac{\partial B_z}{\partial z}\right),$$

and replacing $\partial B_z/\partial z$ by $-B_z/C(\omega)$ according to eq. (6) under the assumption of a location-independent C-response leads to

$$\nabla^2 B_x = \frac{\partial^2 B_x}{\partial x^2} + \frac{\partial^2 B_x}{\partial y^2} - \frac{1}{C(\omega)} \cdot \frac{\partial B_z}{\partial x} = 0 \text{ and } \nabla^2 B_y = \frac{\partial^2 B_y}{\partial x^2} + \frac{\partial^2 B_y}{\partial y^2} - \frac{1}{C(\omega)} \cdot \frac{\partial B_z}{\partial y} = 0. \quad (59)$$

These equations connect second derivatives of the horizontal components to first derivatives of the vertical component above stratified conductors. Cartesian (x, y, z) co-ordinates are replaced now in an approximate manner by (u, v, z) co-ordinates, eqs (57) are multiplied with $\sin\theta$, and a linear polynomial

$$B_z^*(u, v) = c_{00} + c_{10} \cdot u + c_{01} \cdot v + \delta B_z^* \quad (60)$$

is fitted to the vertical component within the network of observing sites. Finally, derivatives are derived by differentiation of the respective polynomials. All this converts eqs (59) into

$$(a_{20} + a_{02}) = c_{01}/2C(\omega), (b_{20} + b_{02}) = c_{01}/2C(\omega). \quad (61)$$

Each one of the two equations allows us to replace one of the two quadratic coefficients for B_u^* and B_v^* by one linear coefficient for B_z^*. Eliminating in this way $a_{02} = b_{11}$ and $b_{20} = a_{11}$ in eqs (57) leads to

$$B_u^* = a_{00} + \ldots + [c_{01}/2C(\omega) - b_{02}] \cdot 2uv + [c_{10}/2C(\omega) - a_{20}] \cdot v^2$$

with a corresponding expression for B_u^*. We presume that the coefficients c_{10} and c_{01} have been determined beforehand and adopt for $C(\omega)$ preliminary model C-response $C_{mod}(\omega)$, the same for all sites. Then we collect all known quantities on the left-hand-sides and obtain in

$$\begin{aligned} B_u^{**}(u,v) &= B_u^*(u,v) - \left[c_{01} \cdot 2uv + c_{10}v^2\right]/2C_{mod}\,, \\ B_v^{**}(u,v) &= B_v^*(u,v) - \left[c_{10} \cdot 2uv + c_{01}u^2\right]/2C_{mod} \end{aligned} \tag{62}$$

modified variables to which second degree polynomials are fitted, now with seven instead of nine unknown coefficients:

$$\begin{aligned} B_u^{**} &= a_{00} + a_{10} \cdot u + a_{01} \cdot v + a_{20} \cdot \left(u^2 - v^2\right) - b_{02} \cdot 2uv + \delta B_u^{**}\,, \\ B_v^{**} &= b_{00} + a_{01} \cdot u + b_{01} \cdot v + b_{02} \cdot \left(v^2 - u^2\right) - a_{20} \cdot 2uv + \delta B_v^{**}\,. \end{aligned} \tag{63}$$

Rows of Table 1 with $M = 7$ and thus with results derived on their basis verify that the performed reduction in the number of unknowns has the desired effect of improved stability, while the relative *rms* misfit residuals have increased only slightly in comparison to those for fits with nine coefficients. The change of the *rms* data amplitudes reflects the use of modified input data according to eqs (62), derived with $C_{mod}(\omega)$ for a 3-layer spherical Earth model (cf. Schmucker, 1999b, Fig. 1).

Various possibilities exist for improvements by assigning weights to the data: according to their errors or according to polynomial misfit residuals or according to the distance from the reference point P_r. We see no reason not to assume that the hourly values are of equal quality at all times and at all sites, which rules out the first option. For an assessment of the second option individual observatory *rms* misfit residuals ε_{obs} are compared with each other in Fig. 4. Here $\varepsilon_{obs}^2 = <\mid \delta B_u \mid^2 + \mid \delta B_v \mid^2>$ and $<>$ denotes the average over all analysed events. There seems to exist a slight tendency of residuals ε_{obs} to decrease toward north, but otherwise with few exceptions all observatories have residuals of about the same size, as well for the displayed second time harmonic of S_r as for the second frequency band of S_{cont}, in that case in the average of ε_{obs}^2 over all harmonics within the respective band. We note that observatories with excessive residuals reoccur in both analyses, and detailed inspections have shown that these observatories have persistently large residuals for all events and frequencies.

Therefore it has been decided not to use IQSY data from the observatories LGR, ROB, SUA, CLF. The observatory TOL will be excluded in the analysis of daily variations and the observatory ODE in the continuum analysis, leaving in either case 30 observatories for the derivation of polynomials. The observatory COI will be retained, even though its residual is quite large for the displayed second harmonic of the S_r analysis, because residuals for all other harmonics are all at a tolerable level. When polynomials have to be derived for the vertical component according to eq. (60), five more observatories are omitted: COI and ALM at the south-western tip of the Iberian Peninsula and VAL on the Irish west-coast have strongly anomalous B_z-variations due to ocean effects, at SWI this component appears to be highly disturbed, and SFS has no Z-variometer. Otherwise no explanation can be offered, why certain observatories have variations, which do not fit to those at surrounding sites. It could be due to large local induction anomalies, modifying their internal parts. But this seems to be a rather remote possibility.

With regard to the third option, experience has shown that data can have adverse effects on the polynomial fit, when they come from observatories which are far away from the reference point P_r. After shifting it to the site where the sounding is to be performed, data will be omitted from observatories, whose distance $D = \sqrt{u^2 + v^2}$ exceeds a certain maximum value D_{max}, accepting that the invariance of polynomials against the position of P_r is lost. The chosen distance of exclusion should be neither too large to be effective nor too small, which would leave too few observatories for stable solutions by least squares. Tests have shown that for the European network the choice $D_{max} = 1500\,km$ represents a good compromise, at least for observatories in central positions, where this choice leaves data from about 20 sites for the polynomial fit.

Returning to Table 1, we observe that for analyses with $N = 30$ observatories the overall fit by polynomials is improved against analyses with all 35 observatories, while condition numbers remain more or less unchanged. For second degree polynomials with $M = 9$, for instance, the relative misfit is lowered from 16% to 12% for S_r and from 22% to 19% for S_{cont}. Admittedly these improvements are due largely to the exclusion of the observatory ROB. When with $D_{max} = 1500\,km$ and the Bavarian observatory FUR as zero reference point only data from 22 observatories are used, the decrease of the condition number from 59 to 20 indicates that the stability has been improved considerably by a concentration on not too distant sites. However, instabilities return with a condition number of 78, when the distance of exclusion is lowered further to $1000\,km$, leaving only fourteen sites within this distance from FUR. The lower part of Table 1 summarizes the results for $N = 30$ and $M = 7$ for six frequencies and six frequency bands, respectively, and this will be the preferred combination of sites in all forthcoming MVS soundings. We see that the misfit residuals decrease steadily with increasing frequency, but when set in relation to the also decreasing amplitudes, the overall relative misfit increases, in the case of S_r smoothly from 12% for the first harmonic to 26% for the fourth harmonic and then abruptly to about 40% for the fifth ad sixth harmonic. For S_{cont} the rise is more or less continuous from 18% for the first to 26% for the sixth frequency band. A similar difference in the two analyses will be found, when considering the spatial coherence as function of frequency, thus connecting the increase of misfit residuals to the loss of spatial coherence.

Two further possible improvements concern only the analysis of S_r. Noting that daily variations are mainly functions of local time $T = t + \lambda$, with times in angular measure, it could be of advantage to fit polynomials to their Fourier amplitudes in local time, i.e. with time factor $exp(i\omega T)$. This leads to complications, however, when differentiating them with respect to longitude. The then necessary modifications are outlined in Appendix C. Secondly, recalling a remark from Section 2.1 that the basic equation for gradient sounding represents the first term of a series, a second series term can be included in a very approximate manner by adding a correction factor $(1 + i\varepsilon)^{-1}$ to the horizontal spatial gradient, with ε in the order of 0.05. Details can be found at the end of Appendix A.

4.3 Time series of polynomial coefficients and horizontal spatial gradients

It will be interesting to see how the polynomials respond to changing source field geometries in times of low and high magnetic activity. For this purpose the 240 hourly values within a ten-day section, the same as in Fig. 1, are developed hour-by-hour into second degree polynomials. Figs 5 and 6 show the resulting time series of coefficients. Starting at the bottom with coefficients a_{00} and b_{00} for the absolute terms, which are the polynomial approximations for B_u and B_v at the zero reference point $P_r = P_0$ we note by comparison with Fig. 1 that their time series resemble closely the observed variations at the nearby observatory FUR. Since the polynomial fit involves data from

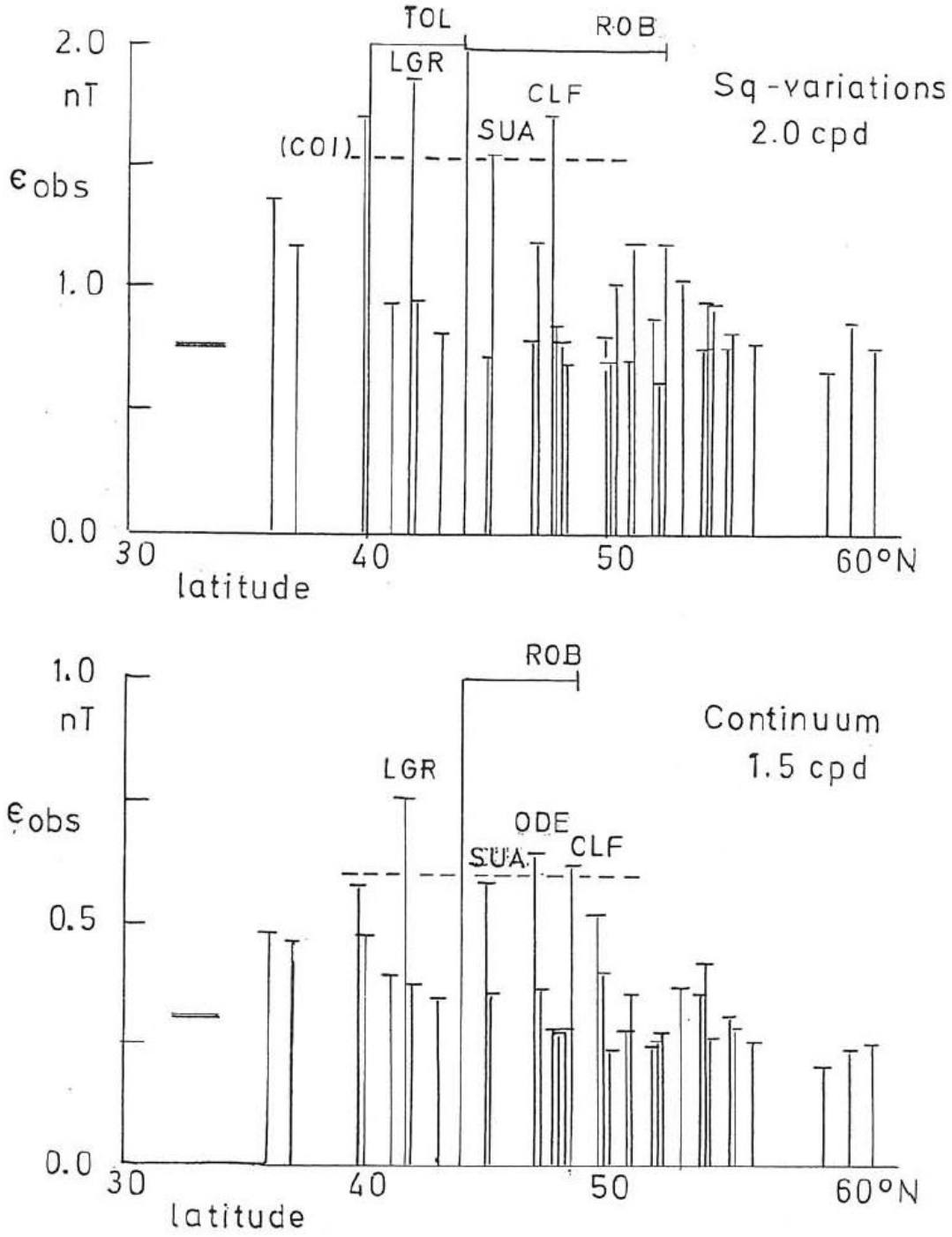

Figure 4: Residuals ε_{obs} for second degree 2-dimensional polynomials fitted to the harmonics of horizontal components at 35 European observatories, either to the second harmonics of daily variations (top), or to the harmonics within the second frequency band of the continuum (bottom). The residuals represent individual *rms* averages over 124 Q*-days or 72 ten-day sections, arranged according to the latitude of the respective observatory. Thick horizontal bars indicate the overall *rms* averages of all events and sites. - The majority of observatories have residuals close to this average. Those five observatories with residuals at least twice as large and thus crossing the dashed line will not be used any further for fitting polynomials. Cf. text for the special case of the observatory COI in Portugal.

all over Europe, this resemblance is a clear indication that the polynomials provide indeed a good presentation of a spatially coherent variation field, during the first days of magnetic quietness as well as during the later disturbed days.

We recall that the north component of *Sq*-variations is quite small in Southern Europe below the centre of the overhead current loop, but its north-south gradient is strongest here and thus the coefficient a_{01} dominates among the coefficients for linear terms. On the greatly disturbed sixth day they increase fivefold in comparison to the preceding quiet days, which is more than one might have expected from the sample records in Fig. 1. In the time series of coefficients b_{01} and a_{01} the dependence becomes visible which daily variations have on local time and thereby on longitude. During the first quiet days they are almost comparable in size with the coefficient a_{10}, but their increase toward the disturbed days is less conspicuous. In rough approximation *Sq*-variations of the east component are proportional to $\sin T$, which implies that $\partial B_v/\partial\lambda$ and thereby b_{01} should be proportional to $\cos T$, which is indeed the case, i.e. b_{01} has its minimum at local noon when this component passes through zero. Similarly for an approximate local time dependence of the north component according to $(1-\cos T)$, the coefficient a_{01} should oscillate like $\sin T$ which is also more or less the case. Hence, these coefficients fit well into concepts about source field geometries and thus have a distinct physical meaning.

Among the quadratic coefficients in Fig. 6 the most prominent coefficient is a_{20} at all times. During the first quiet days it is opposite in sign to coefficient a_{10}, indicating that the north-south gradient of *Sq*-variations in the north component flattens with increasing latitude, as to be expected when crossing the westward flow of overhead *Sq*-currents near noon. But both coefficients have the same sign during hours of peak activity, when a positive coefficient a_{20} implies increasing gradients toward north and thus toward the auroral zone. It is noteworthy that also the remaining much smaller quadratic coefficients display a clear diurnal periodicity, at least during the first quiet days, proving that they are not merely spurious artefacts of the polynomial expansions. This favourable impression is strengthened by the time series in the lower part of Fig. 6 to test the validity of eqs (61). It verifies that the sums s_1 and s_2 of quadratic coefficients are indeed well reproduced by their predictions s_{1^*} and s_{2^*}, involving time series of the linear coefficients c_{10} and c_{01} for the vertical component. The adopted model response C_{mod} is that of a perfect conductor at $600\,km$ depth. Because it is real and the same for all frequencies, convolutions with its delta-function shaped time-domain response become products, i.e. $s_{1^*} = c_{10}/2C_{mod}$ and $s_{2^*} = c_{01}/2C_{mod}$.

With regard to the size of the various coefficients, those for linear terms are in the order of a few Picotesla (pT) per kilometre and thus lead to differences of a few Nanotesla (nT) across Europe. The same applies roughly to the quadratic coefficients which are in the order of nT/Mm^2, where $Mm = 10^6\,m$ stands for $1000\,km$. It is noteworthy that these rather small differences have allowed the determination of physically meaningful polynomials, whose coefficients in their temporal development relate well to the expected time-space structure of the respective variation fields. It testifies for a remarkable calibration accuracy of the variometers in use during the IQSY at all participating European observatories.

In concluding this section, we return for a last time to the ten-day interval of Fig. 1 and compare in Fig. 7 the vertical component (B_z^*), in nT, with the horizontal spatial gradient (G) , in pT/km, obtained with the polynomial coefficients of Figs 5 and 6 by combining eq. (55) with eqs (57), i.e.

$$G = a_{10} + b_{01} + (a_{20} + a_{02}) \cdot 2u + (b_{20} + b_{02}) \cdot 2v.$$

With a scaling ratio of 20 : 33 both time series would look alike, when $B_z^* = C \cdot G$ were derived from G for a perfect conductor at $C = 600\,km$ depth. We observe indeed a remarkable similarity

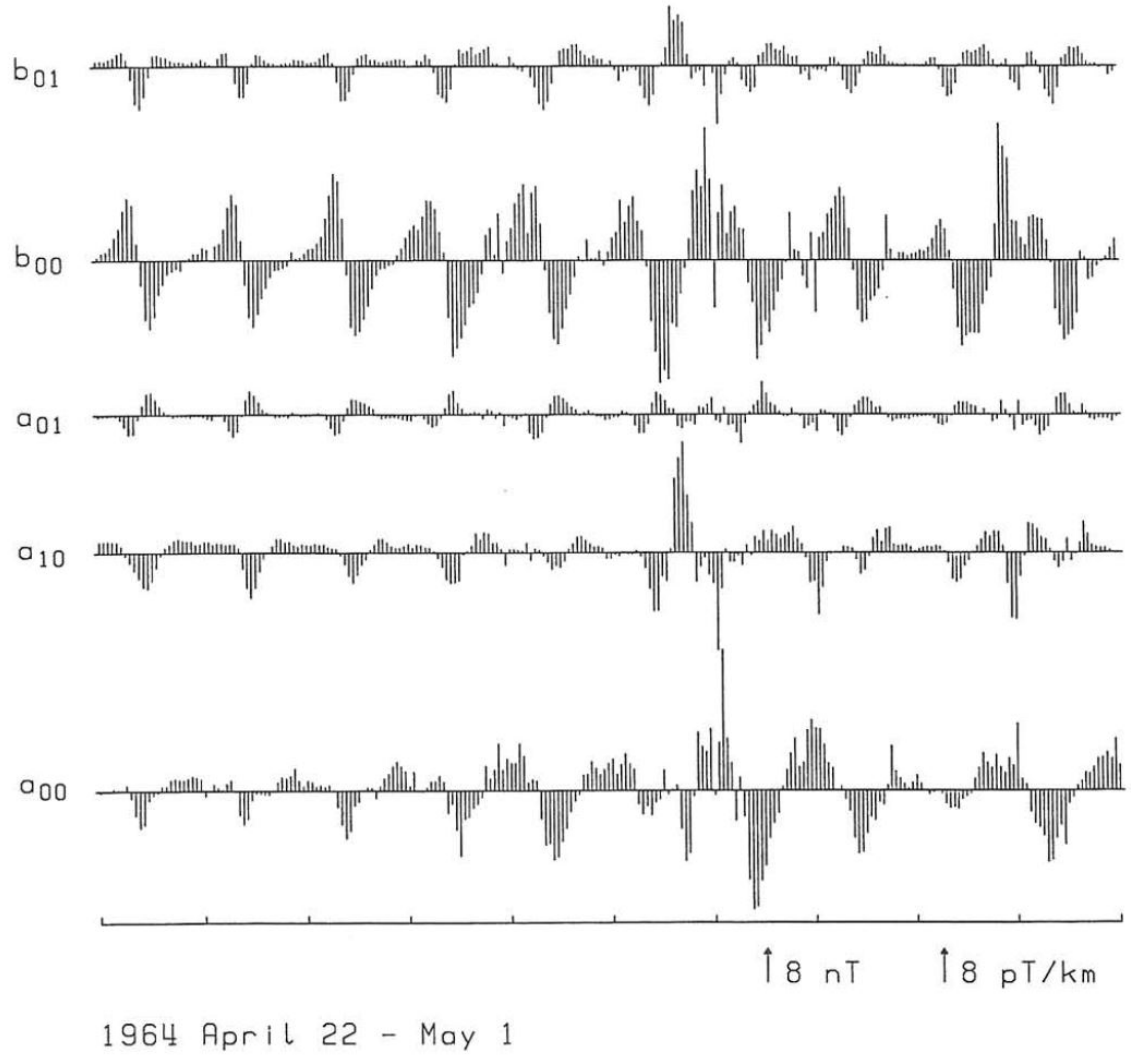

Figure 5: Time series of polynomial coefficients for the same ten days as in Fig. 1, derived by fitting second degree 2-dimensional polynomials to the horizontal components at 30 European observatories, hour-by-hour. Cf. eqs (57) for notations. Coefficients a_{00} and b_{00} for absolute terms are in Nanotesla, coefficients a_{10}, $a_{01} = b_{10}$ and b_{01} for linear terms in Picotesla per kilometre. See Fig. 6 for coefficients of quadratic terms. - With the zero reference point P_r in Southern Germany, time series a_{00} and b_{00} are expected to reproduce the variations of B_x and B_y at the observatory FUR as it is indeed the case (cf. Fig. 1). The most prominent linear coefficient is a_{10} for the change of B_x in north-south direction and its quasi-periodic variations reflect the latitude dependence of daily variations during quiet times. Similar variations of a_{01} and b_{01} account for the dependence of daily variations on local time and thereby on longitude. Strongly enhanced oscillations of a_{10} and b_{01} on disturbed days reflect an increased spatial complexity of the inducing source field during magnetic storms.

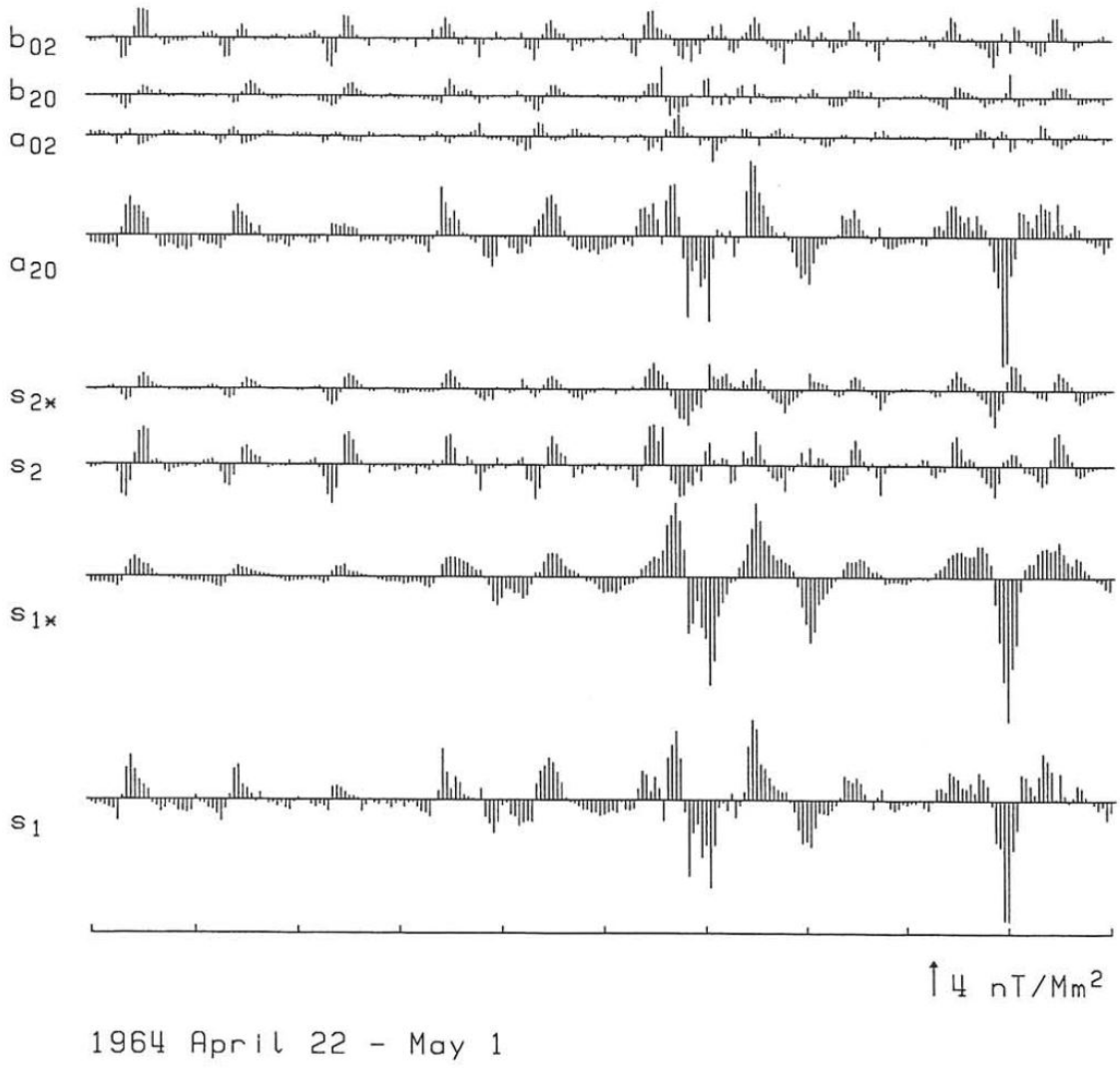

Figure 6: Time series of polynomial coefficients as shown in Fig. 5. Top: Coefficients for the quadratic terms with identities $a_{02} = b_{11}$ and $b_{20} = a_{11}$, in Nanotesla per 1000 kilometres squared. Bottom: Sums $s_1 = a_{20} + a_{02}$ and $s_2 = b_{20} + b_{02}$ of coefficients for quadratic terms above their predictions $s_{1^*} = 0.5 \cdot c_{10}/C_{mod}$ and $s_{2^*} = 0.5 \cdot c_{01}/C_{mod}$ according to eqs (60) and (61). They involve coefficients c_{10} and c_{01} for linear polynomials fitted to B_z and a model response C_{mod}, here for a perfect conductor at $600\,km$ depth. - The most conspicuous coefficient is a_{20} for the non-linear change of B_z in north-south direct ion and we find a reasonably good agreement of the sums of quadratic coefficients with their predictions. Cf. text for further comments.

of the two time series, even to small details, which means first of all that we can expect reliable C-response estimates from gradient sounding. Secondly, these responses should not vary greatly across Europe from Italy to Sweden, at least not for daily variations. Thirdly, it confirms that the vertical component reflects essentially induction in a layered Earth by a spatially non-uniform source field rather than local induction anomalies.

But it is evident from Fig. 7 also that during the hours of maximum magnetic activity second degree polynomials cannot cope with the steep increase of substorm-related variations of the vertical component beyond the observatory WNG in Northern Germany. We recall that during these times coefficients a_{10} and a_{20} have the same sign and thus produce a linear increase of G with latitude, which is more or less in accordance with the observed increase of the vertical component up to Northern Germany. But starting with the observatory RSV in Denmark, third degree polynomials would have been needed, yielding a second degree polynomial for G. As far as activity-related variations are concerned, it remains inconclusive therefore, whether the surprisingly large amplitudes of B_z at the Swedish observatory LOV express a greater penetration depth into a comparatively more resistive Earth's mantle under Scandinavia, or whether they are due to the cited deficiencies to determine G properly. On the other hand, the vertical component of daily variations seems to be well reproduced by the spatial gradients at *all* sites, including the northern observatories, which supports the second interpretation.

5 TRANSFER FUNCTIONS

5.1 Multivariate regressions for gradient sounding in combination with geomagnetic depth sounding

In the context of electromagnetic sounding research usually not more than two transfer functions are determined for one single field component, as for instance in MTS. One of the exemptions is Larsen's "signal-noise separation method" to process MTS data with correlated magnetic noise at two sites (Larsen et al., 1996, eq. 3) . The method requires the determination of four transfer functions for each geo-electric component, two for the magnetic far-field of global dimensions and two for the magnetic near-field of a local source, which is responsible for the noise. The here attempted combination of gradient sounding with GDS involves three or even five transfer functions. It is the main purpose of the following subsection to investigate how the arising multivariate linear problem should be formulated for a well resolved and stable solution.

Because no need exists to identify explicitly frequency and location, to which the analysis refers, we simplify notations and denote with Z_n the complex Fourier amplitude of the vertical component (B_z^*) for the n-th event at a given frequency and location. It will be understood as output variable of the multivariate regression

$$Z_n = \sum_{k=1}^{K} C_k X_{nk} + \delta Z_n \,, \tag{64}$$

with $K \leq 5$ and $n = 1,2,\ldots,N$, in which $C_1, C_2, \ldots, C_K$ are the transfer functions to be found. The input variables $X_{n1}, X_{n2}, \ldots, X_{nK}$ represent an assortment of Fourier amplitudes for horizontal magnetic field components and their spatial derivatives, as they appear for instance on the right-hand-side of eq. (31). They are derived from polynomials and are therefore available for all events regardless of any data gaps for the horizontal components, provided the number of sites without

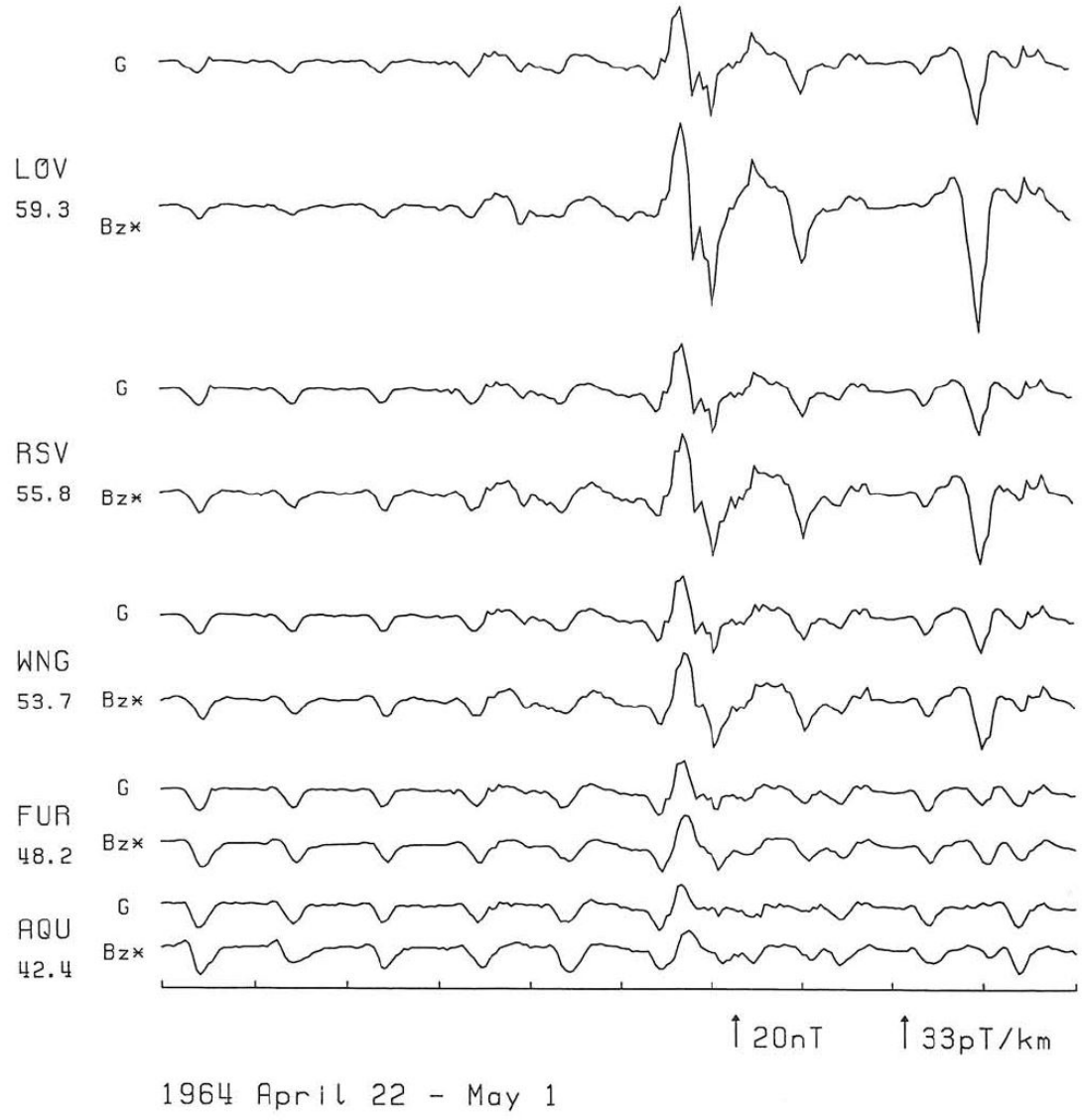

Figure 7: Time series of the vertical component B_z^* and of the horizontal spatial gradient G according to eq. (74), shown for the same ten-day record samples across Europe as in Fig. 1. For the chosen scaling factors the two time series would look alike, if the C-response were the real-valued response of a perfect conductor at $600\,km$ depth $(20\,nT = 600 \cdot 33\,pT)$. - Variations of B_z^* are predicted quite well from G at all five sites, down to small details. On disturbed days, however, activity-related strong excursions in B_z^* are reproduced by G only up to Northern Germany. Further to the north their rapid increase cannot be matched by very similar but less rapidly rising oscillations in G.

data is not too large. The analysis is restricted then to those N events for which B_z is available at the considered location.

The scaling of the input variables and their transfer function should ensure that all input variables contribute more or less equally to the output variable. Therefore C-responses will be measured in units of $1000\,km$, yielding with spatial gradients in the order of Picotesla per kilometre contributions in the order of Nanotesla. The same applies to contributions connected to the dimensionless GDS transfer functions, which are in the order of 0.1, while amplitudes of the horizontal components are in the order of $10\,nT$. The exclusive assignment of residuals to Z_n can be justified as follows: All data and the Fourier amplitudes derived from them naturally have errors. But the performed least squares fit of polynomials to observations at *many* sites should smooth out the influence of individual errors upon the input variables, while Z_n represents a fully error-bearing observations at a *single* site.

For brevity we continue in vector notations. Vectors $\underline{Z} = (Z_n)^T$ and $\delta\underline{Z} = (\delta Z_n)^T$ stand for the N output variables and their residuals, the model vector $\underline{c} = (C_k)^T$ for the K unknown transfer functions, and the $(N \times K)$ matrix $\underline{\underline{X}} = (X_{nk})$ for the column-wise arranged input variables. In these notations eq. (64) reads $\underline{Z} = \underline{\underline{X}}c + \delta\underline{Z}$ and the normal equation for a least squares solution is $\underline{\underline{X}}^H\underline{\underline{X}}\underline{c} = \underline{\underline{X}}^H Z$, with $\underline{\underline{X}}^H$ as Hermitian transpose of $\underline{\underline{X}}$. The $(K \times K)$ matrix $\underline{\underline{S}} = \underline{\underline{X}}^H\underline{\underline{X}}$. contains as *spectral matrix* the power and cross-spectra of the input variables in all possible combinations. Its diagonal element S_{kk} is the power spectrum of X_k and its off-diagonal elements S_{kl} the cross-spectrum of X_l with X_k. Similarly the components of the *data vector* $\underline{d} = \underline{\underline{X}}^H\underline{Z}$ are the cross-spectra S_{zk} of the output variable with all K input variables. In the case of the S_r-analysis of single days, these (global) spectra are the weighted sums of Fourier products over the N events. In the S_{cont}-analysis, by assigning the same transfer function to all Fourier amplitudes within the same frequency band, we proceed from band-averaged Fourier products, which are then summed over all events (cf. Section 3).

The thus abbreviated normal equation $\underline{\underline{S}}\underline{c} = \underline{d}$ has the solution $\underline{c} = \underline{\underline{S}}^{-1}\underline{d}$ for a minimum squared norm of the residual vector. The concern is that the spectral matrix $\underline{\underline{S}}$ may become ill-conditioned for inversion with an increasing number K of transfer functions. The ultimate cause are interdependencies among the input variables in the sense that products of power spectra $S_{kk}S_{ll}$ approach the squared absolute value of the cross-spectrum $\mid S_{kl} \mid^2$, which means that the coherence coh^2_{kl} between X_k and X_l, approaches unity. In the bivariate analysis of MTS and only one coherence between input variables, the remote possibility that the spectral matrix becomes ill-conditioned usually is ignored. In the trivariate version of MVS already three coherences are involved, but eigen-value decompositions of the spectral matrix have shown that it is as a rule still well-conditioned for inversion. But when in the most general form of MVS altogether five transfer functions have to be found, the number of coherences increases to ten, and then even moderate interdependencies of, say, uniformly $coh^2_{kl} = 0.5$ tend to render a not regularized inversion of $\underline{\underline{S}}$ to be problematic. In order to gain more insight an exemplary eigen-value analysis is conducted now with the (5×5) Hermitian matrix $\underline{\underline{S}}$ for gradient sounding in combination with GDS, involving Sq-variations on 124 quiet Q^*-days during 1964-65. Test site is the observatory Fürstenfeldbruck (FUR) in Southern Germany. But since the input variables change only smoothly within Europe, the following results should be representative for the entire network of observatories.

They are twofold: Firstly, the condition number λ_l/λ_k indicates whether regularisation is needed for inverting $\underline{\underline{S}}$, with (positive) eigen-values λ_j numbered according to their size and $j = 1, 2, \ldots, K$.

Secondly, the exigent-vectors $\underline{u}_j = (u_{kj})$ provide information about linear combinations of transfer functions, which can be determined with an accuracy proportional to λ_j^{-1}, when errors of the data vector components are taken into account. Noting that $\hat{c}_j = \underline{u}_j^T \underline{c}$ and $\hat{d}_j = \underline{u}_j^T \underline{d}$ are projections of model and data vectors on principal axes and that the solution $\hat{c}_j = \hat{d}_j/\lambda_j$ applies also to the transfer of independent data errors into model errors, projections $\hat{c}_1$ and $\hat{c}_K$ for the largest and smallest eigen-values can be expected to have the smallest and greatest errors, respectively. Hence, the visual display of the components of eigen-vectors, as in Fig. 8, suggests, which combination of transfer functions may have chances to be determined well and for which combination estimates will be problematic. The lengths of the vertical bars in Fig. 8 depict the size of the elements. But neither their size matters as such, because all eigen-vectors have been normalised to $\| \underline{u}_j \|^2 = 1$, nor matters the distinction between real and imaginary parts. The only reason to show them separately is to preserve their signs.

Figure 8 begins in the top row with eigen-vectors $\underline{u}_1$ for five input variables according to eq. (31). They indicate that the combination of $C_1 = C_{xy}$, $C_2 = -C_{yx}$, and $C_5 = z_D$ promises the best resolution. But observing that the eigen-vector components u_{11} and u_{21} have comparable sizes and agree in their signs for real and imaginary parts, the sum of the first two transfer functions, when connected to the sum of the first two input variables, promises to have an even better resolution. This leads to a rearrangement of terms according to eq. (33). The resulting eigen-vectors $\underline{u}_1$ are shown in the second row. They verify that the Berdichevsky average $C_1 = (C_{xy} - C_{yx})/2$ and in general both GDS transfer functions can be estimated with greater accuracy than transfer functions $C_2 = C_{xy} + C_{yx}$ and $C_3 = C_{xx} - C_{yy}$ for anisotropy and 3D effects, respectively.

Eigen-vectors $\underline{u}_2$ to $\underline{u}_5$ in the next four rows demonstrate that all five eigen-vectors are needed to construct a solution from $C_k = \sum_{j=1}^{5} u_{kj}\hat{c}_j = \sum_{j=1}^{5} u_{kj}\hat{d}_j/\lambda_j$ which includes transfer functions C_2 and C_3 because the eigen-vector components u_{2j} and u_{3j} become prominent only for $j = 4$ and 5. But the full inclusion of all eigen-vectors may come in conflict with the need for regularisation in the case of large condition numbers. When then for a chosen α^2 as regularisation parameter, $1/\lambda_j$ is replaced by γ_j/λ_j with weights $\gamma_j = \lambda_j^2 / \left(\alpha^2 + \lambda_j^2\right)$, the choice $\alpha = \lambda_4$, for example, reduces the contribution from $u_{k4}\hat{d}_4$ to C_k by one half, and the contribution from $u_{k5}\hat{d}_5$ to $\gamma_5 \approx (\lambda_5/\lambda_4)^2$ when $\lambda_5 \ll \lambda_4$.

In the last rows of Fig. 8 we return to the eigen-vectors for the largest eigen-value, now shown for all six harmonics and with condition numbers at the right margin. We note that the conclusion about the best resolvable combination of transfer functions remains valid for all frequencies. Secondly, large condition numbers for the first four harmonics indicate the need to stabilise the inversion of their spectral matrices by adding a regularisation parameter α^2 to their diagonals . The choice $\alpha^2 = 0.1$ for $\lambda_4 = 0.941$ and $\lambda_5 = 0.274$ implies with weights $\gamma_4 = 0.898$ and $\gamma_5 = 0.429$ that all five transfer functions can be included into a sufficiently stabilised solution. But because it is not possible to specify data errors, it cannot be said whether the resulting residuals of the 5-variate regression are on the same level with data errors, as it is intended by regularisation. The concurrent loss in fit of the predicted to the observed output variable is quite moderate as it is evident from an only minor decrease of the multiple coherence (cf. Table 3, last column). Noteworthy is the continuous decrease of condition numbers with increasing frequency, removing the necessity of regularisation for the last two harmonics. This unexpected result means that interdependencies among the five input variables gradually disappear, possibly because at high frequencies they come down to the level of independent random variables.

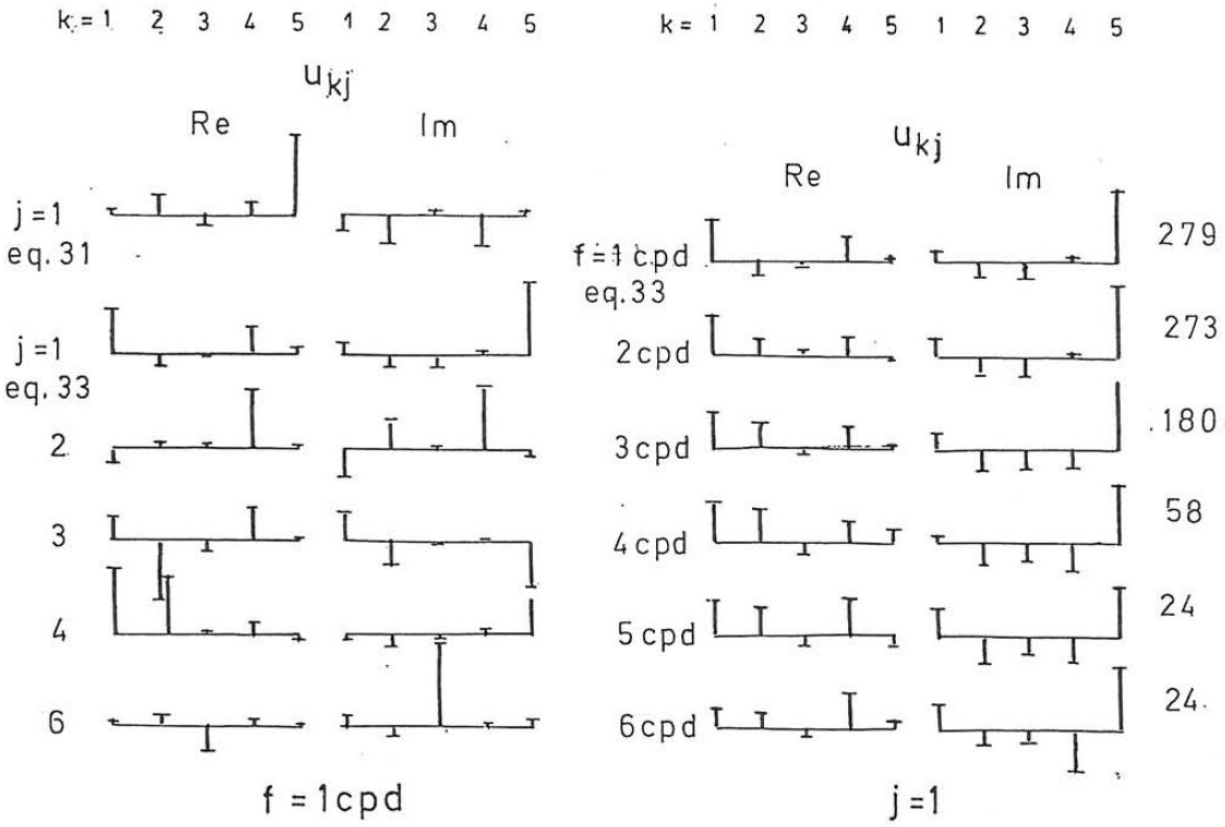

Figure 8: Eigen-value analysis of the spectral matrix $\underline{\underline{S}}$ in a multivariate regression to derive tensor C-responses together with GDS transfer functions. Subscripts j for the eigen-values λ_j and subscripts k for the transfer functions to be determined, with $j,k = 1,2,\ldots,K$ and $K = 5$. Frequency f in cpd. Vertical bars visualize the components u_{kj} of eigen-vectors $\underline{u}_j = (u_{kj})$ for the j-th eigen-value, normalised to $\| u_j \| = 1$ and displayed separately for real and imaginary parts. Test site is the observatory FUR in Southern Germany, and the spectra are for the harmonics of daily variations on 124 $Q*$-days in 1964-65. - Top row left: Eigen-vector for the largest eigen-value λ_1, in a multivariate regression according to eq. (31). Second to sixth row left: Eigen-vectors for all five eigen-values in a multivariate regression according to eq. (33). All displays are for the first harmonic. First to sixth row right: Eigen-vectors $\underline{u}_1$ in a multivariate regression according to eq. (33) for all six harmonics, with condition numbers on the very right. Cf. text for further comments.

5.2 Error bounds of transfer function estimates

Trustworthy estimates of experimental errors are essential for the purpose of this study to test the uniformity of C-responses within Europe. Otherwise it would not be possible to decide, whether scattering response estimates are significant or whether they merely reflect estimation uncertainties. There always exists some fundamental ambiguity about the appropriateness of the underlying theoretical concept, which requires for instance linearity of the basic relations, a point which will be considered in Appendix A, or we presume a stratified Earth for gradient sounding at places, where it should be done in combination with GDS. The possibility of *systematic* errors has to be pointed out, but is beyond control. The variometer could have temperature effects or their scale values could be slightly wrong. If in particular the Z-variometer has a persistent calibration error of a few percent, then all MVS transfer functions have the same error at the respective site.

We turn then to *statistical* errors and begin with bias errors due to noise in the input variables. It seems that in the case of multivariate analyses only jack-knife estimates can handle them (s. below). We continue therefore with the already stated assumptions that no bias exists and derive estimation errors solely from the residuals δZ_n in eq. (64). For mutual control two kinds of errors are considered: distribution-dependent *D-errors* and jack-knife *J-errors*. Calculations for the first kind of errors proceed from two basic assumptions about the statistical distributions of *"true" residuals* $\dot{\delta Z}_n = Z_n - \sum_k \Gamma_k X_{nk}$ and of *deviations* $\delta C_k = C_k - \Gamma_k$, with Γ_k as expectation value of transfer function C_k. The assumptions are that $\dot{\delta Z}_n$ and δC_k in real and imaginary parts are normally distributed independent random variables, with the same variance σ^2 for all events and transfer functions. This leads to χ^2-distributed residual spectra $\dot{\delta S} := \sum_n \mid \dot{\delta Z}_n \mid^2$ and $\delta S := \sum_n \mid \delta Z_n \mid^2$, and also to χ^2-distributed squared modules of δC_k. Sine least squares solutions of multivariate regressions imply $\sum_n \delta Z_n X^*_{nk} = 0$, the spectrum of the associated residuals can be obtained with the aid of eq . (64) from

$$\delta S = \sum_n \delta Z_n (Z^*_n - \sum_k C^*_n X^*_{nk}) = S_{zz} - \sum_k C_k S^*_{zk}, \tag{65}$$

with $coh^2 := 1 - \delta S / S_{zz} = S^{-1}_{zz} \cdot \sum_k C_k S^*_{zk}$ as squared multiple coherence. Considering then the k-th transfer function, the difference between the two residual spectra can be expressed in terms of the deviation δC_k as

$$\Delta S := \dot{\delta S} - \delta S = \mid \delta C_k \mid^2 S_{kk}(1-\rho_k) \tag{66}$$

with $0 \le \rho_k \le 1$ (cf. Appendix ; eq. D2). In univariate relations ρ_k is zero. In multivariate relations it accounts for interdependencies among the input variables.

The number of degrees of freedom to be assigned to the χ^2-distributed variables are $2N$ for $\dot{\delta S}$, obviously $2K$ for $\mid \delta C_k \mid^2$ and thereby also for ΔS, leaving $(2N - 2K)$ for δS according to the partition theorem of χ^2. In the case of band-averaged Fourier products the equivalent number Tb of such products in each band has to be added as a factor to N, with b as equivalent band-width of the spectral filter, here $0.93\,cpd$, yielding $Tb = 9.3$. The derivation of D-errors proceeds from the F-distributed variance ratio $u = (\Delta S/\nu_2)/(\delta S/\nu_1)$ in the usual manner, with $\nu_1 = 2N - 2K$ and $\nu_2 = 2K$. For a chosen error probability β an upper limit $g(\nu_1, \nu_2; \beta)$ can be specified for u as a random variable, which in turn establishes in conjunction with eqs (65) and (66)

$$\Delta C^2_k = \frac{\nu_2}{\nu_1} \frac{S_{zz}(1-coh^2)}{S_{kk}(1-\rho_k)} g(\nu_1, \nu_2; \beta) \tag{67}$$

as an upper bound for $\mid \delta C_k \mid^2$ and thereby defines the D-error ΔC_k for the k-th transfer function. When global spectra are derived by a *weighted* summation of event spectra, N in the formula for v_1 has to be replaced by the sum of weights Q_{nm} over all events.

In univariate relations with $K = 1$ and $v_2 = 2$ the probability density function of the F-distribution can be integrated in closed form, which leads to

$$\Delta C_1^2 = \frac{\delta S}{S_{11}} \left[(1/\beta)^{1/m} - 1 \right] \tag{68}$$

with $m = v_1/2$, $\delta S = S_{zz} - \mid S_{z1} \mid^2 / S_{11}$. The formulas for deriving D-errors in trivariate relations can be found in Appendix D, and no attempt is made to calculate D-errors in multivariate relations beyond $K = 3$. All further error estimations are carried out for $\beta = 0.32$, which corresponds to an error probability of 32 percent that the realisation of a normally distributed random variable lies within one standard deviation from the mean.

Before continuing it has to be realised that for multivariate relations the derivation of D-errors requires further assumptions in addition to those already stated. They concern the phases $\arg\{\delta C_k\}$ of deviations and their co-variances, i.e. the expectation values of products $\delta C_k \cdot \delta C_l$ for $k \neq l$. When the assumptions about co-variances are circumvented, the D-errors become inflated. The inflation is moderate for $K = 2$, but appears to be twofold for trivariate regressions (cf. Appendix D and Table 3).

It has been noted repeatedly by others that D-errors tend to be overly optimistic. One cause for the underestimation of errors seems to be that contrary to the stated assumption linear dependencies connect real and imaginary parts of the residuals and, in the case of band-averages, also between real and imaginary parts of *all* residuals in the same frequency band. Such interdependencies may have been indicated already in Fig. 3 by a certain non-randomness of the spectral continuum between the spectral peaks of daily variations. As a consequence the degrees of freedom v_1 are overestimated, leading to errors which are too small, as it is readily inferred from eq. (68).

Junge (1992)and Ritter et al. (1998, Appendix A1) suggest to derive the number of degrees of freedom experimentally from the mean and variance of the event spectra $\mid \delta Z_n \mid^2$ of residuals, in the following double subscripted as

$$\delta \hat{S}_{nm} = \mid Z_n - \sum_k C_k X_{nk} \mid^2 \tag{69}$$

in order to include in subscript m a reference to the relevant frequency. In the continuum analysis $\delta \hat{S}_{nm}$ is to be understood as band-average. If then M denotes an estimate of the expectation value μ of $\delta \hat{S}_{nm}$ and s^2 an estimate of its variance σ^2, and noting that $2\mu^2/\sigma^2$ represents the number of degrees of freedom for χ^2, then $2M^2/s^2$ defines an *effective number of degrees of freedom* v_{eff} of $\delta \hat{S}_{nm}$. Thus for $N \gg 1$ the number of degrees of freedom assigned to the event spectra of residuals at frequency ω_m are

$$v_{eff}(m) = \frac{2 \left(\sum_n \delta \hat{S}_{nm} \right)^2}{N \cdot \sum_n \left[\delta \hat{S}_{nm} \right]^2 - \left(\sum_n \delta \hat{S}_{nm} \right)^2}, \tag{70}$$

which corresponds to equation A10 in the cited reference. Henceforth, the limit $g(v_1, v_2; \beta)$ in eq. (67) will be calculated with the frequency-dependent value

$$v_1(m) = \sum_n Q_{nm} \cdot min \left\{ v, v_{eff}(m) \right\} - 2K. \tag{71}$$

The thereby established upper limits for v_{eff} are $v = 2$ for the S_r-analysis and $2Tb = 18.6$ for the S_{cont}-analysis. Theses limits are reached rarely, however, and as a rule v_{eff} tends to scatter around 1.2 and 12, respectively.

The *jack-knife* method is likewise an experimental method, which Chave & Thomson (1989) introduced into MTS. It can be applied to multivariate relations involving any number of input variables, and it does not require assumptions about statistical distributions of residuals $\delta\dot{Z}_n$ or deviations δC_k. For the forthcoming analyses with five input variables, it will be the only method to estimate errors. By omitting in the least squares analysis one event after the other, N experiments are performed with $(N-1)$ events. If C_{ki} is the least squares estimate in the i-th experiment, without the i-th event, and C_k the same estimate from all N events, then the mean of the N differences $D_{ki} = C_k - C_{ki}$, multiplied with $(N-1)$ and added to C_k, defines the jack-knife estimate M_k, and the sample variance of those differences leads to an estimate s_k^2 of the variance σ_k^2 of the real and imaginary parts of δC_k:

$$M_k = C_k - (N-1)/N \sum_{i=1}^{N} D_{ki} \,, s_k^2 = \frac{N-1}{N} \sum_{i=1}^{N} \mid D_{ki} - \frac{1}{N} \sum_{j=1}^{N} D_{kj} \mid^2 \,, \tag{72}$$

in correspondence to eqs (21) and (22) in the cited reference.

The estimator M_k has the advantage over the least squares estimate C_k that it tends to be bias-free. The (biased) estimator s_k^2 has the advantage over the squared D-error for C_k that it presents the variance of either M_k or C_k in their real and imaginary parts, with co -variances taken fully into account as expectation values of products $\delta C_k \cdot \delta C_l$ for $k \neq l$. It would have been possible even to derive the complete $2K \times 2K$ co-variance matrix for the real and imaginary parts of δC_k, with the implication that both parts have the same variance. At this point we recall the complications which in the derivation of D-errors arise from the unknown phases of the deviations δC_k and from their likewise unknown co-variances.

Chave & Thomson (1989) were concerned that output and input variables may have greatly different variances. In order to offset this imbalance the differences D_{ki} are down-weighted with increasing diagonal elements w_i of the hat-matrix, and D_{ki} in eq. (72) is replaced by $D_{ki}^w = N(1-w_i)/(N-1) \cdot D_{ki}$. This matrix connects the prediction $\underline{\underline{X}}\underline{c}$ for vector $\underline{Z}$ to the vector $\underline{Z}$ itself, representing the observed output variables. With $\underline{c} = \underline{\underline{S}}^{-1}\underline{\underline{X}}^H\underline{Z}$ the weights w_i are the elements of the thus defined *hat-matrix* $\underline{\underline{X}}\underline{\underline{S}}^{-1}\underline{\underline{X}}^H$ in the i-th row and column . If c is a robust estimate, $\underline{\underline{X}}^H$ has to be multiplied with the diagonal matrix of weights Q_{nm}. In this study results from weighted and non-weighted differences turn out to be almost identical, and in all further applications weighting is omitted. Furthermore, with the mean of these differences near zero throughout, M_k and C_k are almost identical, indicating the absence of bias.

For a sufficiently large number of events, σ_k can be approximated by its estimate s_k from above, representing the standard deviation of the real and imaginary parts of δC_k. In this way s_k defines also the jack-knife error ΔC_k^J as upper bound for $\mid \delta C_k \mid$ for an error-probability of 32 percent. Since our D-errors refer to the same error probability, both kinds of errors can be tested against each other. Entries into the forthcoming Table 3 demonstrate that D- and J-errors are of similar sizes for univariate analyses, with a tendency of J-errors to be slightly smaller, but in the trivariate analysis D-errors exceed J-errors by a factor of two. The reason seems to be the already mentioned inflation of D-errors due to the neglect of co-variances.

The best method to see whether error limits are realistic or not, is a repetition of the regressions with different data, obtained preferably also with different instruments. As a substitute the 24

months of the IQSY 1964-65 are subdivided according to Lloyd season into *D-months* (November to February), *E-months* (March-April, September-October), and *J-months* (May to August). All days in the respective season are used for an analysis of daily variations towards C-responses, omitting only those greatly disturbed days for which the whole-day magnetic activity index $C9$ exceeds the value of five for moderate activity. The subdivision leads to six sets of C-responses, each derived with the data of about 115 days. Figure 9 displays their real and imaginary parts for the first harmonic in complex planes. It should be noted that the vertical axis is limited for clarity to the depth range from 500 to 800 km, which is relevant for the real parts at 1 cpd. Test site is the observatory Fürstenfeldbruck (FUR) in Southern Germany. On the left are the resulting scalar C-responses from an univariate regression, in the centre and on the right the Berdichevsky averages C_1 of tensor C-responses in multivariate regressions, omitting in the trivariate case the last two terms of eq. (33) for GDS. Error bars represent in all three displays jack-knife errors for consistency.

We note in Fig. 9 an overall adequate determination of errors, but a closer inspection reveals also various shortcomings. Five of the six seasonal univariate estimates agree well within error limits, testifying for the presumed randomness of errors. But a strongly divergent estimate for the winter season 1965 indicates that unexpected deviations may occur which cannot be accounted for with statistical errors. Scatter and errors grow naturally when in multivariate regressions the number of transfer functions increases, but the majority of estimates remains compatible with each other due to enlarged error limits. The exemptions are the summer seasons of both years. Thus we can expect to obtain the best and most consistent results by concentrating the analysis on all not greatly disturbed days during equinoxes. It also appears that in the trivariate realistic account of uncertainties. These conclusions can be extended to the higher harmonics and apply also to other sites. Noteworthy is in any case that the univariate and the two multivariate determinations agree quite well with each other.

5.3 Spectral weights for robust transfer function estimations

So far it has been assumed that the residuals δZ_n of the linear process are normally distributed random variables in their real and imaginary parts, with zero mean and a constant variance σ^2. This is the underlying assumption not only for the derivation of D-errors, but also for the least squares analysis itself. Only then does it lead to estimates C_k with minimum variance against their expectation values Γ_k. A variable variance σ_n^2 among the events is not critical and can be accounted for by weighting the variables with $1/\sigma^n$. But as to be shown later there is no evidence that such weighting is necessary. This conclusion is not in conflict with observations by Egbert & Booker (1986) and others, when analysing mid-latitudes data toward GDS transfer functions for fast substorm variations and pulsations. They found that during times of intensifying magnetic activity the spectrum of residuals tends to increase in proportion to the power spectra of the horizontal components. But since during disturbed times the complexity of the source field structure increases also and because horizontal spatial gradients are not taken into account in conventional GDS, the spatial non-uniformity of the source field could have added to the residuals in proportion to increasing complexity.

The validity of the stated assumptions is tested with the aid of quantile-quantile (Q-Q) plots. Since the algorithm for robust processing will be based on the absolute values $\mid \delta Z_n \mid$ of the residuals, which should be *Rayleigh*-distributed, the following plots visualize their compatibility with a truly Rayleigh-distributed random variable $\widetilde{R}$. Its distribution function is $F(\widetilde{R}) = 1 - exp(-iR^2/2\sigma^2)$, where σ^2 denotes the common variance of two normally distributed random variables A and B,

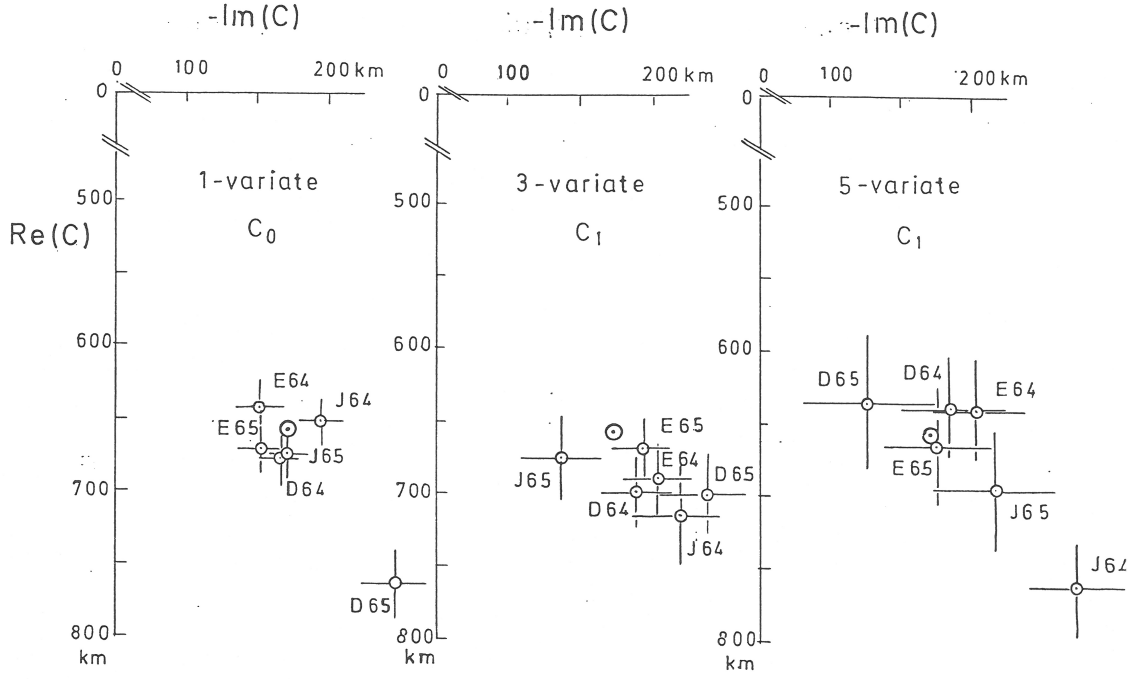

Figure 9: Seasonal C-response estimates from univariate and multivariate regressions, shown in complex planes for the first harmonics of daily variations. Test site is the observatory FUR in Southern Germany and all days of the years 1964-65 are included within the respective Lloyd-season[1)] except highly disturbed days with $C9 > 5$. Error bars refer to jack-knife errors in all three displays. Left: Scalar C-responses obtained with the univariate gradient method. Centre: Scalar C-responses obtained in combination with two GDS transfer functions. Right: Berdichevsky averages of tensor C-responses obtained in combination with two GDS transfer functions. Large symbols without error bars are theoretical responses for a global model which accounts for the globally determined potential ratio of external to internal parts, for comparison. - Widening clusters of estimates with increasing numbers of transfer functions correspond to a concurrent increase of error uncertainties, which verifies that calculated error bounds are realistic. All seasonal estimates agree within error limits, with one notable exception in each display. They are consistent also with the global results in all three regressions.

[1)] D-months: Nov.- Febr. ; E-months: March-April and Sept.-Oct.; J-months: May-August.

standing for the real and imaginary parts of δZ_n, i.e. $\widetilde{R} = +\sqrt{A^2+B^2}$. The absolute values of the residuals are ordered now according to their size, and the resulting order statistics are renamed $R^{(h)}$ with $R^{(1)} \leq R^{(2)} \leq \ldots \leq R^{(N)}$. Noting that $\widetilde{R}$ has the median $\widetilde{R}_{med} = \sqrt{2\ln 2}\sigma$, the median of the order statistics provides a convenient estimator for the standard deviation σ. For an uneven number of events and $M = (N+1)/2$ an integer, the estimator is $s = R^{(M)}/\sqrt{2\ln 2}$. Otherwise the mean of $R^{(N/2)}$ and $R^{(N/2+1)}$ is to be taken. Plotting then the normalized order statistics $x_h = R^{(h)}/s$ against their predictions $y_h = \widetilde{R}^{(h)}/\sigma$ for $F(\widetilde{R}^{(h)}) = h/(N+1)$, yielding $y_n = \{2\ln[(N+1)/(N+1-h)]\}^{1/2}$, the resulting Q-Q plot would follow a straight line, when $\mid \delta Z_n \mid$ were truly Rayleigh-distributed, while events with $y_n > x_n$ beyond, say, $x = 2$ identifying *outliers*. This line passes through the origin and the median point $h = M$ by definition, with $x_M = y_M = \sqrt{2\ln 2} = 1.18$.

Figure 10 presents Q-Q plots for various selections of events, here single days. They display the order statistics of residual amplitudes for the first harmonic of daily variations, obtained with gradient sounding, and in order not to suppress outliers they refer to non-robust estimates of the scalar C-response. Test site is again FUR, but corresponding Q-Q plots for higher harmonics and also for different sounding sites have led to similar conclusions. The three plots to the left concern the possibility that the deviations between observed and predicted order statistics depend on the season. As in Fig. 9 all quiet and moderately disturbed days with $C9 \leq 5$ are included. We note in the top display that during the winter months residuals start to exceed their prediction already from one standard deviation onward ($x = 1$) , while during summer and equinoxes the agreement lasts until about two standard deviations. Beyond $x = 2.5$, however, residuals surpass predictions widely in all seasons, identifying the remaining roughly eight percent of realizations as genuine statistical outliers. With regard to the estimators of standard deviations, shown in the upper left corner of each plot, we observe the expected seasonal dependence, with an increase from $0.45\,nT$ during the winter to $0.74\,nT$ during the summer. This is much less, however, than the concurrent seasonal change of the daily variations themselves, which increase in their amplitudes by a factor of about three, justifying in this way the stated preposition of a more or less time-constant variance.

The three Q-Q plots on the right investigate the influence which magnetic activity might have. When all 720 days of 1964-65 are included, which have B_z-data at the test site, regardless of the degree of magnetic activity on the specific day, then residuals on a multitude of days deviate increasingly from their prediction beyond two standard deviations , but the omission of the 36 most disturbed days in the Q-Q plot below, which have $C9 \geq 6$, reduces their number effectively. A further restriction to quiet and moderately disturbed days during the eight equinoctial months leaves just about ten realizations as clearly recognizable outliers, which amounts to about five percent of the total of 221 days. All further S_r-analyses will be based on this selection of days. In the S_{cont}-analysis a corresponding examination of residuals of the 72 ten-day sections has shown that their variance may be regarded also as constant throughout the two years of the IQSY, with a tendency however that sections containing magnetic storms have more excessive residuals than sections without them, a point to be taken up again in the next section.

We have tested two alternative methods to derive spectral weights Q_{nm}, real numbers in $[0,1]$ and subscripted in reference to the n-th event and m-th frequency. In the first method they are the ratio of expected to observed numbers of events, whose residual spectra lie within a specified range (Schmucker, 1999b, Appendix A), the second method is Junge's robust algorithm (Junge, 1994; Ritter et al., 1998, Appendix A1). Both methods generate in three iterations the final set of weights for a given frequency. Additional iterations leave the weights more or less unchanged and are not needed. Furthermore, both methods lead to comparable results in the sense that the same events receive weights near zero or near unity. But they differ in the intermediate range. The first method

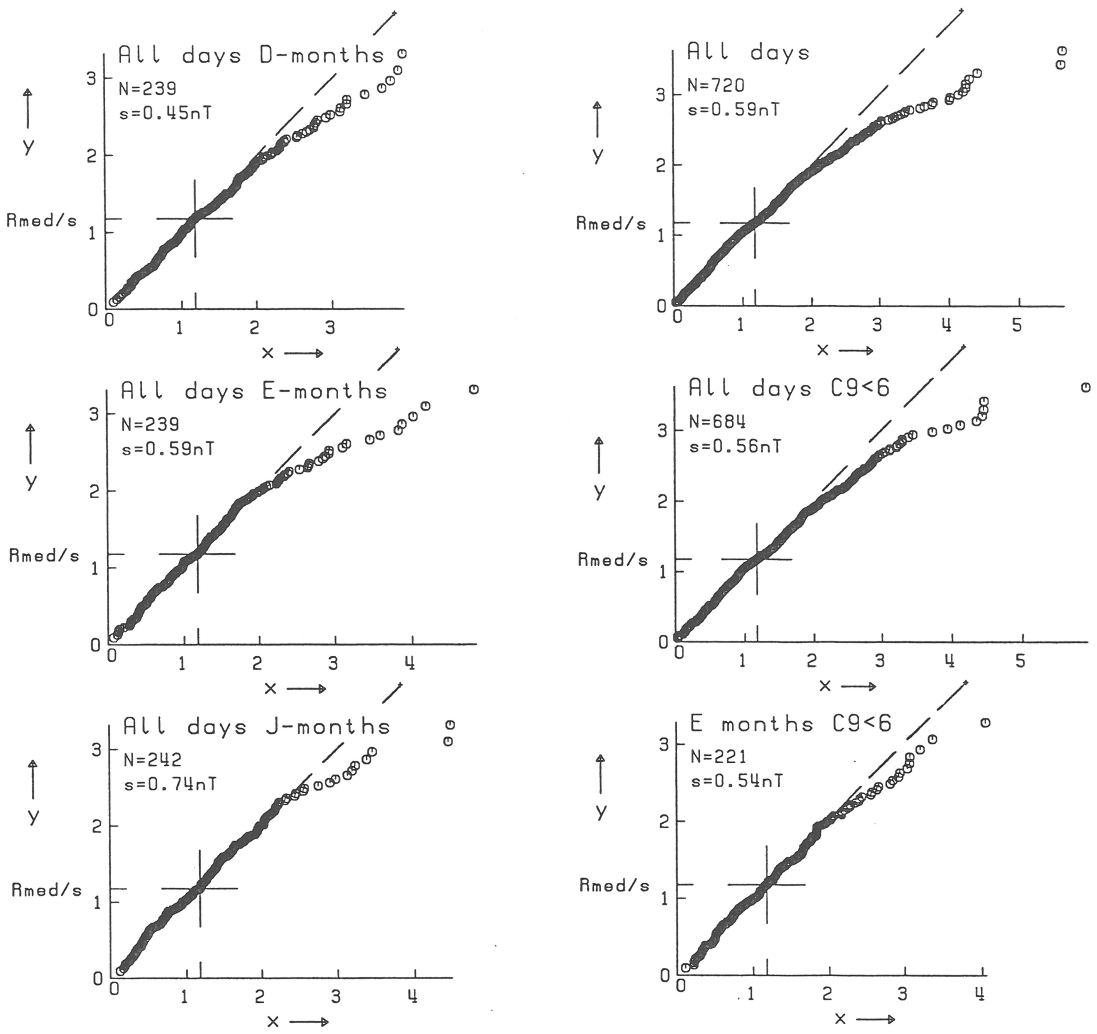

Figure 10: Quantile-quantile (Q-Q) plots to identify outliers in univariate gradient sounding. Test site is the observatory Fürstenfeldbruck (FUR) in Southern Germany. The analysed data are selected single days in 1964-65, and the residuals are for the first harmonics of daily variations. x: Normalised absolute values of the (complex) residuals ordered according to their size; y: The same for Rayleigh-distributed random variables (cf. text). Numbers in the upper left corner of each display are the number N of analysed days and the estimates for the standard deviations of the real and imaginary parts of the residuals. Small circles mark (x,y) on N days . - Left: Q-Q plots for the three Lloyd seasons 1964-65 (cf. legend to Fig. 9), indicating that days during the winter months have the largest number of outliers, with x exceeding the prediction y from $x = 1.0$ onwards. Right: Q-Q plots involving all days 1964-65 (top), all days except highly disturbed days with $C9 > 5$ (centre), the same for equinoctial months only (bottom). Gradual decrease in the (relative) number of outliers from top to bottom, and concurrent shift for the onset of outliers from $x = 1.5$ (top) to $x = 2.0$ (centre) and $x = 2.5$ (bottom).

tends to include or exclude events completely, while Junge's algorithm yields much better balanced weights. Therefore it will be implemented with a few modifications to adapt it to the special needs of this study (cf. Appendix E).

One of the modifications concerns the derivation of residual spectra. In the original version of the algorithm they follow from eq. (69) with transfer functions which are derived event by event with the aid of the respective event spectra. This implies that no weights are involved and that the event spectra of residuals remain unchanged in the course of the iterative process. But this procedure is possible only, when the number of Fourier amplitudes $T\Delta f$ within frequency bands is sufficiently large in comparison to the number K of transfer functions to permit their determination by least squares. In the S_r-analysis of single days and thus $T\Delta f = 1$, residual spectra can be derived, however, only with transfer functions which have been obtained from global spectra, i.e. after a weighted summation of Fourier products, with the consequence that the event spectra of residuals have to be updated in the course of the iterative process. In the S_{cont}-analysis with $T\Delta f = 10$ the number of Fourier products is quite sufficient to derive residuals also with transfer functions obtained individually for the 72 ten-day sections, at least in univariate regressions. Tests have shown that the resulting two sets of weights are very similar. Hence, for consistency weights will be derived in the manner as described for the S_r-analysis.

The following examples illustrate the influence of weighting on the final outcome. We return once more to gradient sounding with daily variations at the observatory FUR, using all 720 days during the IQSY, for which B_z is available. For the first harmonic at $1\,cpd$ the non-robust estimate is $C(\omega_1) = 667 - 195ikm$ (10), with the D-error in parenthesis; the squared coherence is $coh^2 = 0.946$. Robust estimation leads with $C(\omega_1) = 666 - 194ikm$ (7) and $coh^2 = 0.956$ not to a very different result, even though the coherence has increased slightly and the error has been reduced accordingly. Obviously, days are rare with "bad" data for gradient sounding and their influence is not unduly strong. The sum of weights implies with 668.3 that effectively 7.3% of the data have been eliminated by weighting. With increasing frequency the improvements by robust processing become more visible. The results for $6\,cpd$ are $C(\omega_6) = 297 - 183ikm$ (26) with $coh^2 = 0.414$ non-robust and $C(\omega_6) = 305 - 169ikm$ (19) with $coh^2 = 0.468$ robust, while with 670.5 as the sum of weights again 7.0% of the data are not used. These findings are characteristic for all sites and extend also to the continuum analysis. The overall impression is that robust processing may not be essential in this study but it is certainly useful.

We conclude the section with considering the question, why certain events are down-weighted and others not. When daily variations are analysed, the degree of magnetic activity might be decisive for the assignment of weights. Table 2 confirms the correctness of this expectation. It concerns the daily residuals for the just cited non-robust estimate for $1\,cpd$ at FUR by subdividing the analysed 720 single days into nine classes according to their residual spectrum on a semi-logarithmic scale. Entries in the bottom row are the days with class-index $I = 0$ for the smallest residuals, entries in the top row are the days with class-index $I = 8$ for the largest residuals (Schmucker, 1999b, eq. A5).

The first column contains the total number of days in each class. The numbers in parenthesis in the second column are the expected number of days, if the squared normalised residuals were χ^2-distributed with the number of degrees of freedom from eq. (70), using for normalisation the sample variance from the upper right Q-Q plot in Fig. 9. There are, for example, 48 days in class $I = 3$ with residual spectra of moderate magnitude, but there should have been only 16 days in this class. A comparison of the first two columns in Table 2 reflects the general experience that there exist considerable more events with moderate to large residuals than there should be. But still

the number of days decreases continuously with increasing class index until $I = 7$, which clearly identifies the eleven days in the highest class $I = 8$ as outliers.

The days of each class are subdivided further column-wise according to the magnetic activity index $C9$, which is a whole-day semi-logarithmic measure for the daily magnitude of geomagnetic variations after the removal of S_q. The third column starts with the number of days during complete quietness when $C9 = 0$, and the last column contains for $C9 = 7$ the most disturbed days during the IQSY 1964-65. Since these were years of the "Quiet Sun", no day exists with $C9 = 8$ or 9 for extreme activity. In class $I = 3$, for example, 11 days out of 48 are very quiet days with $C9 = 0$. We observe that almost none of the quiet days up to $C9 = 2$ has large residuals beyond class $I = 4$, while the 36 greatly disturbed days with $C9 \geq 6$ are spread more or less evenly over all classes. In the intermediate range of $C9$-indices, the tendency of quiet days persists to have good results, occupying classes up to $I = 4$. The overall conclusion is that an analysis with only very quiet days leads to a distribution of residuals, which corresponds already without weights closely to a χ^2-distribution, when this distribution is adapted to the sample variance for the days wit h $C9 = 0$. With this concentration on quiet days a large number of days with useful information would be lost, however, and therefore all not severely disturbed days should be included.

Figure 11 offers a corresponding view of weights Q_{nm} in the continuum analysis. They are shown as time series for the 72 ten-day sections fitted into the IQSY, extending from January 2 in 1964 to December 22 in 1965. Tick marks along the time axis at the end of every third time-section provide an approximate subdivision into months, while dots identify those six sections, which contain magnetic storms with $C9 = 7$. Plotted are the weights derived with Junge's algorithm after the third iteration. They are shown for all eight frequency bands of the continuum analysis and for soundings at two observatories, FUR in Southern and Wingst (WNG) in Northern Germany $610\,km$ apart.

Not unexpectedly WNG has more down-weighted sections than FUR further away from the auroral zone. But we note long sequences with weights near unity at both sites and for all frequencies, for example from November 1964 to March 1965. During theses months no magnetic storm has occurred, but the same applies also to the months from July to October in 1965 with conspicuously down-weighted sections in most frequency bands. Hence, no clear correlation seems to exist between the assignment of weights and the degree of magnetic activity as long as it is moderate. Sections which receive weights near zero can be connected, however, clearly to the occurrence of storms. But again there are exemptions and also differences between the northern and southern site. The April 1965 storm for example coincides with zero weighting for nearly all frequencies, but only at WNG, while the September 1964 storm seem to have no marked effect on the weights at neither site. In view of this ambivalence any pre-selection of time-sections on the basis of storm-time activity seems to be unfounded, and all time-sections will be included in the S_{cont}-analysis, relying again on robust processing to suppress contributions from sections with presumably storm-related excessive residuals.

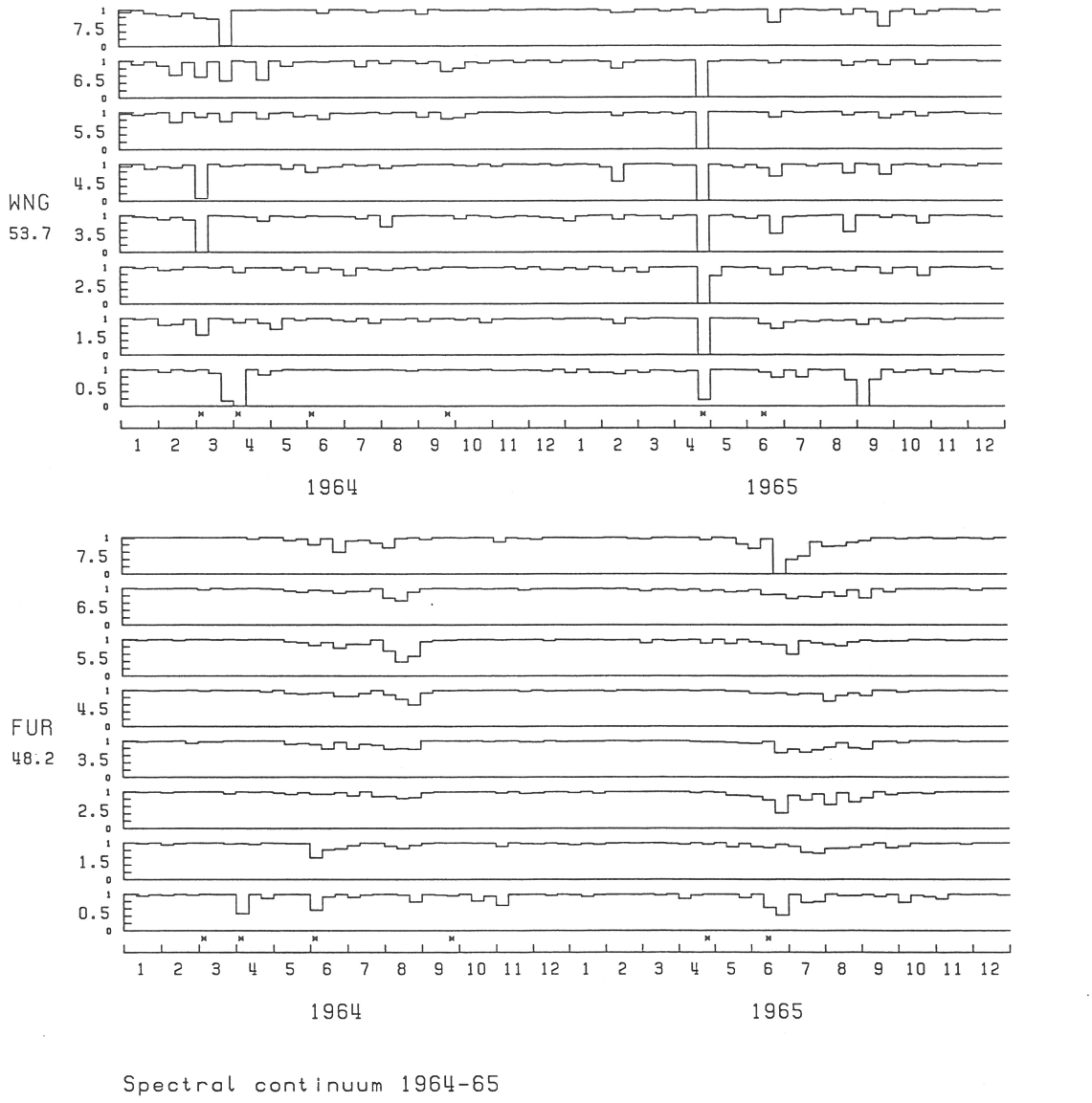

Figure 11: Spectral weights Q_n^m which are used to estimate C-responses with the gradient method applied to the continuum. They have been derived with Junge's algorithm and are shown as time-series for the 72 ten-day time-sections ("events") fitted into 1964-65. Dots along the time axes identify sections which contain one or more magnetic storm with $C9 \geq 7$. Spectral weights are displayed for all eight frequency bands. Test sites are the observatories Wingst (WNG) in Northern and Fürstenfeldbruck (FUR) in Southern Germany. - Down-weighted sections coincide with storm-time activity, but not always for all frequencies and not always simultaneously at both sites. FUR which is further away from the auroral zone has clearly less down-weighted sections than WNG.

6 MAGNETO-VARIATIONAL SOUNDINGS AT TWO TEST SITES

6.1 Introductory note and comments on the displays

So far results have been presented mainly for single frequencies to illustrate certain aspects of data processing and transfer function estimation. The following displays involve entire sequences of frequencies and have the purpose to illuminate virtues and limitations of the various ways in which gradient soundings can be performed, either alone or in combination with GDS. For completeness we shall include also alternative MVS methods to study 1D structures. Exemplary test sites are again the observatories Wingst (WNG) in Northern and Fürstenfeldbruck (FUR) in Southern Germany.

When response estimates are shown for daily variations (S_r), they have been derived from quiet to moderately disturbed days with $C9 \leq 5$ during the equinoxes 1964-65, i.e. from a total of 226 single days, when no data are missing. Estimates are presented for the first six harmonics from $1\,cpd$ to $6\,cpd$ in correspondence to periods between 24 hours and four hours. Results for the background continuum (S_{cont}) are displayed separately for a test of mutual consistency. They are based on all 72 ten-day time sections fitted into the above two years and comprise eight frequency bands, with mid-frequencies ranging from $0.5\,cpd$ to $7.5\,cpd$ in correspondence to periods between 48 hours and 3.2 hours.

When spatial derivatives are needed for gradient sounding, they refer to differentiated second order polynomials according to eqs (57) and eqs (62/63), yielding for example for the spatial horizontal gradient in eq. (55)

$$G = \frac{\partial B^*_{nu}}{\partial u} + \frac{\partial B^*_{nv}}{\partial v} = a_{10} + b_{01} + 2 \cdot (a_{20} + a_{02})u + 2 \cdot (b_{20} + b_{02})v \tag{73}$$

or alternatively

$$G = a_{10} + b_{01} + (c_{01}v + c_{10}u)/C_{mod}(\omega)\,. \tag{74}$$

In the S_r-analyses polynomials with seven coefficients will be used and thus eq. (74) applies, while in S_{cont}-analyses G will be derived from complete second order polynomials with nine coefficients which leads to eq. (73). These choices have been found to yield the most consistent results. It will be shown in Part II how to avoid a bias on the final estimates due to the involvement of a preset preliminary model response C_{mod} in eq. (74).

Estimates of complex-valued C-responses are shown with error bars in complex planes. Real parts $z*(m) = Re[C(\omega)]$ are plotted downwards on a linear scale, imaginary parts horizontally on a logarithmic scale after a conversion into apparent resistivities $\rho*(\omega) = 2\mu_0\omega\{Im[C(\omega)]\}^2$. Visually $z*$ represents the depth of a substitute *perfect* conductor at the respective angular frequency ω, and $\rho*$ is the resistivity of a substitute finite uniform conductor below a non-conducting top layer of thickness $h = Re\{C\} + Im\{C\}$. For a conversion into the conventional MTS apparent resistivity $\rho_a(\omega) = \omega\mu_0 \mid C \mid^2$, divide $\rho*$ by $2\cos^2\phi$, where $\phi = arg\{Z\} = \pi/2 + arg\{C\}$ denotes the phase of the (scalar) impedance (cf. eq. 4). Since long-periodic variations have phases mostly above $\pi/4$, this implies $-Im\{C\} < Re\{C\}$ and thus h will be positive. In those rare cases that the phase is below $\pi/4$, apparent resistivities $\rho*$ will be calculated differently (cf. Schmucker, 1987, Section 4.1).

By this conversion of C-responses into $\rho * - z*$ plots for a sequence of frequencies we obtain smoothed images of resistivity versus depth as they may evolve eventually from a joint interpretation of all displayed responses. Furthermore, $\rho * - z*$ plots provide an effective control whether a given set of C- responses is compatible with a 1D model (cf Weidelt, 1972, eq. 2.31). If this is so, $z*$ as a measure for the depth of penetration cannot decrease with increasing period. Thus from $z*$ for the shortest and longest periods we can infer the depth range, for which reliable information on resistivity can be expected. The corresponding constraint for $\rho*$ is less visibly contained in the condition $0 \leq d\log \mid C \mid / d\log \mid T \mid \leq 1$.

As guidelines we add in all $\rho * - z*$ plots global C-responses obtained with the potential method (cf. eq.41). These are not empirical estimates, however, but theoretical responses for a 4-layer spherical Earth model, which can account for the empirical potential ratio of internal to external parts for the six harmonics of S_r (cf. Schmucker, 1999b, Table 8 and Fig. 1). Their $\rho * - z*$ values are shown therefore without error bars, and they refer to spherical responses $C_n(\omega)$ as introduced in eq. (21). In the case of daily variations they are for source fields, whose configuration on spheres is given by spherical harmonics of degree $n = p+1$, which contain the dominant "principal" spherical harmonic in the expansion of the p-th time harmonic. For the continuum we use uniformly $n = 1$ for all frequencies, knowing that any realistic source field representation would require a wide spectrum of spherical harmonics to account for its complicated spatial structure in high latitudes. Recalling that all MVS transfer functions have been derived under the assumption of quasi-uniformity of the source, the possibility of source-effects will receive further attention in Part II.

Results of geomagnetic depth sounding are shown in the form of *induction vectors* $\underline{c}$ for GDS transfer functions Z_H and Z_D. With $\underline{\hat{x}}$ and $\underline{\hat{y}}$ as unit vectors towards geographic north and east, respectively, we shall use the definitions

$$\underline{c}_{Re} = -Re(z_H)\underline{\hat{x}} - Re(z_D)\underline{\hat{y}}, \; \underline{c}_{Im} = +Im(z_H)\underline{\hat{x}} + Im(z_D)\underline{\hat{y}} \tag{75}$$

and thereby follow *Parkinson's* convention for the real vector $\underline{c}_{Re}$ and *Wiese's* convention for the imaginary vector $\underline{c}_{Im}$. The particular choice of signs corresponds to their original definition, and it is used here for the same reason (cf. Schmucker, 1970a, eq.3.19): For long-periodic variations induction anomalies tend to have GDS transfer functions with positive phases. Hence, for elongated anomalies our two vectors point in opposite directions normal to the strike, with $\underline{c}_{Re}$ in the direction of *decreasing* depth of penetration toward a better conducting substructure and with $\underline{c}_{Im}$ in the direction of *increasing* depth of penetration for a less conducting substructure (cf. eqs 32 and 36). With the same choice of signs both vectors would coincide in direction which makes their visual distinction difficult.

6.2 $\rho^* - z^*$ plots of C-responses obtained with univariate gradient sounding

We start in Figs 12 and 13 with univariate gradient sounding towards scalar C-responses according to eq. (55). Plots on the left of each figure display the results for the six harmonics of daily variations, covering in $z*$ the depth range from $300\,km$ at 4 hours to $650\,km$ at 24 hours. Plots on the right show the $\rho * - z*$ values for the eight continuum periods which extend the $z*$ depth range by about $50\,km$ at either end, from $250\,km$ at 3.2 hours to more than $700\,km$ at 48 hours. Beginning with test site FUR, we notice in Fig. 12 a nearly perfect agreement between local and global results up to the fourth harmonic of daily variations, with errors in the order of just $10\,km$ or two percent. When for the last two harmonics greater deviations occur, they remain nevertheless within the increased error bounds.

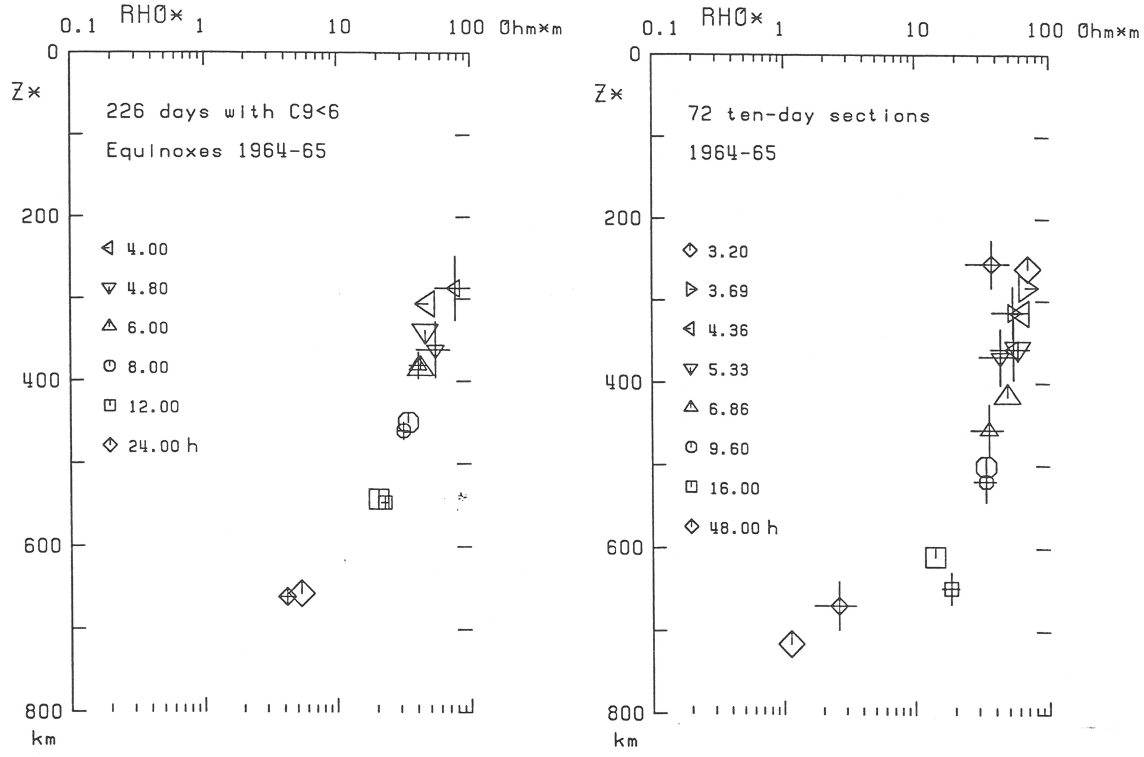

Figure 12: $\rho* - z*$ presentations of scalar C-responses in complex planes, derived with univariate gradient sounding for the observatory Fürstenfeldbruck (FUR) in Southern Germany. Left: Results for the six harmonics of daily variations. Right: Results for the eight frequency bands of the spectral continuum. Large symbols without error bars are theoretical responses for a global model (cf. legend to Fig. 9). - Local and global C-responses agree within error limits for all six harmonics of daily variations, but slightly deviating results are obtained for the first two frequency bands of the continuum.

This coincidence of local and global soundings represents a remarkable achievement in itself and demonstrates the virtues of gradient soundings under favourable 1D conditions, namely that B_z-data from a *single* site can reproduce estimates on a global scale involving B_z-data from a *multitude* of sites. It means also that the substructure beneath FUR cannot be too different from what we may regard as a continental norm. The thereby indicated absence of induction anomalies will be verified with GDS results below. As to be expected under such circumstances gradient sounding in combination with GDS does not lead to any improvement and thus estimates from multivariate regressions are not shown. The smooth decrease of $\rho*$ from values close to $100\,\Omega m$ at $300\,km$ to $4\,\Omega m$ at $650\,km$ corresponds to the well known drop of mantle resistivities below $1\,\Omega m$ at about this depth, occurring either continuously or in one or more discontinuous steps.

Turning to the display on the right of Fig. 12 we note not only larger error bounds, but for the first two continuum periods also substantial deviations from global responses. From the third period onward local estimates are compatible again with global results. Recalling that S_q-variations have been removed prior to the continuum analysis, the two sets of C-responses may be regarded as independent estimates and it is noteworthy that they are both compatible with one and the same global model.

Figure 13 repeats the displays for the second test site WNG. We shall see that this site comes toward short periods under the growing influence of a prominent induction anomaly in Northern Germany. As a consequence the agreement with global results is limited now to the first two harmonics of daily variations. Beyond them a widening gap opens and in particular $z*$ ceases to decrease with decreasing periods. Similar discrepancies exist for the corresponding continuum periods. For its second period the local estimate is even far away from the global value. These inconsistencies can be removed at least partially by the use of multivariate regressions as shown in Fig. 14 for trivariate analyses. In the case of daily variations they involve the three estimates for a tensor C-response and the Berdichevsky average C_1 is shown, while in the case of the continuum a scalar C-response is displayed which has been derived together with the two GDS transfer functions. The reason for these differing formulations of trivariate regressions will become transparent in Section 6.4. The not shown estimates for complete multivariate analyses involving all five transfer functions according the eq. (35) can remove the remaining deviations for the last two harmonics of S_r, but on the expense of creating new disagreements among the first four harmonics as seen in Table 3, while a 5-variate continuum analysis leads to widely scattered and unreliable results which illuminates the limitation of tensor gradient sounding in combination with GDS.

6.3 $\rho^* - z^*$ plots of C-responses obtained with related methods

The first method to be considered will be the closely related univariate Z:Y method according to eq. (43). Its input variable is again the horizontal spatial gradient, but now derived as G_{SHA} from series of spherical surface harmonics for the potential. Hence, the method has to be carried out in conjunction with a spherical harmonic analysis of the global variation field. But because no separation of external and internal parts is needed, the analysis can be restricted to the horizontal components. Still in view of the sparse network of geomagnetic observatories the pertinent variation field should be of sufficient spatial smoothness to permit a truncation of the series of spherical harmonics after a few terms, a condition which is met in this context only by daily variations during quiet times, representing S_q. The following Z:Y response estimates are based on the analysis of 124 $Q*$ days 1964-65 and G_{SHA} is derived from twelve spherical harmonics for each time harmonic exactly as outlined elsewhere (Schmucker, 1999a, Section 4). The requirement of spatial simplicity becomes even more stringent when only one single spherical harmonic is used as in the Z:H and Z:D methods. For the p-th time harmonic of daily variations our choice will be the most prominent local time spherical harmonic during equinoxes, which is of degree $n = p+1$ and order $m = p$ (cf. Schmucker, 1999a, Fig. 5). Furthermore, because the north-component (H) of S_q-variations is quite small in comparison to its east-component (D) in mid-latitudes near to the centre of the overhead S_q-current loop, we shall use the Z:D method according to eq. (47).

Figure 15 shows that both alternative methods yield for the test site FUR C-responses which in their $\rho* - z*$ presentation reproduce quite correctly the overall mantle structure. But various shortcomings become evident by comparing them with the results in Fig. 12 obtained for the same site with gradient sounding. Except for the first Z:Y estimate all $z*$ depths are smaller than expected, while up the third harmonic $\rho*$ values and thereby the (negative) imaginary parts appear as too large, with no trustworthy Z:D results obtainable for the sixth harmonic. In other words, the problem lies with the correct determination of phases. But it is interesting to note that beyond $1\,cpd$ both methods yield very similar estimates, deviating from the glob al responses more or less in the same way. Thus there seems to exist a common deficiency in both methods to represent adequately the global structure of S_q-variations which cannot be overcome even with the Z:Y method by in-

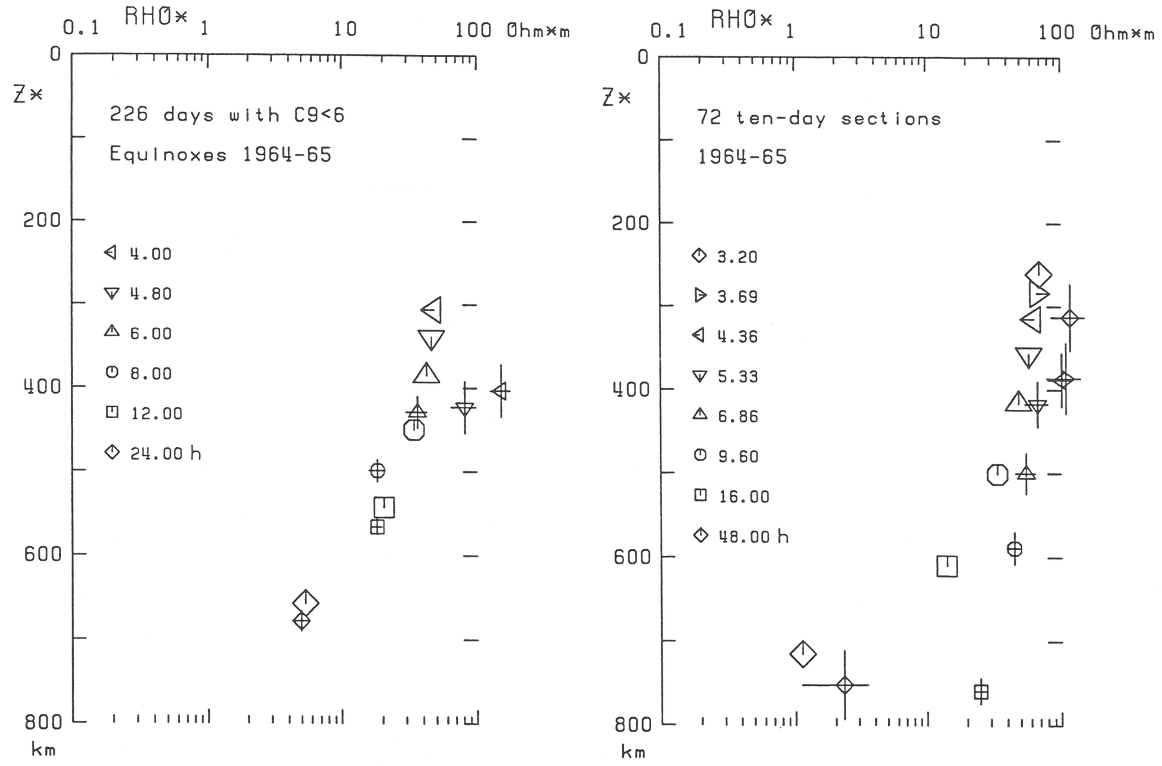

Figure 13: Same as in Fig. 12, but for the observatory Wingst (WNG) in Northern Germany, which with increasing frequency comes more and more under the influence of a local induction anomaly. As a consequence local and global scalar C-responses coincide only for the first two periods in both analyses. Increasing differences appear from the third periods onward, when z* ceases to decrease further with decreasing periods as to be expected for a 1D structure.

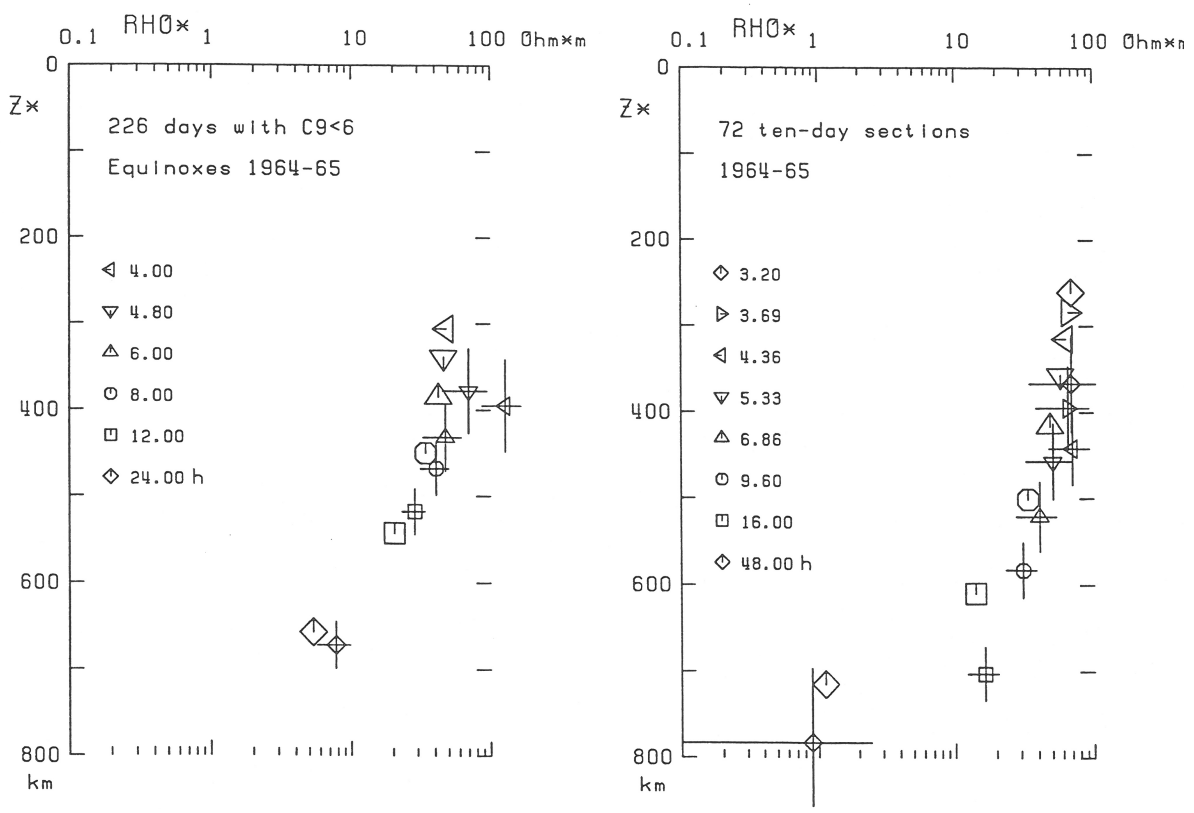

Figure 14: $\rho* - z*$ presentations of C-responses in complex planes, derived with trivariate regressions for the observatory Wingst (WNG) in Northern Germany. Left: Estimates obtained for tensor C-responses without GDS transfer functions; shown are the Berdichevsky averages for the six harmonics of daily variations. Right: Estimates of scalar C-responses which are shown, together with GDS transfer functions for the eight frequency bands of the continuum analysis. Large symbols without error bars are theoretical responses for a global model (cf. legend to Fig. 9). - Multivariate regressions improve the agreement between local and global results in comparison to univariate determinations in Fig. 13. In the ease of daily variations local and global estimates agree now within error limits except for the sixth harmonic of daily variations. For the first two frequency bands of the spectral continuum local estimates have been brought at least closer to their global values, and also imaginary parts as contained in the $\rho*$-values show now a better agreement with their global predictions for the last four frequency bands .

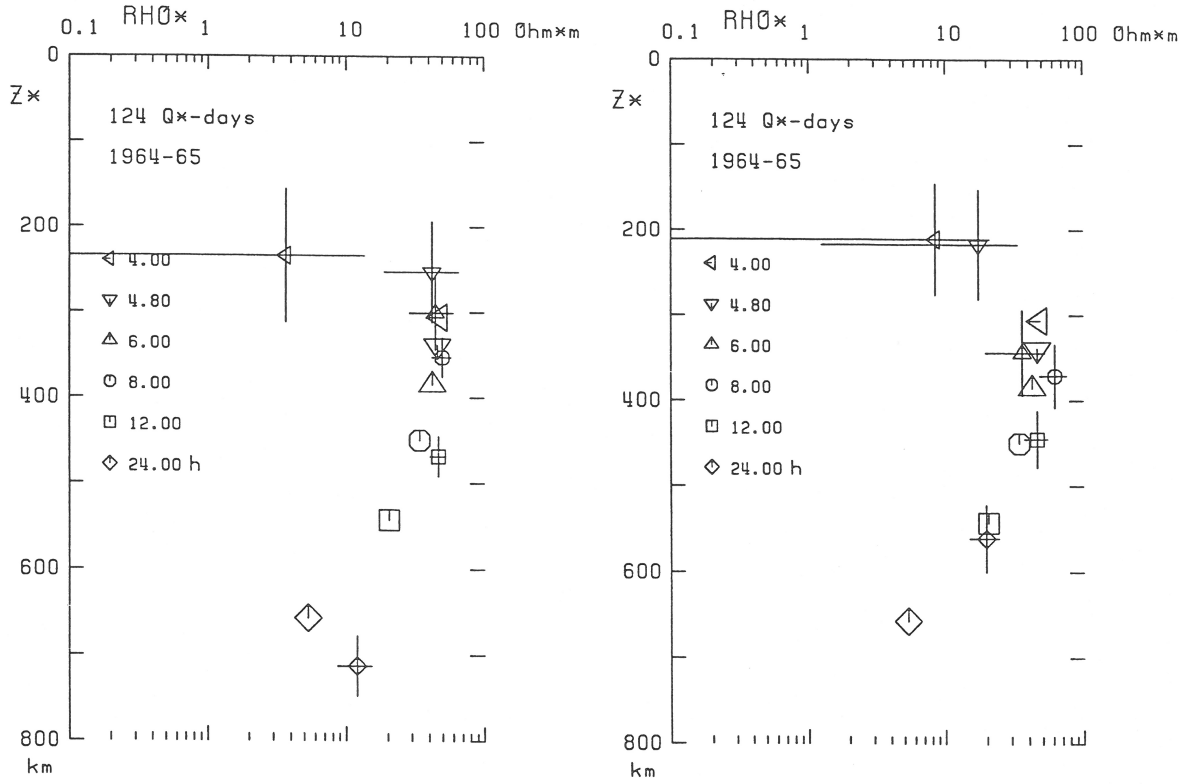

Figure 15: $\rho* - z*$ presentations of scalar C-responses in complex planes derived with alternative methods. Test site is the observatory Fürstenfeldbruck (FUR) in Southern Germany. The analyses are restricted to daily variations on magnetically quiet days. Left: Estimates obtained with the univariate *Z:Y* methods for the six harmonics of daily variations on 124 Q*-days 1964-65. Right: The same for the *Z:D* method. Large symbols without error bars are theoretical responses for a global model (cf. legend to Fig. 9). - Both methods reproduce the overall results of gradient sounding in Fig. 12, even though with greater errors. Furthermore, real parts $z*$ are systematically smaller than those of global responses except for the first *Z:Y* estimate, while imaginary parts as contained in $\rho*$ are in reasonable agreement with their expected values from the global model.

volving series of spherical harmonics. Furthermore, coherencies are substantially lower than those for the gradient method, possibly in conjunction with the presence of noise in the input variables Y and D, a notion which led Olsen (1998) to apply bias correction to his Z:Y response estimates. So far attempts to improve results have not been successful, neither by using the Z:Y method in its multivariate version nor by involving in the Z:D method the H:D ratio of the two horizontal components according to eq. (48).

In conclusion it may be of interest to find out how well the horizontal spatial gradients agree, when they are derived either as G_{POL} from polynomials on a *regional* scale or from spherical harmonics on a *global* scale. Figure 16 shows them both as time-series for the already repeatedly used ten days in 1964, involving hourly means from five observatories on a north-south profile across Europe. The time-series G_{POL} is the same as in Fig. 7, while the time-series G_{SHA} has been generated by a day-by-day synthesis of six time harmonics, each of them the sum of twelve spherical harmonics. During the first three days of exceptional magnetic quietness we note only minor differences, with G_{SHA} perhaps changing slightly more smoothly with latitude than G_{POL}. But discrepancies become striking on the following days of steadily increasing magnetic activity, when from FUR onward oscillations of G_{POL} exceed those of G_{SHA} by factors of two and three. Obviously the adopted series of spherical harmonics is inadequate to approximate the variation field during disturbed times, but otherwise it is not clear from Fig. 16 why during quiet times spatial gradients derived from spherical harmonics rather than polynomials lead to inferior results.

6.4 Induction vectors for GDS transfer functions $\mathbf{z_H}$ and $\mathbf{z_D}$

The eigen-value analysis has shown in Section 5.1 that z_H and z_D are the best resolvable MVS transfer functions in multivariate regressions, and Figs 17 and 18 display them for the two test sites in the form of induction vectors according to eq. (75). They are arranged column-wise, in Fig. 17 for the six harmonics of daily variations and in Fig. 18 for the eight continuum frequencies. The half axes of the error ellipses depict the error bounds of the absolute values of z_H and z_D, respectively. Their mostly circular form indicates that both transfer functions have been determined with comparable accuracy. For a mutual test each illustration shows the results of trivariate and 5-variate analyses, i.e. the GDS transfer functions have been derived in combination with either a scalar or a tensor C-response. We observe an overall agreement within error limits, but we note also that for the continuum the 5-variate results are partially not significant due to very large errors. Nevertheless the restriction to a scalar C-response does not seem to modify the final outcome to any significant extent.

We cannot overlook, however, a striking discrepancy between GDS results from daily variations and the spectral continuum, which is evident in both regressions. Induction vectors derived for S_{cont} are hardly significant at FUR, as to be expected for a 1D substructure, while WNG has quite prominent induction vectors, changing very consistently with frequency: Real vectors point toward a well conducting slab to the southwest of WNG, increasing in length towards higher frequencies, while imaginary vectors of nearly constant length are in opposite direction, i.e. the phase of the GDS anomaly decreases with decreasing period from close to 90 degrees to about 30 degrees, which agrees well with theoretical expectations.

Induction vectors for the S_r-harmonics are much less consistent in their overall appearance and have also larger error ellipses. At WNG real vectors have at least a tendency to point also in south-westerly directions, but scattering imaginary vectors are not opposite to them at all. For FUR we obtain furthermore imaginary vectors well above error limits, which is in clear conflict with the

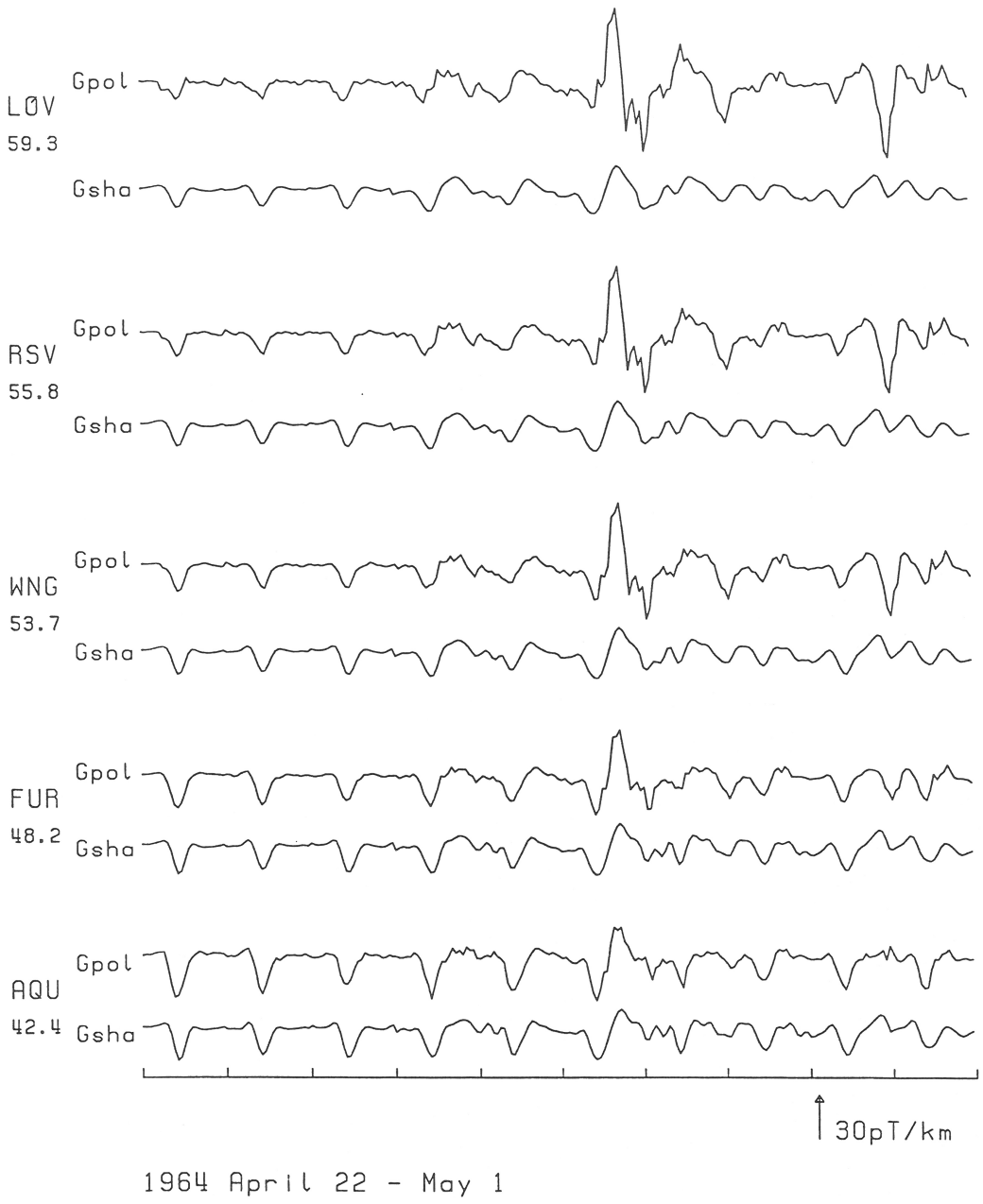

Figure 16: Time series of horizontal spatial gradients G for the same sample records as in Fig. 1, with G derived for the site of the observatory Fürstenfeldbruck (FUR) in Southern Germany: G_{POL} from second degree 2D-polynomials fitted to the horizontal components at 30 observatories in Europe; G_{SHA} from spherical surface harmonics fitted to the horizontal components at 76 observatories world-wide. - Time series agree during the first three days of magnetic quietness except for minor details. But when magnetic activity sets in later on, strong storm-time related variations in G_{POL} exceed those in G_{SHA} at all sites, even though the two time series remain similar otherwise. The difference increases rapidly from south to north, indicating that the *Z:Y* method should be used only during times of magnetic quietness.

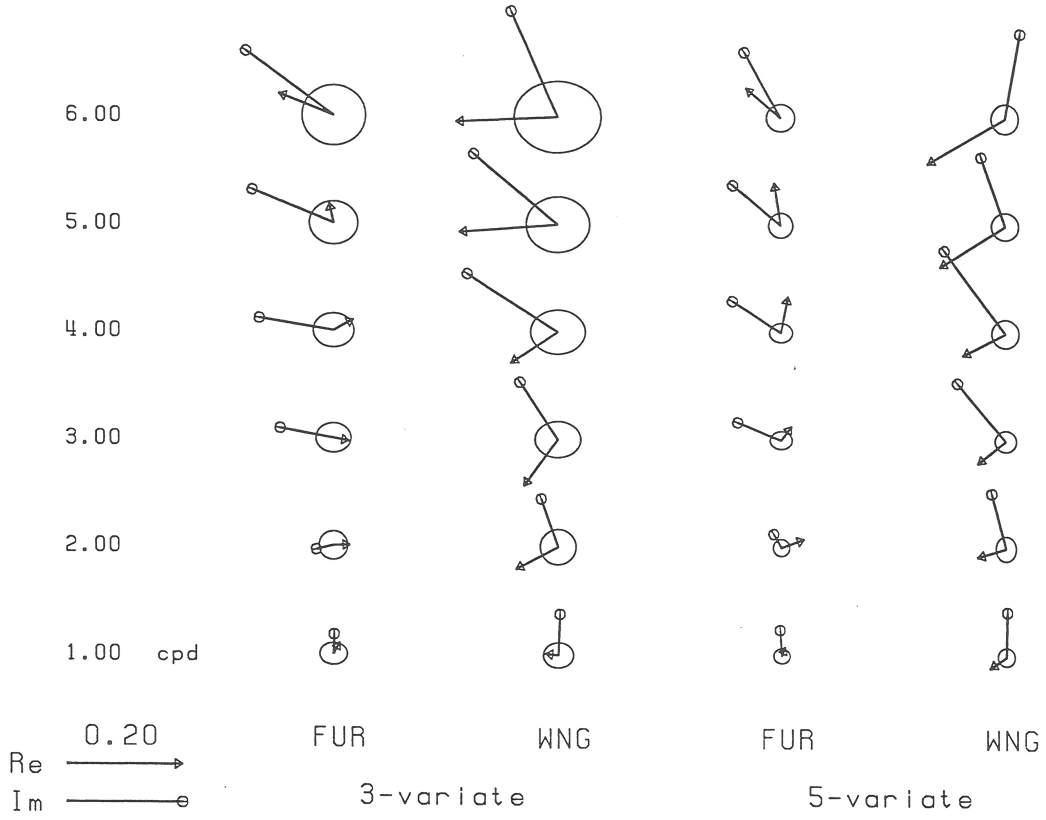

Figure 17: Real and imaginary induction vectors to display GDS transfer functions Z_H and Z_D for the six harmonics of daily variations. Test sites are the observatories Fürstenfeldbruck (FUR) and Wingst (WNG) in Southern and Northern Germany, respectively. Left: Estimates with trivariate regressions, involving a scalar C-response as a third transfer function. Right: Estimates with complete 5-variate regressions according to eq. (33), involving a tensor C-response. Error ellipses visualize the error bounds of the absolute values of Z_H and Z_D, for D-errors left and for J-errors right (cf. Section 5.2). - Overall agreement of the results from trivariate and 5-variate analyses, and more or less consistent changes of lengths and orientations of the vectors with frequency. Significant but presumably unrealistic imaginary induction vectors at FUR from $3\,cpd$ onwards. Real and imaginary induction vectors at WNG are clearly not opposed as to be expected for elongated induction anomalies, indicating problems presumably in connection with correlated input variables (cf. text and Fig. 18).

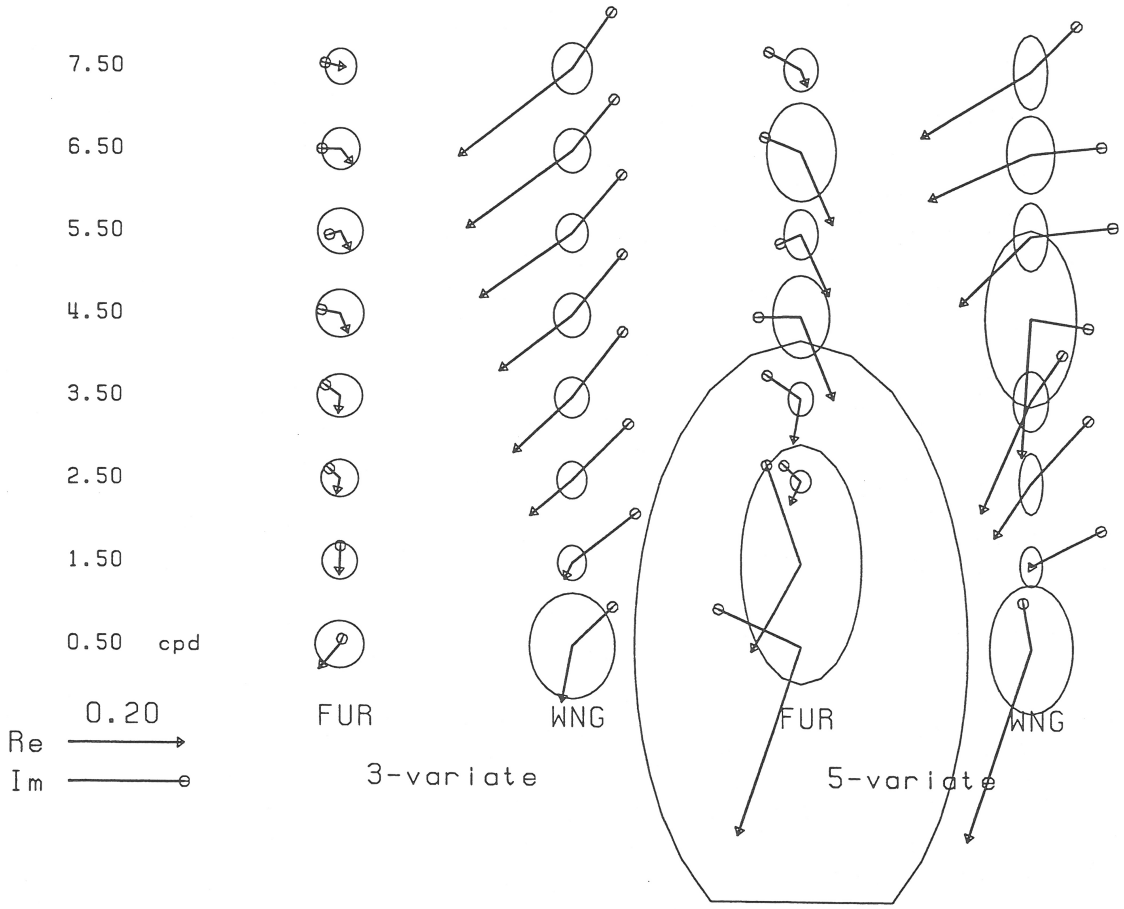

Figure 18: Same as Fig. 17, but for the eight frequency bands of the spectral continuum. - Trustworthy GDS results from trivariate regressions, but excessive error uncertainties in the 5-variate determinations at numerous frequencies. When errors are on a tolerable level for statistically significant results, both regressions lead to GDS transfer functions which are compatible with each other. As expected no significant induction anomaly appears at FUR even at the highest frequency, but from the second frequency band onwards well resolved induction vectors are seen at WNG, changing consistently in lengths, but not in direction with frequency (cf. text). Opposed real and imaginary vectors point toward a well conducting slab to the southwest from WNG striking in north-easterly direction.

conclusion drawn from S_{cont} that no GDS anomaly exists at that site. The cause for the diverging GDS results seems to be that the source field of daily variations has a persistent spatial structure with the implication that its horizontal components are not sufficiently independent from their spatial derivatives. This has the consequence that normal and anomalous parts of B_z cannot be clearly distinguished, a view which is supported by the observation of a significant coherence of about 0.6 for all periods between the input variables G and B_y. Its ultimate cause could be the local time dependence of daily variations. The substorm-related source field of the continuum, in contrast, has a constantly changing and sufficiently complicated time-space structure that coherencies among input variables are practically non-existent. Therefore when considering GDS transfer functions preference will be given henceforth to the more trustworthy continuum results.

6.5 A comprehensive comparison of MVS transfer functions at test site WNG

Table 3 contains for a mutual test the results of uni- and multivariate regressions in various combinations of transfer functions. Estimates are arranged column-wise in six frequency blocs: Each bloc starts with scalar C-responses from univariate gradient sounding followed by the results of two trivariate soundings and a complete 5-variate analysis. Trivariate estimates are either for three tensor C-responses *without* GDS or for a scalar C-responses in combination *with* GDS. Errors are added in parentheses below each estimate. First entries are jack-knife errors (J-errors) and second entries distribution-dependent errors (D-errors), both for an error probability of 32 percent.

We note that D-errors are of about the same size as J-errors for $K = 1$, but twice as large for $K = 3$. This inflation of D-errors is not unexpected and connected to certain assumptions when deriving them (cf. Appendix D). Also not surprising is the increase of errors with the number K of transfer functions, in the case of the 5-variate regression, however, only if estimates are obtained without regularisation, since regularisation tends to lower error bounds. There is also a concurrent rise in coherencies. The increase is not very large for the first harmonic, from 0.962 to 0.970, but quite substantial for the sixth harmonic, from 0.675 to 0.788. It means that the prediction of the output variable B_z improves indeed when more input variables are involved, which puts the here pursued concept of multivariate soundings on a firm statistical basis. Coherencies remain in any case close to unity up to the third harmonics, after which they decline towards values around 0.7. As it has been pointed out in Section 5.1, a corresponding increase of the noise level of the input variables is unlikely to occur, and we expect our estimates to be without bias. This expectation finds support in the almost perfect agreement of jack-knife estimates with conventional estimates by least squares.

Examining now the entries in Table 3 in more detail, we infer from those in the first column that all four analyses lead to comparable C-responses, whether theses are scalar C-responses C_0 or Berdichevsky averages C_1 of a tensor C-response. It is noteworthy that up to $3\,cpd$ they also agree basically with the global model. At higher frequencies, when at the chosen site the influence of a local induction anomaly becomes stronger and stronger, the same tendency can be seen for C_1 as it has been noted already for C_0, namely that their real parts mostly exceed those of the global model responses. Even though the discrepancies are not as large as for C_0, the transition to tensor C-responses and the ultimate inclusion of GDS transfer do not restore consistency to the extent as it could have been expected.

With regard to the so far not considered transfer functions C_2 for anisotropy and C_3 for 3D effects, we recall from Section 5.1 that their determination becomes problematic when done jointly with the two GDS transfer functions, requiring regularisation for a numerically stable inversion of the 5×5 spectral matrix. Hence we have to keep in mind that 5-variate regression results depend to

some extent on the chosen regularisation parameter. Regularisation lowers also the error bounds so that the errors in the 5-variate analysis become smaller than those of the 3-variate regressions carried out without regularisation. We note in Table 3 that the error uncertainties for C_2 and C_3 are quite large and that some of listed estimates are too small to be significant. Still certain consistencies can be found among those exceeding error limits, indicating that they cannot be mere artefacts of a rather complicated analysis. It is difficult to assess their physical implications, however, because conventional 3D modelling is carried out without specifying the TE mode part of the surface impedance.

Hardly any agreement exists with the results of the first listed trivariate analysis, indicating that no trustworthy estimates of C_2 and C_3 can be expected unless GDS transfer functions are taken into account, i.e. the slightly anisotropic C-response at WNG should not be understood as response of a laterally uniform anisotropic substructure. The entries for GDS transfer functions lead to very different conclusions. They are not only well above error limits for all harmonics, but they show also systematic changes among the harmonics. Furthermore, trivariate and 5-variate results are fairly consistent with each other. This confirms the conclusion from Section 6.3 that scalar C-responses are sufficient when combining gradient sounding with GDS.

7 CONCLUSIONS AND OUTLOOK

It will be seen in Part II that the test results reported in Section 6 are representative for mid-latitude MVS studies in the period range of daily variations. Hence, when laterally uniform structures are to be investigated with solely geomagnetic field observations, the gradient method appears to be superior to other methods, based on spherical harmonics. In other words, polynomials or their equivalents fitted to observations on a regional rather than a global scale seem to be the better choice to generate the input variable of the univariate relation far scalar C-responses. The great advantage of the gradient method is that it can be used without concern about the time-space structure of the inducing source field, as in MTS. This has allowed us to apply the gradient method successfully to the line spectrum of daily variations as well as to the associated spectral continuum, thereby involving source fields of very different time-space structures.

But with regard to the source field geometry there exist limitations. A first constraint follows from the requirement of its quasi-uniformity in relation to the depth of penetration at the considered period. As a consequence, gradient sounding with long-periodic variations requires special precautions in the vicinity of ionospheric jets and may not be possible there at all, when the internal part of the variations becomes too small. But the same constraint applies to MTS as well. On the other hand, the source field should be non-uniform enough to produce a measurable vertical component above a 1D substructure. This second purely instrumental constraint does not exist for MTS. There is also the practical aspect that the gradient method requires comparatively elaborate field operations with extremely well calibrated magnetic sensors. We recall from Section 3 and Fig. 7 that spatial derivatives may be in the order of Pico-Tesla per kilometre. Therefore these sensors have to be of sufficient sensitivity as well to resolve the resulting small differences among sites. Furthermore, gradient sounding requires networks of simultaneously recording stations, not necessarily of 30 sites as in the present study, but still preferably in fair excess of the required minimum of three sites to determine spatial differences in the two horizontal directions. Where scalar impedances can be expected, as for instance in sedimentary basins at sufficiently short periods, MTS in shifting single-site operations is clearly the more practical choice.

Laterally non-uniform structures, i.e. the presence of induction anomalies in the magnetic variation field, are no obstacle. In that case the gradient method has to be extended to include GDS transfer functions, and in the complete multivariate formulation the scalar C-response has to be replaced by a tensor C-response. The resulting 5-variate regression has been found to be solvable, at least for the line spectrum of daily variations. But it has been shown also that a reduction to 3-variate regressions is preferable, since it leads to more or less identical but more stably determined GDS results. In addition, since all MVS results are distortion-free with regard to anomalous TM modes, they offer certain advantages to study 3D structures. Due to their relative spatial smoothness they will provide a similarly smoothed image of these structures. On the other hand, MTS results which include anomalous TM modes will be more suitable to reveal near-surface details of the substructure not seen by MVS.

Eventually it may become possible to study the TE and TM modes of MTS impedances separately. Already in the past scalar C-responses have been used repeatedly to remove in a limited way distorting TM modes from them. These C-responses were taken from globally determined potential ratios of external to internal parts or from models. The separation can be accomplished also, at least in principle, with the aid of Faraday's law applied to GDS transfer functions for the vertical component within a network of sites (cf. Becken & Pedersen, 2003, eq. 10). But when in future works tensor C-responses can be derived with greater reliability than in the present study for the same site, where MTS is performed, then the local tensor impedance can be split according to modes. Its TE mode part is identical with the tensor C-response multiplied with $i\omega$, provided the electric field components have been related to the normal horizontal magnetic components (cf. eqs 26 and 29). The decomposition will not be quite complete, however, because the sum of diagonal elements of the tensor C-response remains indeterminable by MVS.

References

Bahr, K., 1985. *Magnetotellurische Messungen des elektrischen Widerstandes der Erdkruste und des oberen Mantels in Gebieten mit lokalen und regionalen Leitfähigkeitsanomalien*, Dissertation.

Bahr, K., 1989. Local Sq response functions from EMSLAB data, (94), 14195–14200.

Becken, M. & Pedersen, L., 2003. Transformation of VLF anomaly maps into apparent resistivity and phase, (68), 4976–505.

Chapman, S. & Bartels, J., 1940. *Geomagnetism*, Claredon Press , Oxford.

Chave, A. & Thomson, D., 1989. Some comments on magnetotelluric response function estimation, (94), 14215–14225.

Dmitriev, V. & Berdichevsky, M., 1979. The fundamental model of magnetotelluric sounding, pp. 1034–1044 (July).

Eckhardt, D., Larner, K., & Madden, T., 1963. Long-periodic magnetic fluctuations and mantle electrical conductivity estimates, (68), 6279–6286.

Egbert, G., 1997. Robust multiple-station magnetotelluric data processing, (130), 475–496.

Egbert, G. & Booker, J., 1986. Robust estimation of geomagnetic transfer functions, *Geophys. J. R. astr. Soc.*, (87), 173–194.

Jenkins, G. & Watts, D., 1968. *Spectral analysis and its application*, Holden -Day , San Francisco.

Junge, A., 1992. On the effective number of degrees of freedom in magnetotelluric transfer function estimation, pp. 139–158.

Junge, A., 1994. *Induzierte tellurische Felder -neue Beobachtungen in Norddeutschland und im Bramwald*, Habil.schrift.

Kuckes, A., 1973. Relations between electrical conductivity of a mantle and fluctuating magnetic fields, (32), 119–131.

Kuckes, A., Nekut, A., & Thompson, B., 1985. A geomagnetic scattering theory for evaluation of earth structure, (83), 319–330.

Larsen, J., Mackie, R., Manzella, A., Fiordelisi, A., & Rieven, S., 1996. Robust smooth magnetotelluric transfer functions, (124), 801–819.

Olsen, N., 1998. The electrical conductivity of the mantle beneath Europe derived from C-responses from 3 to 720 hours, (133), 298–308.

Ritter, O., Junge, A., & Dawes, G., 1998. New equipment and processing for magnetotelluric remote reference observations, (132), 535–548.

Schmucker, U., 1970a. Anomalies of geomagnetic variations in the Southwestern United States, **13**.

Schmucker, U., 1970b. An introduction to induction anomalies, (22), 9–33.

Schmucker, U., 1979. Erdmagnetische Variationen und die elektrische Leitfähigkeit in tieferen Schichten der Erde, (Sonderheft 4), 45–102.

Schmucker, U., 1986. Lokale Sq Analysen mit einem verbesserten Z/H Verfahren, pp. 53–61.

Schmucker, U., 1987. Substitute conductors for electromagnetic response estimates, (125), 341–367.

Schmucker, U., 1999a. A spherical harmonic analysis of solar daily variations in the years 1964-65: response estimates and source fields for global induction.- I. Methods, (136), 439–454.

Schmucker, U., 1999b. A spherical harmonic analysis of solar daily variations in the years 1964-65: response estimates and source fields for global induction.- II. Results, (136), 455–476.

Torta, J. M. & DeSantis, A., 1996. On the derivation of the Earth's conductivity structure by means of spherical cap harmonic analysis, (127), 441–451.

Wang, Z. & Dahlen, F., 1995. Spherical-spline parametrization of three-dimensional Earth models, (22), 3099–3102.

Weidelt, P., 1972. The inverse problem of geomagnetic induction, (38), 257–289.

A GRADIENT SOUNDING WITH NON-UNIFORM FIELDS

The extension of the gradient method to horizontal fields $B_x(x,y)$ and $B_y(x,y)$ of any given spatial distribution requires the Fourier transformation of eq. (9) from the (ω,k)-domain into the (ω,r)-domain, with $\underline{k}=(k_x,k_y)$ as wave-number vector and $\underline{r}=(x,y)$ as position vector in horizontal planes. The inverse Fourier transform of the C-response $\hat{C}(\omega,k)$ is

$$N(\omega,r)=\frac{1}{2\pi}\int_0^\infty C(\omega,k)J_0(kr)k\,dk \tag{A1}$$

which Dmitriev & Berdichevsky (1979) denote as spatial filter in response to a lower conducting half-space, assumed to be laterally uniform. Equation (A1) corresponds to their equation (31) for the TE mode. The Bessel function J_0 of the 1^{st} kind and zero order arises from the integration of $\hat{C}(\omega,k)$ in the (k_x,k_y)-plane along circles of radius $k=(k_x^2+k_y^2)^{1/2}$ and by the use of the Sommerfeld integral

$$\int_0^{2\pi} e^{ikr}d\varphi = 2\pi J_0(kr)$$

in polar (k,φ) coordinates, with $\underline{k}=k(\cos\varphi,\sin\varphi)$ and $dk_x dk_y = k\,d\varphi\,dk$.
The convolution theorem converts eq. (9) into convolutions of the spatial filter with the spatial derivatives of the horizontal components,

$$B_z(x,y)=N(\omega,r)*\partial B_x/\partial x+N(\omega,r)*\partial B_y/\partial y \tag{A2}$$

with $\partial B_x/\partial x$ and $\partial B_y/\partial y$ as inverse Fourier transforms of ik_xB_x and ik_yB_y. The symbol $*$ stands for the 2-dimensional convolution

$$N*F=\int_{-\infty}^{+\infty}\int N(u,v)\cdot F(x-u,y-v)du\,dv.$$

For an approximate evaluation of the convolution integrals in eq. (A2), the horizontal field components are developed into 2-dimensional Taylor series for the surroundings of the sounding point (x,y):

$$F(x+u,y+v)=F(x,y)+u\frac{\partial F}{\partial x}+v\frac{\partial F}{\partial y}+\frac{1}{2!}\left(u^2\frac{\partial^2 F}{\partial x^2}+\ldots\right)+\frac{1}{3!}\left(u^3\frac{\partial^3 F}{\partial x^3}+\ldots\right)+\ldots,$$

with $F=B_x$ or B_y, which leads to integrals over the spatial filter in the form

$$I_{nm}=\int_{-\infty}^{+\infty}\int u^n,v^m N(\omega,r)du\,dv=\int_0^\infty\left\{\int_0^{2\pi}\cos^n\psi\sin^m\psi\,d\psi\right\}N(\omega,r)r^{n+m}r\,dr \tag{A3}$$

with$u=r\cos\psi$, $v=r\sin\psi$, and $du\,dv=r\,d\psi dr$. Obviously the integral is zero unless the exponents n and m are both even numbers or both zero. Furthermore, if one of them is zero and the other an even number n, then $I_{n0}=I_{0n}$. From the differentiated Taylor series follow the spatial derivatives of B_x and B_y as

$$\frac{\partial B_x}{\partial u}=\frac{\partial B_x}{\partial x}+u\frac{\partial^2 B_x}{\partial x^2}+v\frac{\partial^2 B_x}{\partial x\partial y}+\frac{u^2}{2}\frac{\partial^3 B_x}{\partial x^3}+uv\frac{\partial^3 B_x}{\partial x^2\partial y}+\frac{v^2}{2}\frac{\partial^3 B_x}{\partial x\partial y^2}+\ldots$$

and

$$\frac{\partial B_y}{\partial v} = \frac{\partial B_y}{\partial y} + u\frac{\partial^2 B_y}{\partial x \partial y} + v\frac{\partial^2 B_y}{\partial y^2} + \frac{u^2}{2}\frac{\partial^3 B_y}{\partial x^2 \partial y} + uv\frac{\partial^3 B_y}{\partial x \partial y^2} + \frac{v^2}{2}\frac{\partial^3 B_y}{\partial y^3} + \ldots$$

Together with eq. (A3) and the notation $\nabla^2 = \partial/\partial x^2 + \partial/\partial y^2$ they convert the convolution integrals of eq. (A2) into the series

$$B_z(x,y) = I_{00}\left\{\frac{\partial B_x}{\partial x} + \frac{\partial B_y}{\partial y}\right\} + I_{20}\frac{1}{2}\left\{\frac{\partial}{\partial x}\nabla^2 B_x + \frac{\partial}{\partial y}\nabla^2 B_y\right\} + \ldots \tag{A4}$$

It expresses B_z in terms of spatial derivatives of B_x and B_y of uneven orders and thereby extends the gradient method to source fields of unrestricted spatial structure.

We consider now solutions which can be useful in the present context. The transformation of eq. (A1) back into the (ω,k)-domain yields the C-response in terms of the spatial filter:

$$\hat{C}(\omega,k) = 2\pi \int_0^\infty N(\omega,r) J_0(kr) r\, dr\,. \tag{A5}$$

Noting that for $k = 0$ and $J_0(0) = 1$ the right-hand-side is identical with the integral I_{nm} of eq. (A3) for $n = m = 0$, the first series coefficient I_{00} in eq. (A4) turns out to be the same zero wave-number response $\hat{C}(\omega,k) = C(\omega)$ as it appears in eq. (1) for gradient sounding with quasi-uniform source fields. This equation has to be understood therefore as the first term of a series. Furthermore, from eq. (A5) follows with $\partial J_0(kr)/\partial k = -rJ_1(kr)$ that the derivative

$$\partial\hat{C}(\omega,k)/\partial k = -2\pi \int_0^\infty N(\omega,r) J_1(kr) r^2\, dr\,. \tag{A6}$$

vanishes, when for a fixed r the wave-number k and thereby $J_1(kr)$ tend to zero, while the exponential decrease of the spatial filter with increasing distance ensures that $Nr^2 \to 0$ for $r \to \infty$. This asymptotic behaviour of $\partial\hat{C}(\omega,r)/\partial k$ has been the key argument that gradient sounding yields zero wave-number C-responses, which formally apply to uniform fields, even though the induction is by source fields of finite wave numbers.

In order to investigate the influence of the second term on gradient sounding, we replace third derivatives of the horizontal components in eq. (A4) by second derivatives of the vertical component. Using eq. (59) we obtain

$$\frac{\partial}{\partial x}\nabla^2 B_x + \frac{\partial}{\partial y}\nabla^2 B_y = \nabla^2 B_z/\hat{C}(\omega,0)\,,$$

and thereby

$$B_z(x,y) = C(\omega)\left\{\frac{\partial B_x}{\partial x} + \frac{\partial B_y}{\partial y}\right\} + I_{20}\nabla^2 B_z/2C(\omega) + \ldots \tag{A7}$$

with $I_{00} = C(\omega)$.

In mid-latitudes contributions from the so far neglected second term should be rather small. Assuming for a first estimate a uniform half-space of conductivity σ, the integral I_{20} can be solved in closed form. Inserting its C-response $\hat{C}(\omega,k) = (\alpha^2 + k^2)^{-1/2}$ with $\alpha = i\omega\mu_0\sigma$ into the tabulated integral

$$\int_0^\infty \frac{J_0(kr)}{(k^2+\alpha^2)^{-1/2}} k\, dk = \sqrt{\frac{2\alpha}{\pi r}} K_{1/2}(\alpha r) = e^{-\alpha r}/r\,,$$

we obtain as spatial filter

$$N(\omega, r) = e^{-\alpha r}/2\pi r \tag{A8}$$

and thereby from eq. (A3) with $\alpha^{-1} = \hat{C}(\omega, 0) = C(\omega)$

$$I_{20} = \int_0^\infty \frac{1}{2} r^2 e^{-\alpha r} dr = \alpha^{-3} = [C(\omega)]^3 \ .$$

We assume for a first estimate again a source field which can be approximated with a single wave-number k, yielding $\nabla^2 B_z = -k^2 B_z$. The resulting series of eq. (A7), truncated after the second term is

$$B_z = C(\omega) \left\{ \partial B_x/\partial x + \partial B_y/\partial y \right\} \cdot (1+\varepsilon)^{-1} \ , \tag{A9}$$

with the correction $\varepsilon = k^2 [C(\omega)]^2 /2$ for the second term, which is a negative imaginary number. For an appropriate choice of the wave-number k, we recall that the p-th harmonic of daily variations in local time is reasonably well represented by a spherical harmonic of degree $n = p+l$, and thus we use $k^2 = (p+l)(p+2)/R^2$. For an Earth mantle of conductivity $\sigma = 0.02 S/m$ the resulting corrections are $\varepsilon = -0.040i$ for the first harmonic $p = 1$ at $1\,cpd$ and $\varepsilon = -0.062i$ for the sixth harmonic $p = 6$ at $6\,cpd$. Under theses simplifying assumptions the inclusion of the second term rotates $C(\omega)$ in the complex plane by about three degrees anticlockwise for all frequencies.

B THE Z:D METHOD WITH TWO SPHERICAL HARMONICS

The 2 -term magnetic potential in spherical co-ordinates (r, ϑ, λ) to be considered for $r = R$ will be

$$U(r = R, \vartheta, \lambda) = R \left\{ U_n^m P_n^m (\cos\vartheta) + U_{n'}^m P_{n'}^m (\cos\vartheta) \right\} e^{im\lambda}$$

with $n \neq n'$. Omitting references to the cosine of latitude and using the notation $Q_n^m = dP_n^m/d\vartheta$, the tangential components of the magnetic vector $\underline{B} = -grad U$ are

$$B_\vartheta = -R^{-1} \partial U/\partial\vartheta = -a\, e^{im\lambda} \text{ and } B_\lambda = -(R\sin\vartheta)^{-1} \partial U/\partial\lambda = -im/\sin\vartheta\, b\, e^{im\lambda} \tag{B1}$$

with $a = U_n^m Q_n^m + U_{n'}^m Q_{n'}^m$ and $b = U_n^m P_n^m + U_{n'}^m P_{n'}^m$. Solving these equations towards the ratio of potential coefficients leads to

$$U_{n'}^m/U_n^m = (aP_n^m - bQ_n^m)/(bQ_{n'}^m - aP_{n'}^m) \, .$$

This ratio is readily found from $B_\vartheta/B_\lambda = \sin\vartheta/im \cdot a/b$. We assume that the spherical C-responses $C_n(\omega)$ and $C_{n'}(\omega)$ are not very different, replace in eq. (42) for the *Z:Y* method $C_{n'}(\omega)$ by $C_n(\omega)$ and obtain with $\alpha_{nn'} = U_{n'}^m/U_n^m \cdot P_{n'}^m/P_n^m$

$$B_r = -C_n(\omega)/R \cdot U_n^m P_n^m e^{im\lambda} = \left\{ n(n+1) + n'(n'+1)\alpha_{nn'} \right\} \tag{B2}$$

and correspondingly from eq. (B1)

$$i\sin\vartheta/m \cdot B_\lambda = U_n^m P_n^m e^{im\lambda} \left(1 + \alpha_{nn'}\right) \, . \tag{B3}$$

Inserting $U_n^m P_n^m e^{im\lambda}$ from eq. (B3) into eq. (B2) leads to the basic equation of the extended *Z:D* method with a 2-term potential:

$$B_r(\vartheta, \lambda) = n(n+1) C_n(\omega)/R \cdot \sin\vartheta/im \cdot B_\lambda(\vartheta\lambda) f_{nn'} \tag{B4}$$

with

$$f_{nn'} = \frac{1 + \frac{n'(n'+1)}{n(n+1)}\alpha_{nn'}}{1 + \alpha_{nn'}}$$

The added correction factor ensures that the resulting response estimate $C_n(\omega)$ is consistent with the observed ratio of the horizontal components.

C POLYNOMIALS FOR DAILY VARIATIONS IN LOCAL TIME

Since daily variations in longitude λ depend primarily on local time $T = t + \lambda$ rather than on Universal time t, with times in angular measure, their Fourier amplitudes $\tilde{F}_m$ for the m-th harmonic with time-factor $\exp(i\omega T)$ tend to be functions of latitude only. This facilitates their representation by polynomials, but leads to the following complication: Differentiation of Fourier amplitudes F_m with time-factors $\exp(i\omega t)$ towards the eastward co-ordinate v has to take into account the longitude factor, when F_m is replaced by $\tilde{F}_m$. With $f_m = im/R\sin\vartheta$

$$\frac{\partial F_m}{\partial v} = \frac{\partial}{\partial v}\left(\tilde{F}_m e^{im\lambda}\right) = \left\{\frac{\partial \tilde{F}_m}{\partial v} + f_m \tilde{F}_m\right\} e^{im\lambda}\,, \frac{\partial^2 F_m}{\partial v^2} = \left\{\frac{\partial^2 \tilde{F}_m}{\partial v^2} + 2 f_m \frac{\partial \tilde{F}_m}{\partial v} + f_m^2 \tilde{F}_m\right\} e^{im\lambda}\,. \quad \text{(C1)}$$

The potential conditions in eq. (56) has to be changed accordingly, and with coefficients $\tilde{a}_{00}, \tilde{a}_{10}, \ldots$ in the polynomials for $\tilde{B}_\vartheta$ and $\tilde{B}_\lambda$ for the m-th harmonic, the re-formulated identities of eq. (58) are

$$\tilde{a}_{01} + f_m \tilde{a}_{00} = \tilde{b}_{10},\ \tilde{a}_{02} + 1/2\, f_m \tilde{a}_{01} = \tilde{b}_{11},\ \tilde{a}_{11} + 1/2\, f_m \tilde{a}_{10} = \tilde{b}_{20} \quad \text{(C2)}$$

Similarly the local time version of eqs (61) are

$$\begin{aligned} 2(\tilde{a}_{20} + \tilde{a}_{02}) + f_m(2\tilde{a}_{01} + f_m \tilde{a}_{00}) &= \tilde{c}_{10}/C(\omega), \\ 2(\tilde{b}_{20} + \tilde{b}_{02}) + f_m(2\tilde{b}_{01} + f_m \tilde{b}_{00}) &= [\tilde{c}_{10} + f_m \tilde{c}_{00}]/C(\omega). \end{aligned} \quad \text{(C3)}$$

In deriving the last equations linear polynomials were used to derive $\partial F_m/\partial v$ and the absolute terms for $\tilde{F}m$ in order to obtain constant second derivatives, for consistency.

D D-ERRORS FOR MULTIVARIATE REGRESSIONS

Distribution-dependent D-errors ΔC_k establish confidence limits for the absolute values of deviations $\delta C_k = C_k - \Gamma_k$, where C_k is the least squares estimates C_k of the k-th transfer function and Γ_k its expectation value for a large number of realisations. In a first step the residual spectrum $\delta\dot{S}$ of the "true" residuals $\delta\dot{Z}_n = Z_n - \sum_k \Gamma_k X_{nk}$ is set in relation to the residual spectrum δS of the least squares residuals $\delta Z_n = Z_n - \sum_k C_k X_{nk}$, which is readily found from eq. (65). We observe that $\delta\dot{Z}_n = Z_n + \sum_k \delta C_k X_{nk}$ and continue for the moment with $K = 3$ for trivariate linear relations. Then with $\sum_n \delta Z_n X^*_{nk} = 0$ for least squares solutions

$$\begin{aligned} \delta\dot{S} = \sum_n \mid \delta Z_n + \sum_k \delta C_k X_{nk} \mid^2 = \delta S + \sum_k \mid \delta C_k \mid^2 S_{kk} + 2Re\,(\delta C_1 \delta C_2^* S_{12}) + \\ 2Re\,(\delta C_1 \delta C_3^* S_{13}) + 2Re\,(\delta C_2 \delta C_3^* S_{23})\,. \end{aligned} \quad \text{(D1)}$$

Avoiding assumptions about phases of the deviations δC_k, the expressions $Re\left(\delta C_k \delta C_l^* S_{kl}\right)$ are replaced by their upper bounds $\mid \delta C_k \mid \cdot \mid \delta C_l \mid \cdot \mid S_{kl} \mid$. This establishes an upper bound also for the difference $\Delta = \delta \dot{S} - \delta S$ and thereby, as will be seen, for the D-errors as well. An alternative would have been to ignore these expressions altogether, a possibility to be considered in a concluding remark (cf. Jenkins & Watts, 1968, comment to eq. 11.4.44).

With the notations $x = \mid \delta C_1 \mid$, $y = \mid \delta C_2 \mid$, $z = \mid \delta C_3 \mid$ for points $P(x,y,z)$ in Cartesian co-ordinates, and observing that

$$S_{kk} S_{ll} - \mid S_{kl} \mid^2 = S_{kk} S_{ll} (1 - \mathrm{coh}_{kl}^2) \geq 0,$$

eq. (D1) is the equation of an ellipsoid:

$$F(x,y,z) = S_{11}x^2 + S_{22}y^2 + S_{33}z^2 + 2 \mid S_{12} \mid xy + 2 \mid S_{13} \mid xz + 2 \mid S_{23} \mid yz - \Delta = 0.$$

Its centre is at the origin of coordinates, and its principal axes (x', y', z') follow from the directions of the eigen-vectors of a spectral matrix, in which the cross-spectra have been replaced by their absolute values (cf. Section 5.1). With S_{kk} as the k-th eigen-value, the transformation to principal axes yields $F(x', y', z') = S'_{11} x'^2 + S'_{22} y'^2 + S'_{33} z'^2 - \Delta' = 0$ as a rotation-invariant expression. It is assumed that the same ellipsoid applies to all realisations except for a scaling factor, which may vary from realisation to realisation. Upper bounds $\Delta C'_k$ for the projections $x' = \mid \delta C'_1 \mid$, $y' = \mid \delta C'_2 \mid$, $z' = \mid \delta C'_3 \mid$ provide D-errors for the like wise projected estimates $\Delta C'_k$. They can be derived in the same way as described below, but here without the involvement of co-variances which are zero for the projections. But in order to perform the projection to principal axes, the products $.zy = \mid \delta C_1 \mid\mid \delta C_2 \mid$, ... must be known, for example in the form of co-variances as expectation values for these products.

In order to avoid any specific assumptions about them, we can either assume independent deviations with zero co-variances, which most likely leads to underestimation of errors, or we proceed as follows: The ellipsoid is placed into a tightly fitting rectangular box with edges parallel to the (x,y,z) coordinates and of dimensions $(2x_0, 2y_0, 2z_0)$. Then the upper bounds ΔC_1 for x_0, ΔC_2 for y_0 and ΔC_3 for z_0 define the D-errors of the estimates ΔC_k as substitutes for errors $\Delta C'_k$. They clearly overestimate these errors in view of the neglected co-variances in their derivation. For a visualisation we consider an ellipsoid with $x' = \Delta C'_1$, $y' = \Delta C'_2$, $z' = \Delta C'_3$ in the coordinates of principal axes, similarly an enclosing box with $x_0 = \Delta C_1$, $y_0 = \Delta C_2$, $z_0 = \Delta C_3$. Then all realisation points $P(x,y,z)$ with $x' \leq \Delta C'_1, \ldots$ lie within the ellipsoid and thereby also within the box, but not vice versa. The volume ratio of the box to the ellipsoid may reflect the degree of overestimation. If for example all errors $\Delta C'_k = \Delta C_k$ are equal, the volume ratio of the enclosing cube to the enclosed sphere is $6/\pi$, which may serve as a minimum measure for the degree of overestimation of ΔC_k against $\Delta C'_k$. For an elongated ellipsoid in odd orientation the overestimation will be much greater.

After this digression we return to the problem to determine the dimensions of the box. With $P_0(x_0, y_0, z_0)$ as the point of contact between a tangential plane and an ellipsoid, the coefficients in the equation of this plane, $f(x,y,z) = ax + by + cz - d = 0$, follow from

$$f(x,y,z) = \partial F/\partial x \cdot (x - x_0) + \partial F/\partial y \cdot (y - y_0) + \partial F/\partial z \cdot (z - z_0) = 0,$$

with derivatives to be taken at the point of contact. In simplified notations $A = S_{11}$, $B = S_{22}$, $\ldots$, $F = \mid S_{23} \mid$ for the spectra we obtain

$$a = Ax_0 + Dy_0 + Ez_0, b = Dx_0 + By_0 + Fz_0, c = Ex_0 + Fy_0 + Cz_0, d = \Delta$$

Starting with the point of contact $P_0^{(1)}$ on the sides of the box parallel to the (x,y) plane and thereby with $b=c=0$ and $ax=\Delta$, the x coordinate of this point is found to be $x_0^{(1)}=\Delta/a$. The remaining coordinates of point $P_0^{(1)}$ follow from $bC-cF=0$ and $bF-cB=0$ as

$$y_0^{(1)}=\frac{EF-CD}{BC-F^2}x_0^{(1)} \text{ and } z_0^{(1)}=\frac{DF-BE}{BC-F^2}x_0^{(1)}.$$

Insertion into eq. (D1) expresses then Δ in terms of $x_0=x_0^{(1)}=\mid \delta C_k \mid$:

$$\Delta=\dot{\delta S}-\delta S=Ax_0^2+\frac{x_0^2}{(BC-F^2)^2}\left(B(EF-CD)^2+\ldots\right)=x_0^2\left(A-\frac{BE^2+CD^2-2DEF}{BF-F^2}\right)$$

or in the original notation with spectra

$$\dot{\delta S}=\delta S+x_0^2S_{11}(1-\rho_1) \tag{D2}$$

with

$$\rho_1=\frac{S_{22}\mid S_{13}\mid^2+S_{33}\mid S_{12}\mid^2-2\mid S_{12}\mid\mid S_{13}\mid\mid S_{23}\mid}{S_{11}(S_{22}S_{33}-\mid S_{23}\mid^2)}.$$

The interpretation of the parameter ρ_1 is as follows: We consider for the moment the input variable X_{n1} as output variable of a *bivariate* linear process with X_{n2} and X_{n3} as input variables. Then the parameter ρ_1 represent in the notations of Jenkins & Watts (1968, Section 11.4.2) the squared multiple coherence κ_{123}^2 of the bivariate process except that the second term in the numerator should have been $-2Re(S_{12}S_{13}^*S_{23})$.

Corresponding derivations lead to the y coordinate $y_0=y_0^{(2)}$ for the second point of contact for the sides of the box parallel to the (x,z) plane and to the z coordinate $z_0=z_0^{(3)}$ for the third point on the sides parallel to the (x,y) plane. The resulting relations in analogy to eq. (D2) are $\dot{\delta S}=\delta S+y_0^2S_{22}(1-\rho_2)$ and $\dot{\delta S}=\delta S+z_0^2S_{33}(1-\rho_3)$, with $\rho_2$and ρ_3 in corresponding relations to coherence κ_{213}^2 and κ_{312}^2(see below). In the general case the formula for the squared multiple coherence, which is equation 11.4.11 in the cited reference, leads in similar ways to the parameter ρ_k for any number of input variables and thereby to the D-errors of their transfer functions. In the special case of bivariate relations the squared univariate coherency κ_{12}^2 between X_{n1} as output variable and X_{n2} as input variable, or vice versa, leads to $\rho_1=\rho_1=\mid S_{12}\mid^2/S_{11}S_{22}$. The minimum measure for the overestimation of the resulting D-errors is now the ratio of a square enclosing a circ1e, which is $4/\pi$ and thereby near unity.

In the concluding step of the error analysis the residual spectra δS and the squared absolute deviations $\mid \delta C_1\mid^2=x_0^2$, $\mid \delta C_2\mid^2=y_0^2$, $\mid \delta C_3\mid^2=z_0^2$ are regarded as χ^2-distributed random variables with the same variance and with $v_1=2N-2K$ and $v_2=2K$ degrees of freedom, respectively. The upper bounds for x_0^2, y_0^2, z_0^2 are derived in the usual manner by forming F-distributed variance ratios u_k. In the notations of eq. (D2) they are $u_1=\left[x_0^2S_{11}(1-\rho_1)/v_2\right]/\left[\delta S/v_1\right]$, $u_2=\left[y_0^2S_{22}(1-\rho_2)/v_2\right]/\left[\delta S/v_1\right]$, ... Their common upper limit $g(v_1,v_2;\beta)$ follows the chosen error probability β from $\beta=\int_g^\infty f(u)du$, with $f(u)$ as the pdf of F-distributed random variables, which in turn leads to upper bounds for x_0^2, y_0^2, z_0^2 and thereby to D-errors of estimates C_k.

After converting the spectra in eq. (D2) into the squared coherence between input variables, here with the denotation $r_{kl}^2 = \mid S_{kl} \mid^2 / S_{kk} S_{ll}$, the explicit formulas to derive squared D-errors in *trivariate* linear relations are

$$\Delta C_k^2 = \frac{v_1}{v_2} \frac{\delta S}{S_{kk}(1-\rho_k)} g(v_1, v_2; \beta), \tag{D3}$$

where with $r_{123} = r_{12} r_{13} r_{23}$

$$\rho_1 = \frac{r_{12}^2 + r_{13}^2 - 2r_{123}}{1 - r_{23}^2}, \rho_2 = \frac{r_{12}^2 + r_{23}^2 - 2r_{123}}{1 - r_{13}^2}, \rho_3 = \frac{r_{13}^2 + r_{23}^2 - 2r_{123}}{1 - r_{12}^2}.$$

Eq. (65) can be used to replace δS by $S_{zz}(1 - \mathrm{coh}^2)$.

As to be expected, all three coherences between input variables matter. If one of them is unity, then one of the errors is not determinable. If on the other hand two coherences are zero, for example r_{13} and r_{23}, then with $\rho_1 = \rho_2 = r_{12}^2$ we obtain errors ΔC_1 and ΔC_2as if we had solved a bivariate relation, as it should be, except that the limit g is for three rather than two input variables. With $\rho_3 = 0$ the third error is derived as for univariate relations.

In conclusion we return to an alternative evaluation of eq. (D1) which leads to eq. 11.4.44 in Jenkins & Watts (1968). Omitting the last three terms yields $\rho_k = 0$, as it is readily verified, and eq. (D3) shows that this implies an underestimation of errors due to the neglect of coherencies among the input variables.

E JUNGE'S ALGORITHM TO DETERMINE SPECTRAL WEIGHTS

The iterative process is founded on the spectral amplitudes $\sqrt{\delta \hat{S}_{nm}}$ of the residuals. For convenience and in correspondence to Ritter et al. (1998, Appendix A1) we use simplified notations without reference to frequency ω_m and without the letter δ for residuals. Thus

$$S_n^{(j)} = \mid \delta Z_n^{(j)} \mid = \mid Z_n - \sum_k C_n^{(j)} X \mid \tag{E1}$$

denotes the spectral amplitude of the residual δZ_n in the n-th event of a total of N events. If event spectra are band-averaged Fourier products, then S_n is the square root of the band-averaged squared absolute residuals. The added superscript for the jth iteration is necessary because the estimates C_k of transfer functions are derived with weighted sums of event spectra and thereby change slightly with changing weights during the iterative process. Otherwise eq. (E1) corresponds to equation A2 in the cited reference, henceforth referred to as AJ.

The algorithm uses two kinds of spectral weights, denoted here with w_n as in AJ rather than with Q_n^m as in Section 5.3. Introducing the notation $\widetilde{S}_n = \mid S_n - < S_n > \mid$ with $<>$ as mean of all events, robust processing is carried out in the first two iterations with *Huber weights*

$$w_n^H = \begin{cases} 1 & \text{for } \widetilde{S}_n \le c_H \\ c_H / \widetilde{S}_n & \text{for } \widetilde{S}_n > c_H \end{cases} \tag{E2}$$

In the third and final iteration *Tukey weights*

$$w_T = \begin{cases} [1 - (\widetilde{S}_n / c_T)^2]^2 & \text{for } \widetilde{S}_n \le c_H \\ 0 & for \widetilde{S}_n > c_H \end{cases} \tag{E3}$$

are used to let the final weights approach smoothly zero and to eliminate completely any left-over events with excessive spectral amplitudes. Since these weights refer usually to real-valued Gauss-distributed variables, the subtraction of the mean to define $\widetilde{S}_n$ utilises a certain degree of similarity between the *pdf's* of Rayleigh-distributed and Gauss-distributed random variables after their respective means have been removed, a point which will be taken up again below.

The critical point in the derivation of Huber weights is the variance estimate of weighted spectral amplitudes $\Psi_n = w_n \widetilde{S}_n$. It determines the threshold value c_H beyond which Huber down-weighting begins. The algorithm uses the estimate

$$s^2 = \frac{< \Psi_n^2 >}{(< \delta\Psi_n / \delta\widetilde{S}_n >)^2} \tag{E4}$$

of Huber's asymptotic variance for Ψ_n, where $<>$ denotes again the average over the N events (c.f. Junge, 1994, eq. ... and Egbert & Booker 1986, Appendix A.2) The evaluation of eq. (E4) with eq. (E2) yields the standard deviation estimate

$$s_H = \frac{\sqrt{< \Psi_n^2 >}}{N_H / N} \tag{E5}$$

for Huber-weighted spectral amplitudes $\Psi_n = w_H \widetilde{S}_n$, with N_H as the number of events for which $\widetilde{S}_n \leq c_H$. This is equation A7 in AJ. The corresponding estimate for Tukey-weighted spectral amplitudes $\Psi_n = w_T \widetilde{S}_n$ follows from eqs (E3) and (E4) as

$$s_T = \frac{\sqrt{< \Psi_n^2 >}}{1/N \sum\limits_{(n)} [1 - (\widetilde{S}_n / c_T)^2] \cdot [1 - 5(\widetilde{S}_n / c_T)^2]}, \tag{E6}$$

where the notation (n) implies summation over events with $\widetilde{S}_n \leq c_T$.

In the initial phase of robust processing non-robust estimates $C_k^{(0)}$ yield a first set $S_k^{(0)}$ of spectral amplitudes for the residuals, leading in

$$s_0 = 1.483 med[\mid S_k^{(0)} - med(S_k^{(0)}) \mid] \tag{E7}$$

to a first estimate of their standard deviation, which is equation A3 in AJ. On their basis the iterative process begins with the derivation of a first set of Huber weights w_n^H by inserting $c_H = 1.5 s_0$ and $\widetilde{S}_n = \widetilde{S}_n^{(0)}$ into eq. (E2). The standard deviation $s_H^{(1)}$ for $\Psi_n = w_n^H \widetilde{S}_n^{(0)}$ follows from eq. (E5). Subsequently new spectral amplitudes $\widetilde{S}_n^{(1)}$ result from updated estimates $C_k^{(1)}$, based on Huber-weighted sums of event spectra.

The second iteration repeats the first one. A new set of Huber weights $w_n^{H'}$ is derived with $c_H = 1.5 s_H^{(1)}$ and $\widetilde{S}_n = \widetilde{S}_n^{(1)}$, with standard deviation $s_H^{(2)}$ for $\Psi_n = w_n^{H'} \widetilde{S}_n^{(1)}$. Based on the new Huber weights, again updated estimates $C_k^{(2)}$ yield in $S_n^{(2)}$ the spectral amplitudes for the third and final iteration. Now Tukey weights are obtained by evaluating eq. (E3) with $c_T = 6 s_H^{(2)}$ and $\widetilde{S}_n = \widetilde{S}_n^{(2)}$, and the Tukey-weighted sums of event spectra lead to the final robust estimates $C_k^{(3)}$. There is no need to derive from them newly updated spectral amplitudes $S_n^{(3)}$ or to calculate the standard deviation s_T for $\Psi_n = w_T \widetilde{S}_n^{(2)}$ according to eq. (E6). Their derivation is useful, however, to test whether the squared normalised spectral amplitudes, $(w_T \widetilde{S}_n^{(3)} / s_T)^2$, resemble indeed χ^2-distributed random

variables, checking at the same time, whether eq. (70) yields with $\delta\hat{S}_{nm} = (S_n^{(3)})^2$ realistic numbers for the effective degrees of freedom v_{eff}.

Junge's algorithm in its original version uses spectral amplitudes for transfer functions C_{kn}, which are obtained individually for each event from its spectra. Therefore Ritter et al. (1998) suggest in their Appendix A2 to update in a second iterative process transfer function estimates, now obtained from global spectra as weighted sums of event spectra, while continuously updating not only the weights, but also the event spectra by a combination of observations and predictions. The purpose is to take into account possible changes in statistical distributions. This second part of Junge's algorithm is not used. The estimates have been updated already during the first iterative process, and there is no evidence for severe violations of the assumption that the distributions of residuals are constant in time.

A concluding note concerns the consequences that the spectral amplitudes are Rayleigh-distributed rather than Gauss-distributed. If A and B are Gauss-distributed random variables with zero mean and the same variance σ^2, then with $c_H = 1.5\sigma$, two times 6.7 percent of their realisations are down-weighted with Huber weights smaller than unity. Furthermore, within the range of $\pm 0.674\sigma$ lie 50 percent of their realisations, and with the factor $1.483 = 1/0.674$ in eq. (E7) the 50% bounds are converted into standard deviations.

The Rayleigh-distributed random variable $R = \sqrt{A^2 + B^2}$ has the mean value $R_M = \sqrt{\pi/2}\sigma$ and the variance $\sigma_R^2 = (2 - \pi/2)\sigma^2$, which yields $\sigma_R = 0.655\sigma$ as its standard deviation. The most probable realisation is $R_W = \sigma = 1.526\sigma_R$, where the relevant *pdf* has its maximum and where it is more symmetric than at the mean value. When R is Huber-weighted with $c_H = 1.5\sigma_R = 0.982\sigma$, then with R_W as zero reference practically no realisations are below $(1 - 0.982)\sigma$. But since 14.0 percent exceed $(1 + 0.982)\sigma$, in the end about the same percentage receives Huber-weights below unity as in the case of Gauss-distributed random variables. Furthermore, with $0.674\sigma_R = 0.442\sigma$ and with $R_{med} = \sqrt{2ln2}\sigma = 1.18\sigma$ as the median, 23.7 percent of the realisations are below $(1.18 - 0.442)\sigma$ and 26.9 percent above $(1.18 + 0.442)\sigma$, which places 49.4 percent within the range $R_{med} \pm 0.674\sigma_R$. Even though the non-symmetry of the Rayleigh-distribution is evident, in the overall percentages both distributions agree.

A small inconsistency arises by the subtraction of the mean instead of the most frequent spectral amplitude to define $\widetilde{S}_n$. With $R_M - R_W = 0.253\sigma = 0.387\sigma_R$ the subtraction of the mean minus a correction of $0.387\sigma_R$ removes this deficiency, using an appropriate estimate of the standard deviation. Without this correction and thus with R_M as zero reference, only 11.8 percent are down-weighted instead of the 14.0 percent. There is no need to consider whether in the case of Tukey weights the threshold $c_T = 6\sigma_R$ for Rayleigh-distributed variables is compatible with the threshold $c_T = 6\sigma$ for Gauss-distributed variables. The assignment of zero Tukey-weights happens so rarely that the exact size of the threshold does not matter.

Table 1: **Polynomials for the horizontal components of magnetic variations in Europe:** Least squares fit to the harmonics of daily variations on 124 Q^*-days 1964-65 and to the harmonics of the spectral continuum in 72 ten-day time-sections 1964-65.

f: frequency, in cpd; N: number of observatories;
M: number of polynomial coefficients; ε: residual[1)] of polynomial fit , in nT;
β: horizontal amplitude[1)], in nT; γ: norm of coefficients[2)], in nT;
λ_1/λ_M: condition number of the normal equation matrix for a fit by least squares.

[1)] rms average of all events and sites (and harmonics within the same frequency band)
[2)] rms average of all events (and harmonics within the same frequency band)

f	N	M	ε	β	γ	λ_1/λ_M	N	M	ε	β	γ	λ_1/λ_M
1.0	35	14	0.85	5.82	9.09	1046	30					
	(32)	9	0.92	5.82	8.81	59	(28)	9	0.71	5.76	8.82	57
		7	0.94	6.50	8.78	9		7	0.76	6.40	8.75	9
		5	1.21	5.82	8.36	4		5	1.09	5.76	8.35	4
1.5	35	14	0.28	1.27	2.03	1046	30					
	(32)	9	0.30	1.27	1.93	59	(28)	9	0.24	1.26	1.94	64
		7	0.32	1.58	2.01	9		7	0.27	1.56	2.03	9
		5	0.37	1.27	1.76	4		5	0.31	1.26	1.78	4

N=30	f	ε	β	γ	f	ε	β	γ
M= 7								
	1.0	0.76	6.40	8.75	0.5	0.32	1.76	2.22
	2.0	0.68	5.09	7.13	1.5	0.27	1.56	2.03
	3.0	0.51	3.11	4.38	2.5	0.21	1.05	1.38
	4.0	0.43	1.63	2.16	3.5	0.18	0.79	1.02
	5.0	0.39	1.01	1.14	4.5	0.17	0.66	0.85
	6.0	0.35	0.84	0.91	5.5	0.16	0.61	0.77

Table 2: **Magnetic activity and residuals in gradient sounding:** Analysis of the first harmonic of daily variations on 721 single days 1964-65; the sounding site is the observatory Fürstenfeldbruck (FUR) in Northern Germany

I: class index for the size of residuals;
*C*9 : whole-day magnetic activity index;
1^{st} column: total number of days with class index *I*;
2^{nd} column: their expected number from χ^2;
3^{rd} to last column: number of days with residuals in class *I* on days with activity index C9 in top row.

		C9=	0	1	2	3	4	5	6	7
I=8	11	(0)	1	1	0	3	1	0	3	2
7	8	(0)	0	1	1	0	2	1	2	1
6	9	(0)	0	0	0	0	3	3	2	1
5	12	(2)	1	1	1	0	2	3	4	0
4	30	(5)	9	4	2	2	4	6	3	0
3	48	(16)	11	12	6	5	4	5	4	1
2	156	(49)	33	38	20	31	13	13	7	1
1	224	(156)	79	60	30	24	16	11	3	1
0	223	(493)	88	66	34	21	11	2	1	0
		Sum	222	183	94	86	56	44	29	7

Table 3: **Magneto-variational transfer functions for the six harmonics of daily variations:** Univariate and multivariate analyses of 226 single days during the equinoxes 1964-65; the sounding site is the observatory Wingst (WNG) in Northern Germany; cf. eqs 34 and 55 for notations of C-responses.
K : number of transfer functions[1]; C_k: C-responses[2], in kilometre;
z_H, z_D: GDS transfer functions[2]; coh^2: squared (multiple) coherence[3].

[1] for $K = 5$ regularisation with $\alpha^2 = 0.100$ [2] J- and D-errors in parenthesis (cf. Sect. 5.2)
[3] for $K = 5$ coherence without regularisation added in parenthesis

		C_0 or C_1	C_2	C_3	$z_H \times 100$	$z_D \times 100$	coh^2
1 cpd	K=1	678-165 i	[global model response: 657-171 i]				0.962
		(09, 12)					
	3	672-206 i	10- 20 i	222- 42 i			0.967
		(15,27)	(30,56)	(40,77)			
	3	640-154 i			-03+ 72 i	23+ 03 i	0.969
		(16,31)			(11,22)	(14,27)	
	5	655-146 i	23- 11 i	39+117 i	20+ 78 i	29- 02 i	0.967
		(22, -)	(30, -)	(59, -)	(16, -)	(15, -)	(0.970)
2 cpd	K=1	566-223 i	[global model response: 543-237 i]				0.964
		(08,09)					
	3	528-280 i	-49- 91 i	118-174 i			0.968
		(16,26)	(26,44)	(47,75)			
	3	557-162 i			39+ 85 i	75- 30 i	0.968
		(19,32)			(18,31)	(18,32)	
	5	531-203 i	-08- 85 i	07- 71 i	15+ 97 i	50- 25 i	0.967
		(16, -)	(20, -)	(38, -)	(16, -)	(14, -)	(0.970)
3 cpd	K=1	499-183 i	[global model response: 450-250 i]				0.932
		(10,13)					
	3	468-273 i	15- 66 i	215-160 i			0.946
		(15,31)	(24,50)	(37,79)			
	3	543-165 i			82+101 i	61- 68 i	0.946
		(21,38)			(17,32)	(24,41)	
	5	517-193 i	90- 73 i	87- 68 i	40+102 i	49- 85 i	0.944
		(19, -)	(21, -)	(31, -)	(19, -)	(19, -)	(0.957)

Table 3 continued

		C_0 or C_1	C_2	C_3	$z_H \times 100$	$z_D \times 100$	coh^2
4 cpd	K=1	429-223 i (16,19)	[global model response: 385-241 i]				0.820
	3	432-255 i (22,39)	03-136 i (33,57)	283-207 i (65,114)			0.842
	3	588-144 i (29,49)			55+102 i (22,39)	84-163 i (29,49)	0.869
	5	477-141 i (25, -)	77-100 i (25, -)	66- 36 i (37, -)	39+146 i (26, -)	75-108 i (24, -)	0.842 (0.883)
5 cpd	K=1	423-299 i (26,31)	[global model response: 339-225 i]				0.687
	3	378-277 i (25,49)	-64-186 i (28,60)	161- 80 i (55,117)			0.761
	3	503-137 i (31,62)			14+124 i (27,49)	177-151 i (29,57)	0.777
	5	355-143 i (24, -)	-44-152 i (23, -)	59+ 37 i (28, -)	73+122 i (24, -)	116- 42 i (24, -)	0.703 (0.811)
6 cpd	K=1	403-372 i (26,31)	[global model response: 306-210 i]				0.675
	3	395-342 i (25,53)	-53-139 i (29,63)	223 – 86 i (55,122)			0.753
	3	428-195 i (43,76)			09+186 i (37,63)	183 – 83 i (44, 78)	0.769
	5	301-179 i (24, -)	-20-121 i (24, -)	81+04 i (24, -)	80+150 i (26, -)	138 +27 i (24. -)	0.703 (0.788)